

Nanomaterials for Thermoelectrics

Guest Editors: Hyung-Ho Park, Won-Seon Seo, Jin-Sang Kim, Chan Park, and Jung-Kun Lee





Nanomaterials for Thermoelectrics

Nanomaterials for Thermoelectrics

Guest Editors: Hyung-Ho Park, Won-Seon Seo, Jin-Sang Kim,
Chan Park, and Jung-Kun Lee



Copyright © 2014 Hindawi Publishing Corporation. All rights reserved.

This is a special issue published in “Journal of Nanomaterials.” All articles are open access articles distributed under the Creative Commons Attribution License, which permits unrestricted use, distribution, and reproduction in any medium, provided the original work is properly cited.

Editorial Board

K. E. Aifantis, Greece
Nageh K. Allam, USA
Margarida Amaral, Portugal
Xuedong Bai, China
Lavinia Balan, France
Enrico Bergamaschi, Italy
T. Borca-Tasciuc, USA
C. Jeffrey Brinker, USA
Christian Brosseau, France
Xuebo Cao, China
Shafiul Chowdhury, USA
Kwang-Leong Choy, UK
Cui ChunXiang, China
M. A. Correa-Duarte, Spain
Shadi A. Dayeh, USA
Ali Eftekhari, USA
Claude Estourns, France
Alan Fuchs, USA
Lian Gao, China
Russell E. Gorga, USA
Hongchen Chen Gu, China
Mustafa O. Guler, Turkey
John Zhanhu Guo, USA
Smrati Gupta, Germany
Michael Harris, USA
Zhongkui Hong, China
Michael Z. Hu, USA
David Hui, USA
Y.-K. Jeong, Republic of Korea
Sheng-Rui Jian, Taiwan
Wanqin Jin, China
Rakesh K. Joshi, UK
Zhenhui Kang, China
F. Karimzadeh, Iran
Alireza Khataee, Iran

Do Kyung Kim, Korea
Alan K. T. Lau, Hong Kong
Burtrand Lee, USA
Jun Li, Singapore
Benxia Li, China
Xing-Jie Liang, China
Shijun Liao, China
Gong-Ru Lin, Taiwan
Tianxi Liu, China
J. -Y. Liu, USA
Songwei Lu, USA
Daniel Lu, China
Jue Lu, USA
Ed Ma, USA
Gaurav Mago, USA
Santanu K. Maiti, India
Sanjay R. Mathur, Germany
Vikas Mittal, UAE
Weihai Ni, Germany
Sherine Obare, USA
Atsuto Okamoto, Japan
Abdelwahab Omri, Canada
Edward Andrew Payzant, USA
Kui-Qing Peng, China
Anukorn Phuruangrat, Thailand
Mahendra Rai, India
S. Sinha Ray, South Africa
Ugur Serincan, Turkey
Huaiyu Shao, Japan
Donglu Shi, USA
Vladimir Sivakov, Germany
Marinella Striccoli, Italy
Bohua Sun, South Africa
Saikat Talapatra, USA
Nairong Tao, China

Titipun Thongtem, Thailand
Somchai Thongtem, Thailand
Alexander Tolmachev, Ukraine
Valeri P. Tolstoy, Russia
Tsung-Yen Tsai, Taiwan
Takuya Tsuzuki, Australia
Raquel Verdejo, Spain
Mat U. Wahit, Malaysia
Zhenbo Wang, China
Ruibing Wang, Canada
Shiren Wang, USA
Cheng Wang, China
Yong Wang, USA
Jinquan Wei, China
Ching-Ping Wong, Hong Kong
Xingcai Wu, China
Guodong Xia, Hong Kong
Ping Xiao, UK
Zhi Li Xiao, USA
Yangchuan Xing, USA
Shuangxi Xing, China
N. Xu, China
Doron Yadlovker, Israel
Yingkui Yang, China
Khaled Youssef, USA
Kui Yu, Canada
William W. Yu, USA
Haibo Zeng, China
Tianyou Zhai, Japan
Renyun Zhang, Sweden
Bin Zhang, China
Yanbao Zhao, China
Lianxi Zheng, Singapore
Chunyi Zhi, Hong Kong

Contents

Nanomaterials for Thermoelectrics, Hyung-Ho Park, Won-Seon Seo, Jin-Sang Kim, Chan Park, and Jung-Kun Lee
Volume 2014, Article ID 263080, 1 page

Investigation of the Microstructural and Thermoelectric Properties of the $(\text{GeTe})_{0.95}(\text{Bi}_2\text{Te}_3)_{0.05}$ Composition for Thermoelectric Power Generation Applications, Lior Weintraub, Joseph Davidow, Jonathan Tunbridge, Richard Dixon, Michael John Reece, Huanpo Ning, Iñigo Agote, and Yaniv Gelbstein
Volume 2014, Article ID 284634, 7 pages

An Optimization of Composition Ratio among Triple-Filled Atoms in $\text{In}_{0.3-x-y}\text{Ba}_x\text{Ce}_y\text{Co}_4\text{Sb}_{12}$ System, So-Young Kim, Soon-Mok Choi, Won-Seon Seo, Young Soo Lim, Soonil Lee, Il-Ho Kim, and Hyung Koun Cho
Volume 2013, Article ID 973060, 7 pages

Fabrication and Enhanced Thermoelectric Properties of Alumina Nanoparticle-Dispersed $\text{Bi}_{0.5}\text{Sb}_{1.5}\text{Te}_3$ Matrix Composites, Kyung Tae Kim and Gook Hyun Ha
Volume 2013, Article ID 821657, 6 pages

Formation of Dense Pore Structure by Te Addition in $\text{Bi}_{0.5}\text{Sb}_{1.5}\text{Te}_3$: An Approach to Minimize Lattice Thermal Conductivity, Syed Waqar Hasan, Hyeona Mun, Sang Il Kim, Jung Young Cho, Jong Wook Roh, Sangsun Yang, Soon-Mok Choi, Kyu Hyoung Lee, and Sung Wng Kim
Volume 2013, Article ID 905389, 5 pages

Effect of Mechanical Deformation on Thermoelectric Properties of p-Type $(\text{Bi}_{0.225}\text{Sb}_{0.775})_2\text{Te}_3$ Alloys, Sung-Jin Jung, Seong Keun Kim, Hyung-Ho Park, Dow-Bin Hyun, Seung-Hyub Baek, and Jin-Sang Kim
Volume 2013, Article ID 868540, 6 pages

Thermoelectric Properties of Carbon Nanotube and Nanofiber Based Ethylene-Octene Copolymer Composites for Thermoelectric Devices, P. Slobodian, P. Riha, R. Olejnik, M. Kovar, and P. Svoboda
Volume 2013, Article ID 792875, 7 pages

All-Solution-Processed $\text{InGaO}_3(\text{ZnO})_m$ Thin Films with Layered Structure, Sung Woon Cho, Jun Hyeon Kim, Sangwoo Shin, Hyung Hee Cho, and Hyung Koun Cho
Volume 2013, Article ID 909786, 6 pages

Thermoelectric Properties of Al-Doped Mesoporous ZnO Thin Films, Min-Hee Hong, Chang-Sun Park, Won-Seon Seo, Young Soo Lim, Jung-Kun Lee, and Hyung-Ho Park
Volume 2013, Article ID 131537, 6 pages

Submicron Features in Higher Manganese Silicide, Yatir Sadia, Mor Elegrably, Oren Ben-Nun, Yossi Marciano, and Yaniv Gelbstein
Volume 2013, Article ID 701268, 5 pages

Effect of Surfactant Concentration Variation on the Thermoelectric Properties of Mesoporous ZnO, Min-Hee Hong, Chang-Sun Park, Sangwoo Shin, Hyung Hee Cho, Won-Seon Seo, Young Soo Lim, Jung-Kun Lee, and Hyung-Ho Park
Volume 2013, Article ID 172504, 6 pages



Electronic and Thermal Transport Properties of Complex Structured Cu-Bi-Se Thermoelectric Compound with Low Lattice Thermal Conductivity, Jae-Yeol Hwang, Hyeona Mun, Jung Young Cho, Sang Sun Yang, Kyu Hyoung Lee, and Sung Wng Kim
Volume 2013, Article ID 502150, 7 pages

Solid-State Synthesis and Thermoelectric Properties of $\text{Mg}_{2+x}\text{Si}_{0.7}\text{Sn}_{0.3}\text{Sb}_m$, Sin-Wook You, Il-Ho Kim, Soon-Mok Choi, and Won-Seon Seo
Volume 2013, Article ID 815925, 4 pages

Editorial

Nanomaterials for Thermoelectrics

Hyung-Ho Park,¹ Won-Seon Seo,² Jin-Sang Kim,³ Chan Park,⁴ and Jung-Kun Lee⁵

¹ Department of Material Science and Engineering, Yonsei University, Seoul, Republic of Korea

² Environment-Energy Ceramics, Korea Institute of Ceramic Engineering, Seoul, Republic of Korea

³ Electronic Materials Center, Korea Institute of Science and Technology, Seoul, Republic of Korea

⁴ Department of Material Science and Engineering, Seoul National University, Seoul, Republic of Korea

⁵ Department of Mechanical Engineering and Materials Science, University of Pittsburgh, Pittsburgh, PA, USA

Correspondence should be addressed to Hyung-Ho Park; hhpark@yonsei.ac.kr

Received 15 December 2013; Accepted 15 December 2013; Published 19 January 2014

Copyright © 2014 Hyung-Ho Park et al. This is an open access article distributed under the Creative Commons Attribution License, which permits unrestricted use, distribution, and reproduction in any medium, provided the original work is properly cited.

The production and use of fossil fuels raise environmental concerns. A global movement toward the generation of renewable energy is therefore underway to help meet increased energy needs. Among various green energy technologies, thermoelectric power generation has attracted increasing attention. Thermoelectric generation refers to the direct conversion of waste heat into useful electricity. Because of a nonpolluting and renewable technique, it is a suitable candidate for future energy conversion. High electrical conductivity, low thermal conductivity, and the high Seebeck coefficient are required for thermoelectric materials. However, it is difficult to control these factors individually because thermal conductivity is generally proportional to electrical conductivity. One way to disrupt this relationship is to control the microstructure on a nanoscale. By adopting a new design concept of phonon-glass electron-crystal, nanostructure could be adopted to optimize thermoelectric figure of merit. The goal of this special issue was to exhibit recent developments in the nanomaterials for application in thermoelectrics, so as to plot a picture of (1) the current state of the field and (2) the opportunities for future research related to nanomaterials for thermoelectrics.

A total of 10 articles are presented in the current issue and they are all research papers. They involve nanocomposite formation for thermoelectrics, nanoparticle dispersion in thermoelectric matrix, minimization of lattice thermal conductivity by formation of dense pore structure, mesoporous structured thermoelectrics, and microstructural control of thermoelectric materials. The effects of porosity, doping, mechanical deformation, and microstructure on the thermoelectric properties were discussed.

We are pleased to see the progress in a relation between microstructural control and the properties of thermoelectric materials. We hope that this special issue will contribute to the enhancement of the thermoelectric properties, economically feasible thermoelectric device technologies, and also their wide use.

Acknowledgments

The editors gratefully thank the authors for their contributions to this special issue and the reviewers for their constructive comments and dedication.

*Hyung-Ho Park
Won-Seon Seo
Jin-Sang Kim
Chan Park
Jung-Kun Lee*

Research Article

Investigation of the Microstructural and Thermoelectric Properties of the $(\text{GeTe})_{0.95}(\text{Bi}_2\text{Te}_3)_{0.05}$ Composition for Thermoelectric Power Generation Applications

Lior Weintraub,¹ Joseph Davidow,² Jonathan Tunbridge,³ Richard Dixon,³ Michael John Reece,⁴ Huanpo Ning,⁴ Iñigo Agote,⁵ and Yaniv Gelbstein^{1,2}

¹ Unit of Energy Engineering, Ben-Gurion University of the Negev, Beer-Sheva, Israel

² Department of Materials Engineering, Ben-Gurion University of the Negev, Beer-Sheva, Israel

³ Intrinsic Materials Ltd., Cody Technology Park, Farnborough GU14OLX, UK

⁴ School of Engineering and Materials Science, Queen Mary, University of London, Mile End Road, London E1 4NS, UK

⁵ TECNALIA Research & Innovation, Mikeletegi Pasealekua, 2 20009 San Sebastian, Spain

Correspondence should be addressed to Yaniv Gelbstein; yanivge@bgu.ac.il

Received 12 June 2013; Accepted 5 December 2013; Published 19 January 2014

Academic Editor: Won-Seon Seo

Copyright © 2014 Lior Weintraub et al. This is an open access article distributed under the Creative Commons Attribution License, which permits unrestricted use, distribution, and reproduction in any medium, provided the original work is properly cited.

In the frame of the current research, the *p*-type Bi_2Te_3 doped $(\text{GeTe})_{0.95}(\text{Bi}_2\text{Te}_3)_{0.05}$ alloy composed of hot pressed consolidated submicron structured powder was investigated. The influence of the process parameters (i.e., powder particles size and hot pressing conditions) on both reduction of the lattice thermal conductivity and electronic optimization is described in detail. Very high maximal *ZT* values of up to ~1.6 were obtained and correlated to the microstructural characteristics. Based on the various involved mechanisms, a potential route for further enhancement of the *ZT* values of the investigated composition is proposed.

1. Introduction

Thermoelectrics as a direct energy conversion method between heat and electricity is mainly used for electrical power generation and cooling applications. Germanium telluride based alloys are known as appropriate candidates for *p*-type legs in thermoelectric applications for the 50–500°C temperature range, exhibiting high dimensionless thermoelectric figure of merit ($ZT = (\alpha^2 T)/(\rho \kappa)$, where α is the Seebeck coefficient, ρ is the electrical resistivity, κ is thermal conductivity, and T is absolute temperature) values. GeTe based compounds are characterized by a continuous phase transition from a low temperature rhombohedral to a high temperature cubic rock salt structure that takes place at 427°C in pure GeTe [1].

Germanium telluride based alloys are characterized by a large deviation from stoichiometry toward tellurium rich compositions. The main nonstoichiometric defects are

doubly ionized metal vacancies. As a result of this deviation from stoichiometry, GeTe always exhibits *p*-type conductivity ($p \sim 10^{20} - 10^{21} \text{ cm}^{-3}$) [2]. To reduce the hole concentration, in order to obtain optimal thermoelectric properties, it is necessary to dope GeTe with donor type electroactive impurities. Bi_2Te_3 [3] and PbTe [4] act as donors while dissolved in GeTe. A mechanism of doping GeTe by Bi_2Te_3 has been put forward by Gelbstein et al. [2], according to which the latter is implanted into the GeTe lattice in the form of complexes consisting of a single electroneutral cation vacancy per each Bi_2Te_3 molecule implanted. The introduction of Bi_2Te_3 into the GeTe lattice changes the cation-anion ratio and the vacancy formation is due to the requirement for charge equilibrium. The reduction of the hole concentration in GeTe after introducing Bi_2Te_3 is associated with the filling of the cation vacancies by germanium atoms present in GeTe as a second phase. High thermoelectric performance was recently reported by PbTe alloying of GeTe

for obtaining quasi-binary $(\text{GeTe})_x(\text{PbTe})_{1-x}$ alloys that can be designed for achieving improved electronic properties and lower lattice thermal conductivities, as compared to PbTe and GeTe, separately, via phase separation reactions [5].

The present communication is concerned with the possibility of increasing the thermoelectric figure of merit of p -type Bi_2Te_3 doped $(\text{GeTe})_{0.95}(\text{Bi}_2\text{Te}_3)_{0.05}$ alloy, by optimizing various powder metallurgy parameters (i.e., powder milling and hot pressing conditions) for obtaining both submicrofeatures, resulting in reduced lattice thermal conductivity values, and optimal electronic doping. The combined effects on the resultant ZT values are discussed in detail.

2. Experimental

$(\text{GeTe})_{0.95}(\text{Bi}_2\text{Te}_3)_{0.05}$ was prepared by sealing the source materials (purity of 5N) at appropriate concentrations in a quartz ampoule under a vacuum of 10^{-5} Torr and melting in a rocking furnace at 850°C for 1 hour followed by water quenching. Various milling conditions of the cast ingot to a maximal powder particle size of 50 and $250\text{ }\mu\text{m}$, using agate mortar and pestle, and to smaller sized powder, using energetic ball milling (Fritsch-Pulverisette 7) at 700 RPM following 10 and 20 cycles of 10 minutes each, were applied. The 50 and $250\text{ }\mu\text{m}$ maximal sieved powder were subsequently hot pressed (HPW5 Hot Press FCT Systeme GmbH) under a mechanical pressure of 35 MPa at 450°C and 650°C for 30 minutes, resulting in high density values of ~ 95 and $\sim 97\%$ of the theoretical density, respectively.

Seebeck coefficient (α) and the electrical resistivity (ρ) measurements were carried out in a self-constructed apparatus under an argon atmosphere up to $\sim 450^\circ\text{C}$ at a heating rate of $3^\circ\text{C}/\text{min}$. For the Seebeck coefficient measurements, an auxiliary heater was used to maintain a temperature difference of 10°C between the extremities of the samples. Electrical resistivity was measured by the “four-probe” method using an alternating power source of 1 V/50 Hz.

The thermal conductivity (κ) was determined as a function of temperature from room temperature to 500°C using the flash diffusivity method (LFA 457, Netzsch). The front face of a disc-shaped sample ($\phi = 12\text{ mm}$, thickness $\approx 1\text{--}2\text{ mm}$) is irradiated by a short laser burst, and the resulting rear face temperature is recorded and analyzed. Thermal conductivity values were calculated using the equation $\kappa = \gamma \cdot C_p \cdot \delta$, where γ is the thermal diffusivity, C_p is the specific heat (measured using differential scanning calorimetry, STA 449, Netzsch), and δ is the bulk density of the sample (calculated from the sample's geometry and its mass). The room temperature C_p value for all of the investigated synthesis conditions was found to be equal to $0.23 \pm 0.01\text{ J/grK}$.

The structural characteristics of the various investigated powder conditions were analyzed by high resolution scanning electron microscopy (Jeol-7400F HRSEM), transmission electron microscopy (TEM-FEI TECNAI-G²), and X-ray diffraction (Rigaku DMAX 2100 powder diffractometer). The mean size, d , of the apparent submicron crystalline domains was obtained by applying Scherrer equation,

$d = (K\lambda)/(\omega \cos \theta)$, where λ represents the wavelength of the X-ray radiation, θ is the angle of the considered Bragg reflection, ω is the peaks width on a 2θ scale, and K is a constant close to unity, to the experimental X-Ray diffraction peaks.

3. Results and Discussion

3.1. Powder Structural Characteristics. The microstructure of the $(\text{GeTe})_{0.95}(\text{Bi}_2\text{Te}_3)_{0.05}$ powder hand crushed and sieved to a maximal powder particle size of $50\text{ }\mu\text{m}$ is shown in Figures 1(a)–1(c).

It can be easily seen from these figures that the $50\text{ }\mu\text{m}$ powder exhibits large microscale agglomerates composed of less than $5\text{ }\mu\text{m}$ powder domains, Figures 1(a) and 1(b), which are composed of even finer particles of less than 300 nm particles, as was observed by TEM analysis (Figure 1(c)). A very similar microstructure was also observed for the powder obtained following hand crushing and sieving to a maximal powder particle size of $250\text{ }\mu\text{m}$, indicating that the basic minimal powder particles are much smaller in size than the actually sieved microscale powder agglomerates for this specific composition. Following 700 RPM, 10 and 20 cycles of 10 minutes each, even finer particles than 100 nm were identified, as indicated in Figure 1(d). No finer details could be distinguished by the SEM for the 20-cycle ball milling compared to the 10 cycles' process.

Room temperature XRD analysis following the various applied synthesis conditions, including the high temperature melting (850°C), and hot pressing (450 and 650°C) conditions, obtained at higher temperatures than the rhombohedral to cubic phase transition ($\sim 430^\circ\text{C}$ for pure GeTe), exhibited the typical low temperature rhombohedral structure, being as expected in agreement with the equilibrium phase diagram.

Typical XRD patterns of the 50 and $250\text{ }\mu\text{m}$ hand crushed and sieved powder and ball milled at 700 RPM for 10 and 20 cycles of 10 minutes each are shown in Figure 2. The figure illustrates a typical doublet, characteristic of the low temperature rhombohedral phase of GeTe, which exhibits broadened widths with increasing the applied mechanical forces during the milling process. For the larger agglomerate powder, hand crushed and sieved to 250 and $50\text{ }\mu\text{m}$, relatively narrow peaks were observed, which were analyzed to correspond to average grain size of $40\text{--}60\text{ nm}$, in agreement with the finest grains of less than 300 nm observed by TEM (Figure 1(c)). Increasing the applied mechanical forces during the 700 RPM energetic ball milling procedure resulted in much broadened peaks, corresponding to finer average grain sizes of $20\text{--}25\text{ nm}$. Yet, due to the fact that these large peaks have broadening effect, evidenced in some amorphization of the originally synthesized crystalline GeTe phase, and therefore are expected to degrade the electronic transport properties of the investigated $(\text{GeTe})_{0.95}(\text{Bi}_2\text{Te}_3)_{0.05}$ composition, it was decided to focus in the next stages of the research on investigation of the transport properties of the larger domains powder following 50 and $250\text{ }\mu\text{m}$ sieving, in which a higher level of crystallinity was preserved following the powdering action.

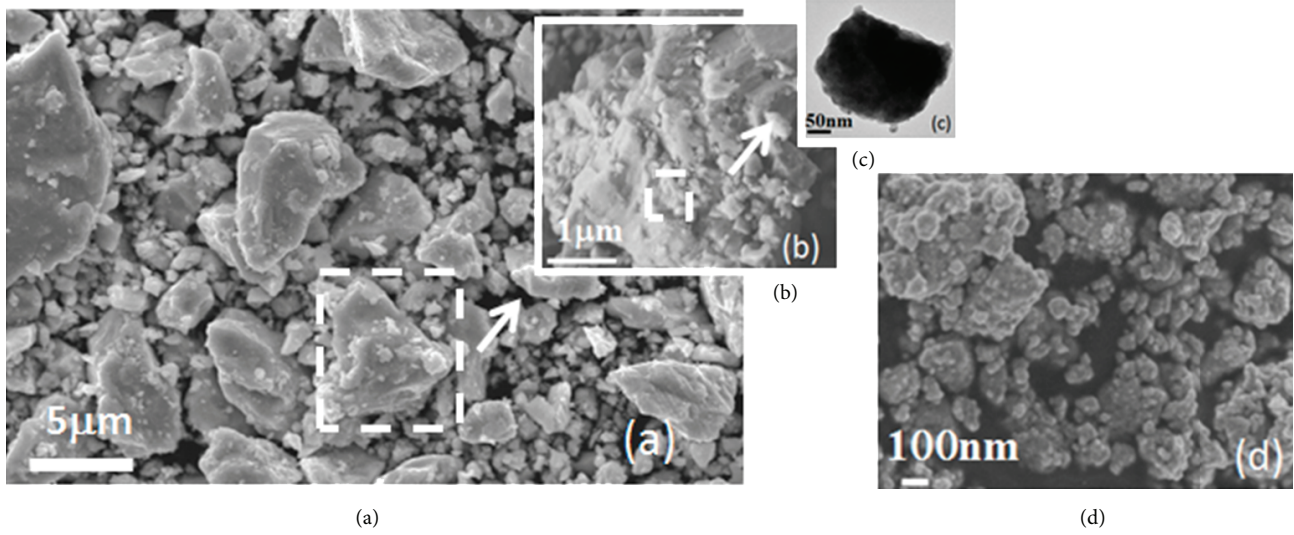


FIGURE 1: SEM (a), higher magnification SEM (b), TEM (c) images of $(\text{GeTe})_{0.95}(\text{Bi}_2\text{Te}_3)_{0.05}$ hand crushed and sieved to maximal sized $50 \mu\text{m}$ powder, and HRSEM image of similar matrix composition following 10-cycles ball milling ball at 700 RPM/10 min (d).

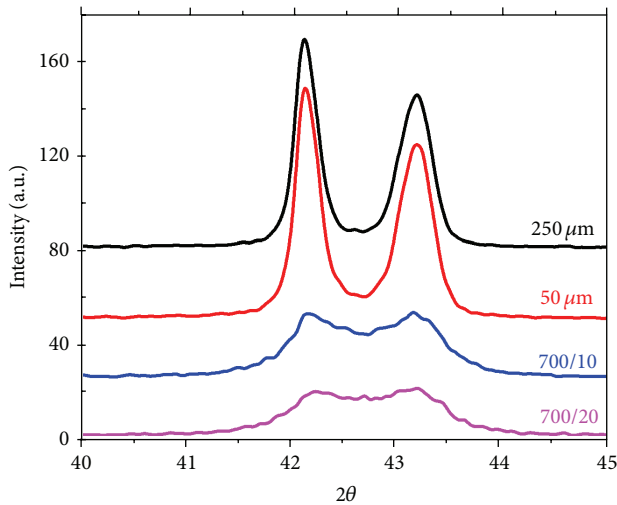


FIGURE 2: Powder XRD of $(\text{GeTe})_{0.95}(\text{Bi}_2\text{Te}_3)_{0.05}$ following hand crushing for maximal powder particles size of 50 and $250 \mu\text{m}$ and following 10 and 20-cycle ball milling of 10 minutes at 700 RPM/10 min.

3.2. Transport Properties following Hot Pressing Consolidation.

As was described above in the experimental section, two hot pressing temperatures of 450 and 650°C were investigated in the current research, yielding density values of ~ 95 and $\sim 97\%$ of the theoretical density, respectively. The 650°C (923 K) temperature, which is about 90% of the melting temperature, T_m , of pure GeTe compound (998 K [6]), was chosen due to the associated high diffusion rates of the involved elements at this temperature and the expected high homogeneity of the investigated composition. The lower hot pressing temperature (450°C) was chosen to be in the vicinity of the phase transition temperature ($\sim 430^\circ\text{C}$ in pure GeTe, [6]) from a low temperature rhombohedral

to a high temperature cubic structures. Both of these hot pressing temperatures, 650 and 450°C , were chosen as slightly lower than the melting temperature and the phase transition temperatures of pure GeTe, respectively, due to the understanding that the investigated $(\text{GeTe})_{0.95}(\text{Bi}_2\text{Te}_3)_{0.05}$ matrix composition, obtained by 5% alloying with the low melting temperature Bi_2Te_3 phase ($\sim 585^\circ\text{C}$ [7]), which is stable from low temperatures up to its melting, is expected to exhibit slightly lower melting temperature and lower phase transition temperatures, respectively, compared to pure GeTe.

The temperature dependencies of Seebeck coefficient, α , electrical resistivity, ρ , and thermal conductivity, κ , of the investigated $(\text{GeTe})_{0.95}(\text{Bi}_2\text{Te}_3)_{0.05}$ composition following hand crushing and sieving to maximal powder agglomerates of 50 and $250 \mu\text{m}$ and hot pressing at 450 and 650°C are shown in Figures 3, 4, and 5, respectively.

Investigation of Figures 3 and 4 reveals that following 650°C hot pressing of both the 50 and $250 \mu\text{m}$ sieved powder agglomerates, nearly identical low temperature α and ρ values, with slightly higher values for the $50 \mu\text{m}$ sample, were observed, indicating similar associated carrier concentrations for both of the samples with slightly lower values for the $50 \mu\text{m}$ sample. This slightly lower overall carrier concentration for the $50 \mu\text{m}$ sample, in which slightly higher mechanical force was applied while crushing the sample to this smaller powder particles size sample, can be attributed to the strain induced compensation effect, in which as was already established for many telluride compounds (e.g. PbTe [8], $\text{Pb}_x\text{Sn}_{1-x}\text{Te}$ [9], $\text{Ge}_x\text{Pb}_{1-x}\text{Te}$ [10], and Bi_2Te_3 [11]), mechanical stresses can result in introduction of additional donor levels in the band gaps, and for the case of inherent p -type compositions, in reduction of the overall carrier concentration.

Although the general high similarity between the α and ρ values obtained following 650°C hot pressing for both of the investigated powder particle sizes, similar low temperature

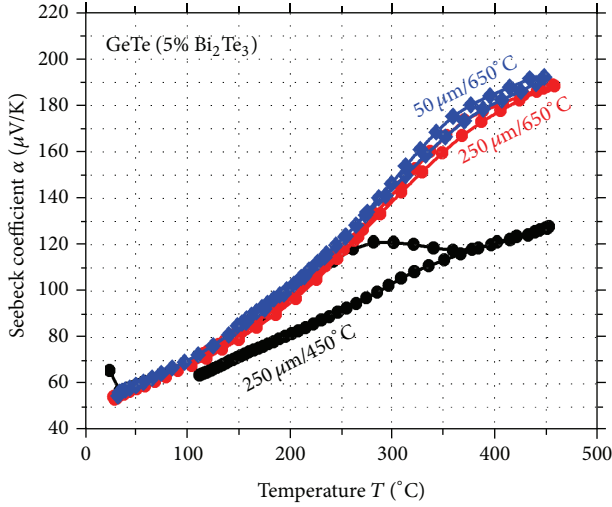


FIGURE 3: Temperature dependence of Seebeck coefficient, α , for $(\text{GeTe})_{0.95}(\text{Bi}_2\text{Te}_3)_{0.05}$ following hand crushing for maximal powder particles size of 50 and 250 μm and hot pressing at 650°C (50 $\mu\text{m}/650^\circ\text{C}$ and 250 $\mu\text{m}/650^\circ\text{C}$, resp.) and for 250 μm hot pressed powder at 450°C (250 $\mu\text{m}/450^\circ\text{C}$).

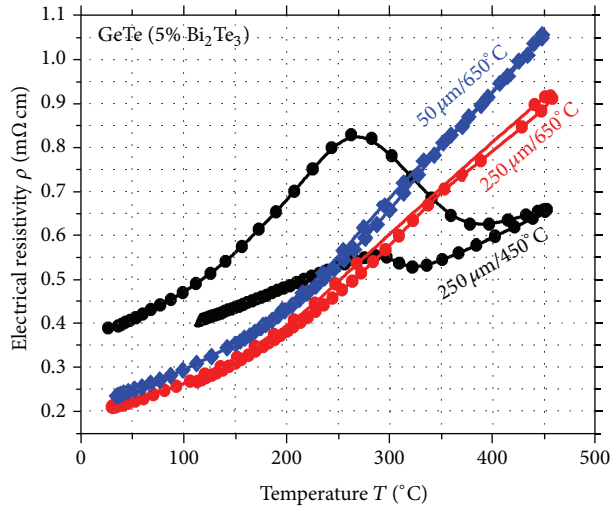


FIGURE 4: Temperature dependence of the electrical resistivity, ρ , for $(\text{GeTe})_{0.95}(\text{Bi}_2\text{Te}_3)_{0.05}$ following hand crushing for maximal powder particles size of 50 and 250 μm and hot pressing at 650°C (50 $\mu\text{m}/650^\circ\text{C}$ and 250 $\mu\text{m}/650^\circ\text{C}$, resp.) and for 250 μm hot pressed powder at 450°C (250 $\mu\text{m}/450^\circ\text{C}$).

Seebeck coefficient values accompanied by much higher low temperature electrical resistivity values were obtained following hot pressing at 450°C of maximal 250 μm sieved powder particles, as shown in Figures 3 and 4. This evidence can be attributed to carrier concentration, p , values similar to those obtained following the 650°C hot pressing, as indicated by the similar α values, but lower carrier mobility, μ , values, as indicated by the higher ρ values ($\rho = (p \cdot e \cdot \mu)^{-1}$) which can result from a lower homogeneity state of this sample, which was hot pressed at much lower temperature than for the case

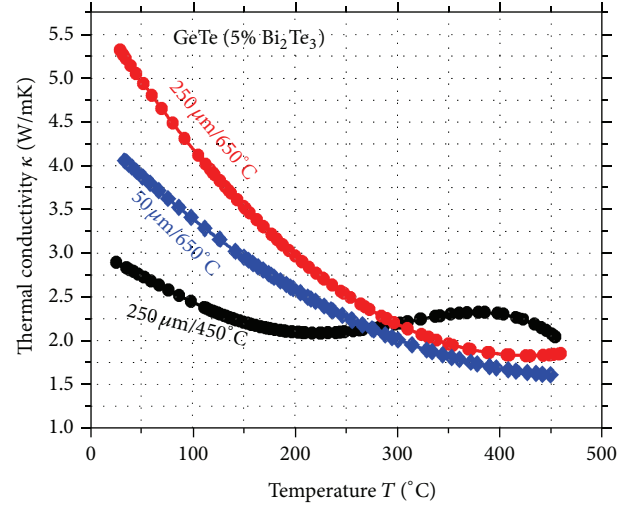


FIGURE 5: Temperature dependence of the thermal conductivity, κ , for $(\text{GeTe})_{0.95}(\text{Bi}_2\text{Te}_3)_{0.05}$ following hand crushing for maximal powder particles size of 50 and 250 μm and hot pressing at 650°C (50 $\mu\text{m}/650^\circ\text{C}$ and 250 $\mu\text{m}/650^\circ\text{C}$, resp.) and for 250 μm hot pressed powder at 450°C (250 $\mu\text{m}/450^\circ\text{C}$).

of the 650°C hot pressing, and can be associated with lower diffusion rates of the involved elements.

Furthermore, both of the α and ρ temperature dependencies of the 450°C hot pressed sample were totally different from those obtained following the 650°C hot pressing procedures. Following the 450°C hot pressing conditions, a thermal hysteresis was observed between the heating and cooling cycles while measuring both α and ρ values, with the most pronounced differences in the 100–400°C temperature range. This abnormal α and ρ temperature dependent trend can result from the second order phase transition, associated with GeTe based compounds, as was previously reported for single crystal grown $\text{Ge}_x\text{Pb}_{1-x}\text{Te}$ and $\text{Ge}_x\text{Sn}_{1-x}\text{Te}$ alloys [12]. In case that as was explained referring to the higher low temperature electrical resistivity values, associated with lower carrier mobility values, compositional inhomogeneity is apparent for this low temperature hot pressing process, compositional variations in the investigated $(\text{GeTe})_x(\text{Bi}_2\text{Te}_3)_{1-x}$ quasi-binary system, are expected to result in a decreased phase transition temperature from the low temperature rhombohedral to the high temperature cubic phases, with decreasing of the x values. As a result, a sequence of multiple $(\text{GeTe})_x(\text{Bi}_2\text{Te}_3)_{1-x}$ compositions is expected to result in extended temperature range in which in the vicinity of each of the individual phase transition temperatures, associated with each of the apparent compositions, a continuous jump in both α and ρ values is expected. Such an effect can explain the abnormal trend observed in both α and ρ values following 450°C hot pressing. For the 650°C ($\sim 0.9 \text{ Tm}$) hot pressing temperature, the much more homogenized state, associated with the much higher diffusion coefficients of each of the involved components, suppresses this effect dramatically.

Regarding the thermal conductivity values (Figure 5) obtained following the 650°C hot pressing conditions, lower

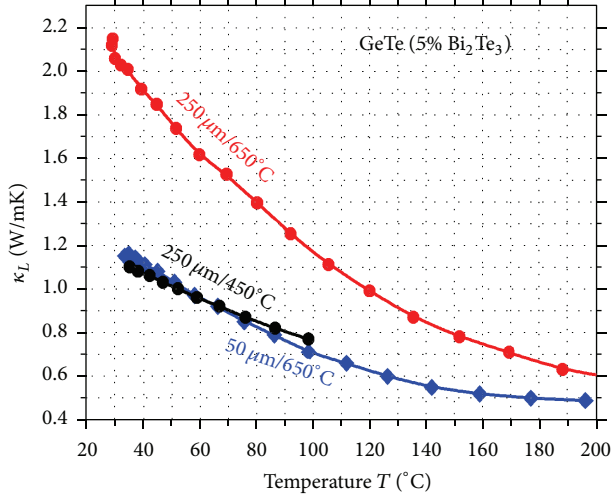


FIGURE 6: Temperature dependence of the lattice thermal conductivity, κ_L , for $(\text{GeTe})_{0.95}(\text{Bi}_2\text{Te}_3)_{0.05}$ following hand crushing for maximal powder particles size of 50 and 250 μm and hot pressing at 650°C (50 $\mu\text{m}/650^\circ\text{C}$ and 250 $\mu\text{m}/650^\circ\text{C}$, resp.) and for 250 μm hot pressed powder at 450°C (250 $\mu\text{m}/450^\circ\text{C}$).

values were obtained following pressing of the maximal 50 μm powder agglomerates compared to the 250 μm condition. Some reduction of the thermal conductivity of the 50 μm powder is expected due to the slightly higher electrical resistivity values (Figure 4) and the consequently lower electronic thermal conductivity, κ_e , values, for this powder condition, as evidenced from the Wiedemann-Franz relation, $\kappa_e = (L/\rho)T$, where L and T are Lorenz number and absolute temperature, respectively. Yet, in order to explain the large (over than 20%) reduction of the thermal conductivity values of the “50 μm ” compared to the “250 μm ” sample, the lattice contribution to the thermal conductivity, κ_L , was also calculated for all of the investigated conditions as presented in Figure 6. For this calculation the reduced Fermi energy (η) was initially calculated at low temperatures ($<200^\circ\text{C}$), for assuring an extrinsic region, using (1) and the measured Seebeck coefficient values (Figure 3) were taken into account:

$$\alpha = \frac{k}{e} \left[\frac{((5/2) + r) F_{(3/2)+r}}{((3/2) + r) F_{(1/2)+r}} - \eta \right], \quad (1)$$

where, e , k , F_r , η , and r are the electrons charge, Boltzmann constant, Fermi integral, the reduced Fermi energy (equals to $[E_F - E_V]/kT$ for p -type materials), and the scattering mechanism parameter (equal to -0.5 for the case of scattering by acoustic phonons as the dominant scattering mechanism, as is the case of GeTe), respectively.

Equation (1) is valid for a quadratic dependence of the carrier energy on the crystal momentum and a power dependence of the mean free time between electron collisions, τ on the kinetic energy ξ ($\tau = \tau_0 \xi^r$, where τ_0 is the constant), as for the case of GeTe based alloys. The heavy hole valence band, present in GeTe, was not taken into account, on account of its minor influence at low temperatures up to very high carrier concentrations of $\sim 7 \times 10^{26} \text{ m}^{-3}$ [13].

At a second stage, the electronic contribution to the thermal conductivity, κ_e , was calculated using the Wiedemann-Franz relation described before, $\kappa_e = (L/\rho)T$, and the measured electrical resistivity values (Figure 4). Lorenz number, given by (2), was calculated using the reduced Fermi energy (η) values obtained from (1) at the initial stage of the calculation:

$$L = \left(\frac{k}{e}\right)^2 \left[\left(\left(r + \left(\frac{7}{2}\right) \right) \left(r + \left(\frac{3}{2}\right) \right) F_{r+(5/2)}(\eta) F_{r+(1/2)}(\eta) - \left(r + \left(\frac{5}{2}\right) \right)^2 F_{r+(3/2)}^2(\eta) \right) \times \left(\left(r + \left(\frac{3}{2}\right) \right)^2 F_{r+(1/2)}^2(\eta) \right)^{-1} \right]. \quad (2)$$

Finally, the lattice contribution to thermal conductivity, κ_L , was calculated by subtraction of κ_e from the measured total thermal conductivity, κ (Figure 5).

It can be clearly seen from Figure 6 that referring to the 650°C hot pressing condition, the “50 μm ” sample exhibits much (reaching $\sim 50\%$, at low temperatures) lower κ_L values compared to the “250 μm ” sample. This result can be explained by the higher population of the less than 300 nm powder domains observed by the electronic microscopy (Figure 1) and XRD (Figure 2) analyses for the “50 μm ” sample, in which higher mechanical stresses were applied during the ingot hand crushing procedures for passing the resultant powder, through the finer sieve size of 50 μm . The increased population of the $<300 \text{ nm}$ powder domains, which are considered as effective phonons scattering centers, is expected to result in lower κ_L values, observed in Figure 6.

Regarding the “250 μm ” powder, much lower low temperature thermal conductivity values were obtained following the 450°C (compared to the 650°C) hot pressing condition, as can be also shown from Figure 5. Again, some reduction was expected due to the increased resistivity values for this sample (Figure 4) and the associated reduced κ_e values as was explained previously. However, further investigation of Figure 6 reveals that the lattice thermal conductivity values are also much lower for this sample, apparently due to the inhomogeneity associated with the lower diffusion rates of the involved matrix components and the possible presence of multiple closely related $(\text{GeTe})_x(\text{Bi}_2\text{Te}_3)_{1-x}$ phases. The latter can also explain the abnormal temperature dependence of the thermal conductivity of this sample (Figure 5) which as was explained previously referring to the electrical resistivity trend (Figure 4) might be influenced by the appearance of a sequence of closely related $(\text{GeTe})_x(\text{Bi}_2\text{Te}_3)_{1-x}$ phases, each associated with different individual phase transition temperature, leading to an extended temperature range of abnormal κ values.

The temperature dependence of the dimensionless figure of merit, ZT , following the various investigated experimental conditions is shown in Figure 7.

From this figure, it can be easily seen that for the homogenized samples obtained following 650°C hot pressing,

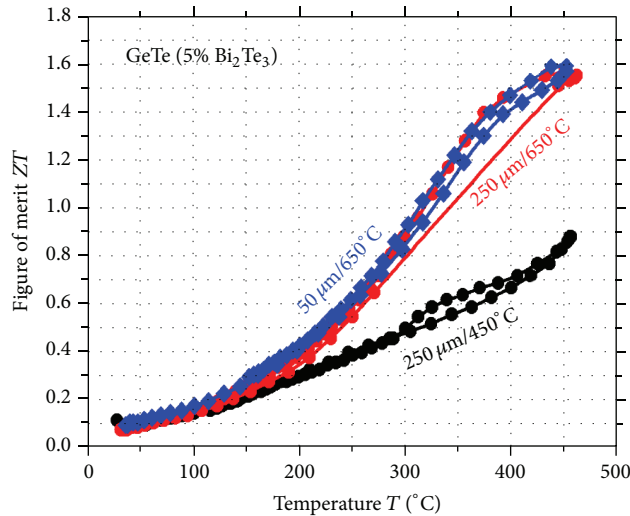


FIGURE 7: Temperature dependence of the dimensionless thermoelectric figure of merit, ZT , for $(\text{GeTe})_{0.95}(\text{Bi}_2\text{Te}_3)_{0.05}$ following hand crushing for maximal powder particles size of 50 and 250 μm and hot pressing at 650°C (50 $\mu\text{m}/650^\circ\text{C}$ and 250 $\mu\text{m}/650^\circ\text{C}$, resp.) and for 250 μm hot pressed powder at 450°C (250 $\mu\text{m}/450^\circ\text{C}$).

much higher ZT values, compared to the nonhomogenized 450°C hot pressing condition, were obtained, exhibiting very high maximal values of ~ 1.6 , which are among the highest so far reported for any p -type thermoelectric material. No practical differences were observed between the “50 μm ” and “250 μm ” conditions following 650°C hot pressing, probably due to a compensation of the slightly non-optimized carrier concentration, obtained for the “50 μm ” powder due to the previously explained strain induced compensation effect, by the lower lattice conductivity values of this sample, which were associated with the higher population of low ($<300\text{ nm}$) dimensional powder domains.

4. Conclusions

In the current research the $(\text{GeTe})_{0.95}(\text{Bi}_2\text{Te}_3)_{0.05}$ p -type thermoelectric composition was investigated following various processing routes for powdering and consolidation. High energetic ball milling at 700 RPM resulted in large XRD peaks broadening and even some amorphization. However hand crushing and sieving to a maximal 250 μm and 50 μm powder agglomerates resulted in crystalline powder particles, composed of much finer powder domains of less than 300 nm. The higher population of these powder domains resulted in lower lattice thermal conductivity for the 50 μm (compared to the 250 μm) powder. However, the higher strains associated with the increased mechanical force required for crushing the 50 μm powder into the desired size resulted in some reduction of the overall carrier concentration due to the strain induced compensation effect. Compensation of these two opposite effects resulted in similar very high maximal ZT values of up to 1.6 following consolidation, of both the 50 and 250 μm powder agglomerates, at 650°C, values which were found to be much higher than those obtained

following the 450°C hot pressing condition. In the latter, a nonhomogenized matrix was attributed to lower diffusion rates of the involved components at this lower hot pressing temperature. The maximal ZT value of ~ 1.6 obtained following 650°C hot pressing is among the highest ever reported for any p -type thermoelectric material. Following the above conclusion, it seems possible to further enhance the obtained ZT values by annealing of the “50 μm ” powder following the hand crushing procedure, for relieving the associated strains, prior the 650°C hot pressing procedure. Nevertheless, the annealing temperature should be carefully controlled for avoiding any undesired grain growth reactions. In this case, electronic transport properties similar to those obtained for the “250 μm ” powder combined with the low κ_L values obtained for the “50 μm ” powder, and consequently higher ZT values, are expected.

Conflict of Interests

The authors declare that there is no conflict of interests regarding the publication of this paper.

Acknowledgment

The work was partially supported by the EC FP7 *PowerDriver* Project.

References

- [1] J. Sariel, I. Dahan, and Y. Gelbstein, “Rhombohedral-cubic phase transition characterization of $(\text{Pb},\text{Ge})\text{Te}$ using high-temperature XRD,” *Powder Diffraction*, vol. 23, no. 2, pp. 137–140, 2008.
- [2] Y. Gelbstein, Y. Rosenberg, Y. Sadia, and M. P. Dariel, “Thermoelectric properties evolution of spark plasma sintered $(\text{Ge}_{0.6}\text{Pb}_{0.3}\text{Sn}_{0.1})\text{Te}$ following a spinodal decomposition,” *Journal of Physical Chemistry C*, vol. 114, no. 30, pp. 13126–13131, 2010.
- [3] Y. Gelbstein, B. Dado, O. Ben-Yehuda, Y. Sadia, Z. Dashevsky, and M. P. Dariel, “Highly efficient Ge-Rich $\text{Ge}_x\text{Pb}_{1-x}\text{Te}$ thermoelectric alloys,” *Journal of Electronic Materials*, vol. 39, no. 9, pp. 2049–2052, 2010.
- [4] Y. Gelbstein, B. Dado, O. Ben-Yehuda, Y. Sadia, Z. Dashevsky, and M. P. Dariel, “High thermoelectric figure of merit and nanostructuring in bulk p -type $\text{Ge}_x(\text{Sn}_y\text{Pb}_{1-y})_{1-x}\text{Te}$ alloys following a spinodal decomposition reaction,” *Chemistry of Materials*, vol. 22, no. 3, pp. 1054–1058, 2010.
- [5] Y. Gelbstein, J. Davidow, S. N. Girard, D. Y. Chung, and M. Kanatzidis, “Controlling metallurgical phase separation reactions of the $\text{Ge}_{0.87}\text{Pb}_{0.13}\text{Te}$ alloy for high thermoelectric performance,” *Advanced Energy Materials*, vol. 3, pp. 815–820, 2013.
- [6] D. I. Bletskan, “Phase equilibrium in the system AIV-BVI—part II: systems germanium-chalcogen,” *Journal of Ovonic Research*, vol. 1, no. 5, pp. 53–60, 2005.
- [7] T. Caillat, M. Carle, D. Perrin, H. Scherrer, and S. Scherrer, “Study of the Bi-Sb-Te ternary phase diagram,” *Journal of Physics and Chemistry of Solids*, vol. 53, no. 2, pp. 227–232, 1992.
- [8] Y. Gelbstein, Z. Dashevsky, and M. P. Dariel, “High performance n -type PbTe -based materials for thermoelectric applications,” *Physica B*, vol. 363, no. 1–4, pp. 196–205, 2005.

- [9] Y. Gelbstein, Z. Dashevsky, and M. P. Dariel, "Powder metallurgical processing of functionally graded p - $\text{Pb}_{1-x}\text{Sn}_x\text{Te}$ materials for thermoelectric applications," *Physica B*, vol. 391, no. 2, pp. 256–265, 2007.
- [10] Y. Gelbstein, Z. Dashevsky, and M. P. Dariel, "Highly efficient bismuth telluride doped p -type $\text{Pb}_{0.13}\text{Ge}_{0.87}\text{Te}$ for thermoelectric applications," *Physica Status Solidi*, vol. 1, no. 6, pp. 232–234, 2007.
- [11] N. Bomshtein, G. Spiridonov, Z. Dashevsky, and Y. Gelbstien, "Thermoelectric, structural, and mechanical properties of spark-plasma-sintered submicro- and microstructured p -Type $\text{Bi}_{0.5}\text{Sb}_{1.5}\text{Te}_3$," *Journal of Electronic Materials*, vol. 41, no. 6, pp. 1546–1553, 2012.
- [12] Y. Gelbstein, O. Ben-Yehuda, Z. Dashevsky, and M. P. Dariel, "Phase transitions of p -type $(\text{Pb},\text{Sn},\text{Ge})\text{Te}$ -based alloys for thermoelectric applications," *Journal of Crystal Growth*, vol. 311, no. 18, pp. 4289–4292, 2009.
- [13] Y. Gelbstein, O. Ben-Yehuda, E. Pinhas et al., "Thermoelectric properties of $(\text{Pb},\text{Sn},\text{Ge})\text{te}$ -based alloys," *Journal of Electronic Materials*, vol. 38, no. 7, pp. 1478–1482, 2009.

Research Article

An Optimization of Composition Ratio among Triple-Filled Atoms in $\text{In}_{0.3-x-y}\text{Ba}_x\text{Ce}_y\text{Co}_4\text{Sb}_{12}$ System

So-Young Kim,^{1,2} Soon-Mok Choi,³ Won-Seon Seo,¹ Young Soo Lim,¹
Soonil Lee,¹ Il-Ho Kim,⁴ and Hyung Koun Cho²

¹ Energy and Environmental Division, Korea Institute of Ceramic Engineering and Technology (KICET), Seoul 233-5, Republic of Korea

² School of Advanced Materials Science and Engineering, Sungkyunkwan University, Suwon, Gyeonggi-do 440-746, Republic of Korea

³ School of Energy, Materials and Chemical Engineering, Korea University of Technology and Education, Cheonan, Chungnam 330-708, Republic of Korea

⁴ Department of Materials Science and Engineering, Korea National University of Transportation, Chungju, Chungbuk 380-702, Republic of Korea

Correspondence should be addressed to Soon-Mok Choi; smchoi@koreatech.ac.kr

Received 13 June 2013; Revised 9 October 2013; Accepted 8 November 2013

Academic Editor: Hyung-Ho Park

Copyright © 2013 So-Young Kim et al. This is an open access article distributed under the Creative Commons Attribution License, which permits unrestricted use, distribution, and reproduction in any medium, provided the original work is properly cited.

Bulk nanostructured materials are important as energy materials. Among thermoelectric materials, the skutterudite system of CoSb_3 is a representative material of bulk nanostructured materials. Filling a skutterudite structure with atoms that have different localized frequencies (also known as triple filling) was reported to be effective for lowering thermal conductivity. Among studies representing superior power factors, In-filled skutterudite systems showed higher Seebeck coefficients. This study sought to optimize the composition ratio among the triple-filled atoms in an $\text{In}_{0.3-x-y}\text{Ba}_x\text{Ce}_y\text{Co}_4\text{Sb}_{12}$ system. The composition dependence of the thermoelectric properties was investigated for specimens with different ratios among the three kinds of filler atoms in the $\text{In}_{0.3-x-y}\text{Ba}_x\text{Ce}_y\text{Co}_4\text{Sb}_{12}$ system. In addition, the process variables were carefully optimized for filled skutterudite systems to obtain a maximum ZT value.

1. Introduction

Bulk nanostructured materials are a key research topic as energy materials. Materials for energy applications should satisfy the needs of both high conversion efficiency and large power output. Nanostructures are required for the high performance of materials, but bulk materials are needed to produce large power output. In thermoelectric materials, the skutterudite system found in CoSb_3 is a representative material of bulk nanostructured materials [1, 2]. For example, high-performance bulk nanostructured materials have been manufactured using this system by filling the Sb-dodecahedron voids in the CoSb_3 skutterudites with foreign ions such as rare-earth elements, alkalines, and alkaline-earth metals (thereby forming filled skutterudites). These weakly bound filler atoms with their independent vibrational modes were reported to interact with the normal modes of the

structure and suppress thermal conductivity dramatically [2]. The efficiency of a thermoelectric material is determined by its dimensionless thermoelectric figure-of-merit $ZT = S^2\sigma T\kappa^{-1}$, where S , σ , κ , and T are the Seebeck coefficient, electrical conductivity, total thermal conductivity, and absolute temperature, respectively. Therefore, good thermoelectric materials should have a high power factor ($\text{PF} = S^2\sigma$) value and a low thermal conductivity value. For this reason, CoSb_3 -based skutterudites have stimulated much scientific interest.

These filler atoms have been reported to play many roles. When the filler atoms are doped into the skutterudite system, they make chemical bonds with Sb ions. They can act as donor ions in an n -type CoSb_3 matrix, increasing carrier concentration [3, 4]. The filler atoms can also serve as a phonon scattering center, suppressing thermal conductivity. Filling a skutterudite structure with atoms that have different localized frequencies (triple filling) has also been reported

to be effective for lowering thermal conductivity [2–4]. The filler atoms can also enhance the Seebeck coefficients of filled CoSb_3 skutterudite system [5–7], an effect which has been reported many times, especially for the In-filled CoSb_3 skutterudite system. Among these studies representing superior power factors, In-filled skutterudite specimens [5–7] showed higher Seebeck coefficients than In-free filled skutterudite systems [8–14].

In this study, we sought to optimize the composition ratio among triple-filled atoms in an $\text{In}_{0.3-x-y}\text{Ba}_x\text{Ce}_y\text{Co}_4\text{Sb}_{12}$ system. Shi et al. and Yang et al. [3, 4] reported that multiple filling (filling with many ions that have different localized frequencies) might be effective in further lowering thermal conductivity. This study designed triple-filled compositions in the In-filler system $\text{In}_{0.3-x-y}\text{Ba}_x\text{Ce}_y\text{Co}_4\text{Sb}_{12}$, as Ba and Ce have very different resonance frequencies (54 cm^{-1} for Ce and 93 cm^{-1} for Ba) [6]. In many previous studies, the optimized filling amount was reported to be 0.3 ($\text{R}_{0.3}\text{Co}_4\text{Sb}_{12}$, R = filler atoms) for the filled skutterudite system [6, 13], so the filler amount was fixed at 0.3 ($\text{In}_{0.3-x-y}\text{Ba}_x\text{Ce}_y\text{Co}_4\text{Sb}_{12}$) and only the ratios among the filler atoms were varied. The composition dependence of the thermoelectric properties was investigated for specimens with different ratios among the three kinds of filler atoms.

In addition, previous studies noted the need for the process variables to be carefully tuned for filled-skutterudite systems, and especially for rare-earth and alkali-earth filled systems [15, 16]. A higher temperature melting and aging process should be used for filled skutterudites than intrinsic skutterudites. The phase-formation reaction ($\gamma\text{-CoSb}_3 + \text{Sb} \rightarrow \delta\text{-CoSb}_3$) may occur at an elevated temperature in filled-skutterudite systems [15–17]. The optimized process conditions were determined for synthesizing the $\delta\text{-CoSb}_3$ single phase without the $\gamma\text{-CoSb}_3$ phase to acquire samples with a maximum ZT value.

2. Experimental Procedure

Multiple-filled skutterudite samples $\text{In}_{0.3-x-y}\text{Ba}_x\text{Ce}_y\text{Co}_4\text{Sb}_{12}$ were synthesized by a combination of induction melting and spark plasma sintering (SPS). The starting materials were high-purity In (99.999% shot), BaSb_3 (99.98% ingot), Ce (99.999% powder), Co (99.95% slug), and Sb (99.999% shot), which were weighed according to the required stoichiometric ratio and loaded into carbon-coated quartz ampoules. The quartz ampoules were sealed under a vacuum of 10^{-3} Torr. The encapsulated samples were melted by using a radio frequency induction furnace and quenched during solidification to prevent phase separation. The ingots were then encapsulated in a vacuum again and annealed at 973 K for five days to form a homogeneous skutterudite phase ($\delta\text{-CoSb}_3$). The obtained ingots were pulverized into fine powders, followed by SPS in a graphite die at 963 K under 50 MPa of pressure for ten minutes in a vacuum. The prepared samples were sliced with a low-speed diamond saw and then polished.

The phases of the powders were analyzed using X-ray diffraction (XRD) over a 2θ range of $10\text{--}90^\circ$ (D/MAX-2500/PC, Rigaku, Japan, $\text{CuK}\alpha$ radiation). Microstructure of the bulk specimens was observed by using a scanning electron microscopy (SEM, JSM6700F, JEOL, Japan) and a high-resolution transmission electron microscopy (HRTEM, JEM4010, JEOL, Japan). The electrical conductivity and the Seebeck coefficient were measured by means of the four-point probe method using a thermoelectric property measurement system (RZ2001i, Ozawa Science, Japan).

Thermal conductivity was evaluated from the density, the specific heat, and the thermal diffusivity by use of a laser flash method (Netzsch). The Hall coefficient and the carrier concentration were measured based on the Van der Pauw method at room temperature (Resi Test 8300, Toyo Corporation). All of the aforementioned thermoelectric property measurements except Hall coefficient were performed within the temperature range of 300 to 800 K.

3. Results and Discussion

The composition dependence of the thermoelectric properties was investigated for specimens with different ratios among the three kinds of filler atoms in the $\text{In}_{0.3-x-y}\text{Ba}_x\text{Ce}_y\text{Co}_4\text{Sb}_{12}$ system. Figure 1(a) shows a schematic phase diagram of the compositions investigated in this study. Even though low concentration of the Ba and Ce atoms were included in these compositions, the process conditions were appropriately optimized for these rare-earth and alkali-earth filled skutterudites. As a result, the four compositions were indexed as a CoSb_3 skutterudite single phase without any secondary phases like the CoSb_2 phase as shown in Figure 1(b).

The Seebeck coefficients ($|S|$) for all the compositions manufactured at high temperatures were larger than $200\text{ }\mu\text{V/K}$ as can be seen in Figure 2(a). This large Seebeck coefficient is a characteristic of In-filled skutterudite systems. Three possible explanations were reported for the large Seebeck coefficients in the In-filled skutterudite systems. Li et al. reported that nano-dispersed second phase might enhance the Seebeck coefficient of In-filled skutterudites [5]. They reported that InSb phase was dispersed at the boundaries and that this nano-dispersed phase might reduce the mobility of the charge carriers and thereby enhance the Seebeck coefficient of the thermoelectric material. The Seebeck coefficient is a function of the carrier mobility and concentration as follows [18]:

$$S = \frac{\pi^2}{3} \frac{k_B}{q} k_B T \left\{ \frac{d[\ln(\sigma(E))]}{dE} \right\}_{E=E_F} \quad (1)$$

$$= \frac{\pi^2}{3} \frac{k_B}{q} k_B T \left\{ \frac{1}{n} \frac{dn(E)}{dE} + \frac{1}{\mu} \frac{d\mu(E)}{dE} \right\}_{E=E_F},$$

where, S is the Seebeck coefficient; μ is the mobility of the carrier; and n is the carrier concentration. As shown in (1), the Seebeck coefficient was inversely proportional to the mobility. However, it was hard to find the InSb secondary phase by means of XRD and SEM analyses in this study as shown

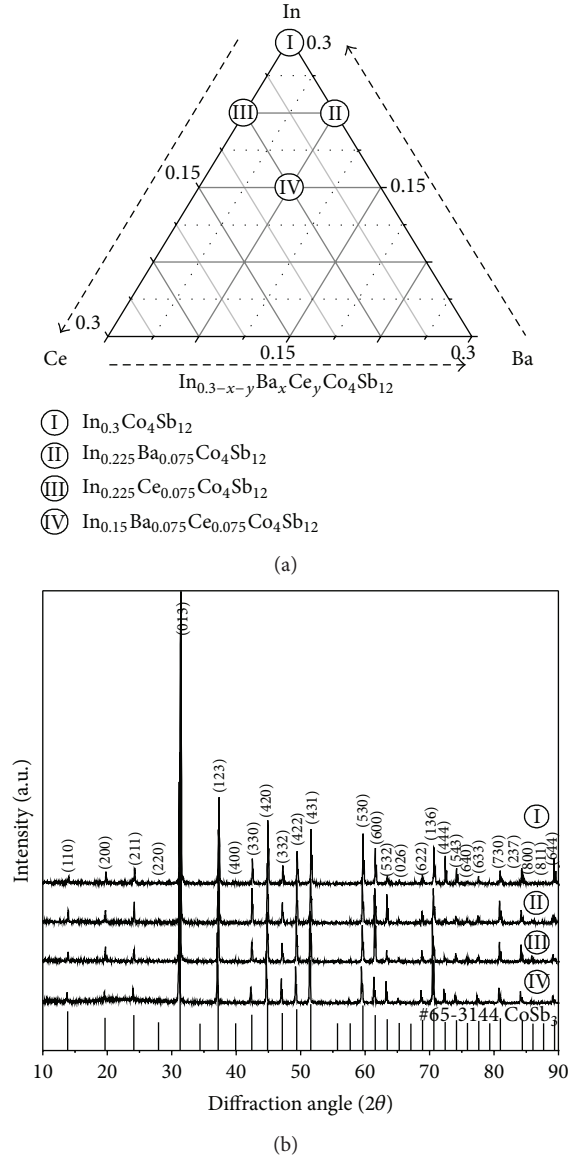


FIGURE 1: (a) A schematic phase diagram of four compositions investigated in the $\text{In}_{0.3-x-y}\text{Ba}_x\text{Ce}_y\text{Co}_4\text{Sb}_{12}$ filled skutterudite system and (b) X-ray diffraction patterns of the compositions.

in Figure 3(a). The underlimit of detection size or amount of secondary nanoparticles also might be the reason of not observed the nano-dispersed secondary phase. As shown in Figure 3(b), however, a small amount of secondary phase with smaller size than the reported scale [5] was detected from a TEM analysis. This means that the In-filler could be doped into the lattice in this study. The reason for the different results about InSb secondary phase is not clear yet. Different process conditions could be one of the reasons for the difference between this work and other reports [5]. More precise analysis for the relationship between process conditions and amount of the InSb secondary phase in various filled skutterudite systems should be carried out for better understanding the In and InSb effects.

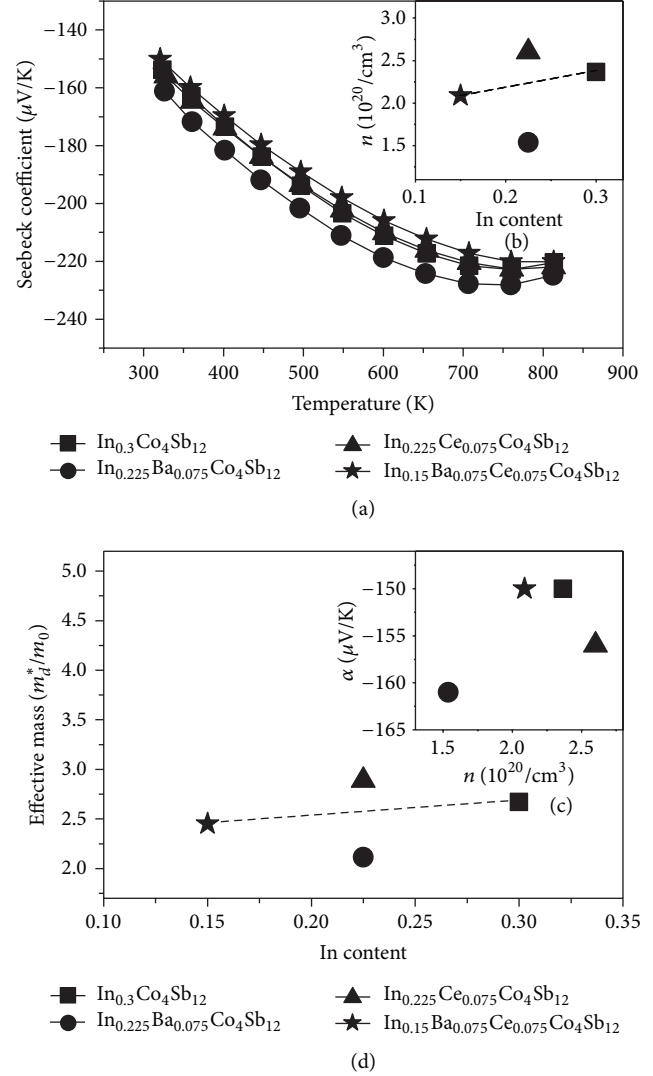


FIGURE 2: (a) Temperature dependence of the Seebeck coefficients, (b) In-content dependence of a carrier concentration, (c) In-content dependence of the Seebeck coefficient, and (d) In-content dependence of an effective mass value.

Shi et al. emphasized the electronegativity values (χ) of the filler atoms [19]. They reported that if the difference of electronegativity values is smaller than 0.8 between a filler atom and Sb, the filler atom cannot be doped into the void of CoSb_3 skutterudite structure. The electronegativity of an In atom (1.7) is nearly the same as that of an Sb atom (1.9). As a result, they reported that an In-filler atom cannot fill the void of the CoSb_3 structure. If the In-filler atoms cannot perform the role as a donor, the low carrier concentration could increase the Seebeck coefficient in the In-filled skutterudite system. This is because the Seebeck coefficient is inversely proportional to the carrier mobility and the carrier concentration as shown in (1). However, the carrier concentration value increased in proportion to the amount of In-filler as shown in Figure 2(b). This result shows

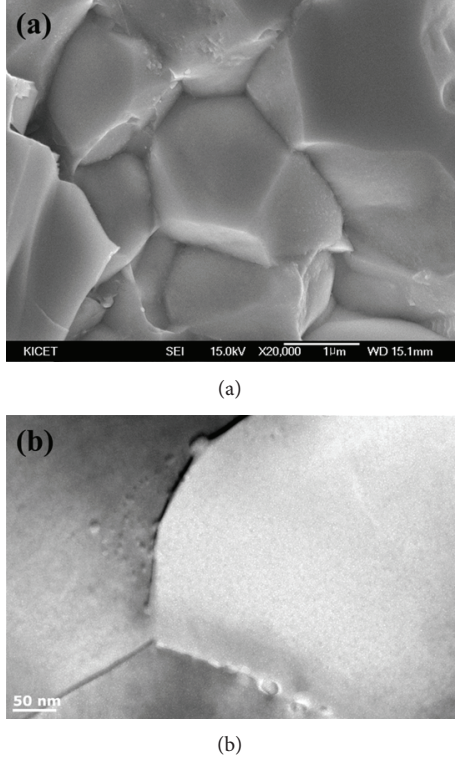


FIGURE 3: (a) A scanning electron microscopy image and (b) a high-resolution transmission electron microscopy image of the bulk $\text{In}_{0.15}\text{Ba}_{0.075}\text{Ce}_{0.075}\text{Co}_4\text{Sb}_{12}$ specimens.

that the In-filler ($\chi = 1.7$) in this study can perform the role as a donor just as in the cases of Ba ($\chi = 0.9$) and Ce ($\chi = 1.1$).

Another possibility is that the In-filler can increase the effective mass of electrons in the skutterudite system. In this study, the Seebeck coefficients show no linear relationship to the carrier concentration as shown in Figure 2(c). Even though the carrier concentration was highest in the $\text{In}_{0.225}\text{Ce}_{0.075}\text{Co}_4\text{Sb}_{12}$ composition, a large Seebeck coefficient was measured in this composition. This lack of a relationship between the carrier concentration and the Seebeck coefficient suggests that the In-filler has an additional effects on the Seebeck coefficients of this triple-filled system. In general, the Seebeck coefficient is proportional to the effective mass of the carriers [15–18]:

$$S = \frac{8\pi^2 k_B^2 T}{3qh^2} m_d^* \left(\frac{\pi}{3n} \right)^{2/3}, \quad (2)$$

where, S is the Seebeck coefficient; k_B is Boltzmann's constant; T is the absolute temperature; q is the carrier charge; h is Planck's constant; m_d^* is the effective mass; and n is the carrier concentration. Thus, an increase in the effective mass can cause an increase in the Seebeck coefficient. Figure 2(d) shows that the effective mass was nearly proportional to the amount of In-filler. The increased effective mass can help explaining the large Seebeck coefficients of the In-filled skutterudites system. As a result, it is anticipated that the large Seebeck coefficients of the In-filled system are ascribed to both the

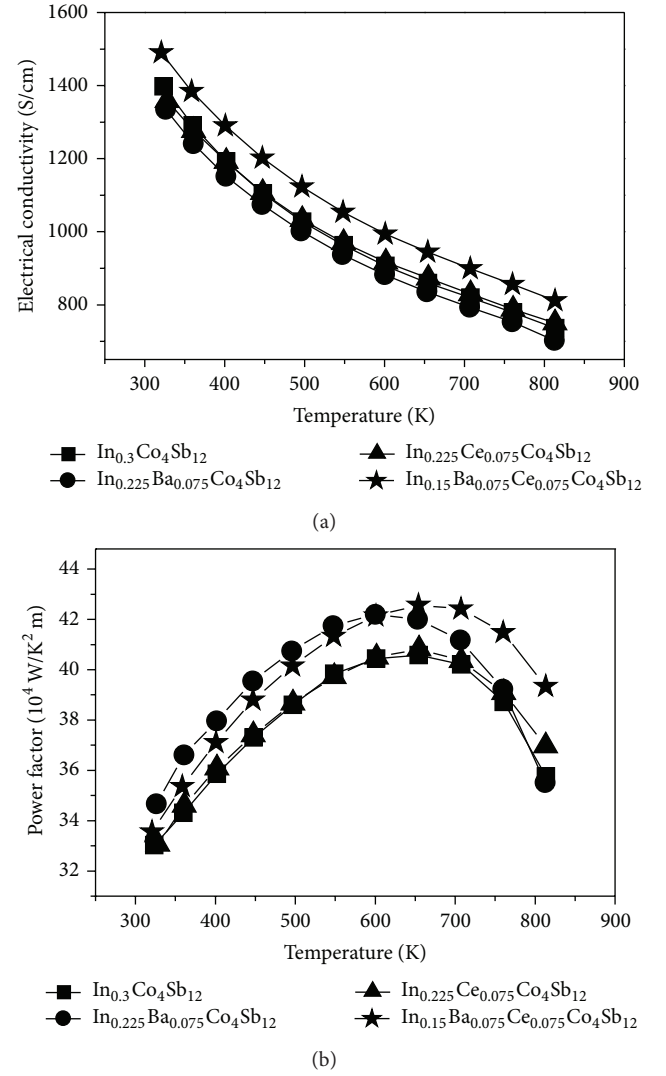


FIGURE 4: (a) Temperature dependence of electrical conductivities and (b) power factor values for the $\text{In}_{0.3-x-y}\text{Ba}_x\text{Ce}_y\text{Co}_4\text{Sb}_{12}$ filled skutterudite compounds.

effect of the InSb secondary phase and the increased effective mass. More detailed study should follow to determine which of the two is the main factor causing the large Seebeck coefficients in In-filled systems.

The electrical conductivity values were inversely proportional to the Seebeck coefficients of the triple-filled skutterudites as shown in Figure 4(a). As mentioned above, the In-filler can perform the role as a donor in this study. Therefore, the carrier concentration could decrease when In^{3+} was substituted by Ba^{2+} , since the charge state of the donor Ba^{2+} is lower than that of In^{3+} . As a result, the electrical conductivity of the $\text{In}_{0.225}\text{Ba}_{0.075}\text{Co}_4\text{Sb}_{12}$ composition was lower than that of the $\text{In}_{0.3}\text{Co}_4\text{Sb}_{12}$ composition. After this, when Ce^{3+} was additionally substituted in for In^{3+} , the electrical conductivity of the $\text{In}_{0.15}\text{Ba}_{0.075}\text{Ce}_{0.075}\text{Co}_4\text{Sb}_{12}$ composition was higher than that of the $\text{In}_{0.225}\text{Ba}_{0.075}\text{Co}_4\text{Sb}_{12}$ composition. This increased electrical conductivity can be explained by the

fact that the charge state of the Ce ion was frequently reported to be $4+$ [20]. Because of the increased donor effect, the carrier concentration of the $\text{In}_{0.15}\text{Ba}_{0.075}\text{Ce}_{0.075}\text{Co}_4\text{Sb}_{12}$ composition was higher than that of the $\text{In}_{0.225}\text{Ba}_{0.075}\text{Co}_4\text{Sb}_{12}$ composition as shown in Figure 2(b). The lower conductivity of the $\text{In}_{0.225}\text{Ce}_{0.075}\text{Co}_4\text{Sb}_{12}$ composition is difficult to explain and may be due to high melting point of Ce atoms. As mentioned in Section 1, the process variables should be carefully tuned for filled-skutterudite systems, especially for rare-earth and alkali-earth filled systems [15, 16]. A higher-temperature melting and aging process should be used for filled-skutterudites than for intrinsic skutterudites, making it difficult to manufacture a CoSb_3 skutterudite single phase from a Ce-filled composition. Further study is needed to explain the low electrical conductivity of a Ce-filled system. One more important factor is that the electrical conductivity of the $\text{In}_{0.15}\text{Ba}_{0.075}\text{Ce}_{0.075}\text{Co}_4\text{Sb}_{12}$ composition was even higher than that of the $\text{In}_{0.3}\text{Co}_4\text{Sb}_{12}$ composition. The effective mass of the $\text{In}_{0.3}\text{Co}_4\text{Sb}_{12}$ composition was larger than that of the other compositions as shown in Figure 2(d). The largest effective mass $\text{In}_{0.3}\text{Co}_4\text{Sb}_{12}$ composition can cause low electrical conductivity in spite of its highest carrier concentration.

In general, the electrical conductivity of thermoelectric materials is inversely proportional to their Seebeck coefficients. Although electrical conductivity of $\text{In}_{0.15}\text{Ba}_{0.075}\text{Ce}_{0.075}\text{Co}_4\text{Sb}_{12}$ was higher than other compositions, the Seebeck coefficient was lowest as can be seen in Figure 2(a). However, degree of reduction in the Seebeck coefficient is smaller than increment in electrical conductivity. As a result, the highest value of power factor higher than $42 \times 10^{-4} \text{ W/K}^2 \text{ m}$ was obtained in the $\text{In}_{0.15}\text{Ba}_{0.075}\text{Ce}_{0.075}\text{Co}_4\text{Sb}_{12}$ composition as shown in Figure 4(b).

Figure 5 shows the temperature dependence of the total thermal conductivity, the electronic thermal conductivity, and the lattice thermal conductivity of the samples. The thermal conductivity is the sum of the lattice thermal conductivity and electronic thermal conductivity as can be seen in the following:

$$\kappa = \kappa_L + \kappa_{el} = \kappa_L + L\sigma T, \quad (3)$$

where, κ_L , κ_{el} , L , σ , and T are the lattice thermal conductivity, the electronic thermal conductivity, the Lorenz number ($2.45 \times 10^{-8} \text{ W}\Omega/\text{K}^2$), the electrical conductivity, and the absolute temperature, respectively. κ_{el} can be obtained by means of the Wiedemann-Franz Law; $\kappa_{el} = L\sigma T$ [21], and κ_L can be determined by $\kappa_L = \kappa - \kappa_{el}$.

As shown in Figure 5(a), the total thermal conductivity was lowest in the $\text{In}_{0.3}\text{Co}_4\text{Sb}_{12}$ composition. The thermal conductivity of the $\text{In}_{0.15}\text{Ba}_{0.075}\text{Ce}_{0.075}\text{Co}_4\text{Sb}_{12}$ composition was higher than that of the $\text{In}_{0.3}\text{Co}_4\text{Sb}_{12}$ composition. This was because the electrical conductivity of the $\text{In}_{0.15}\text{Ba}_{0.075}\text{Ce}_{0.075}\text{Co}_4\text{Sb}_{12}$ composition was the highest among all of the compositions. In spite of its highest electrical conductivity, the lattice thermal conductivity of the $\text{In}_{0.15}\text{Ba}_{0.075}\text{Ce}_{0.075}\text{Co}_4\text{Sb}_{12}$ composition was the lowest in this study. This low lattice thermal conductivity can be explained by the triple rattlers effect. Each filler atom was

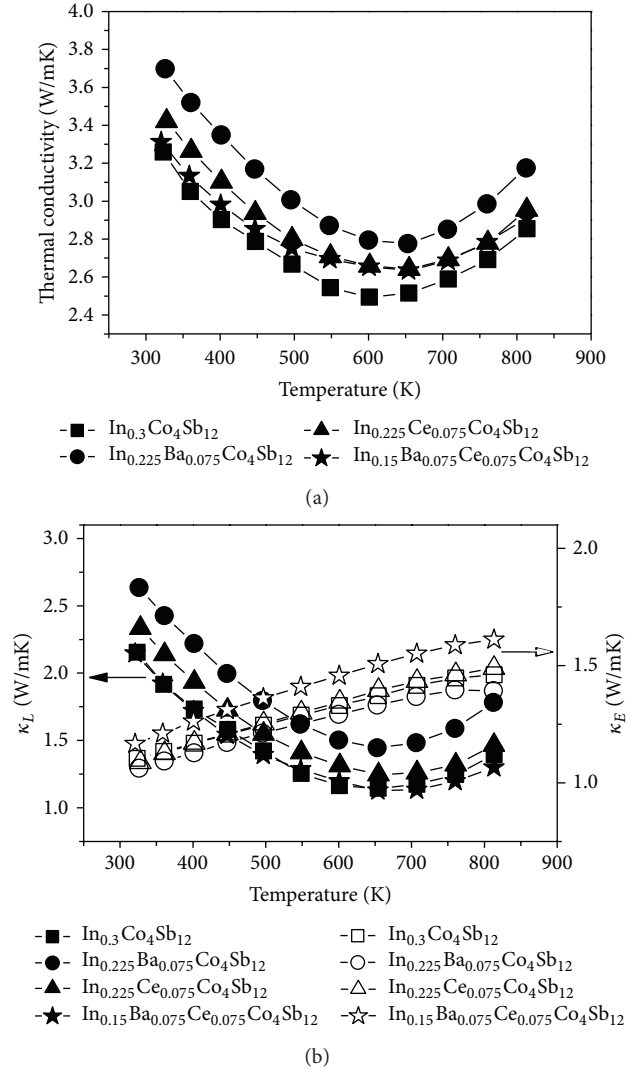


FIGURE 5: (a) Thermal conductivities and (b) both lattice thermal conductivity (κ_L) and electronic thermal conductivity (κ_E) for the $\text{In}_{0.3-x-y}\text{Ba}_x\text{Ce}_y\text{Co}_4\text{Sb}_{12}$ filled skutterudite compounds.

reported to represent a phonon resonance scattering center near a particular frequency [3]. Scattering as wide a spectrum of normal phonons as possible could be the crucial factor when seeking to achieve a low κ_L [3]. Accordingly, filling the skutterudite structure with atoms that have different localized frequencies (triple-filling) was considered to be effective for lowering the κ_L value further [3]. Total thermal conductivity of the $\text{In}_{0.225}\text{Ba}_{0.075}\text{Co}_4\text{Sb}_{12}$ composition was the highest in this work in spite of the lowest electrical conductivity. In general, rattler atoms with low valence state ($2+$) and large ionic radius have been reported to show poor rattling effects in single rattler filled cases [22]. Ba^{2+} has a large ionic radius, so it is believed that the high lattice thermal conductivity of the $\text{In}_{0.225}\text{Ba}_{0.075}\text{Co}_4\text{Sb}_{12}$ composition is attributed to the Ba-filler. However, it is difficult to explain that the higher total thermal conductivity of the $\text{In}_{0.225}\text{Ce}_{0.075}\text{Co}_4\text{Sb}_{12}$ composition than that of the

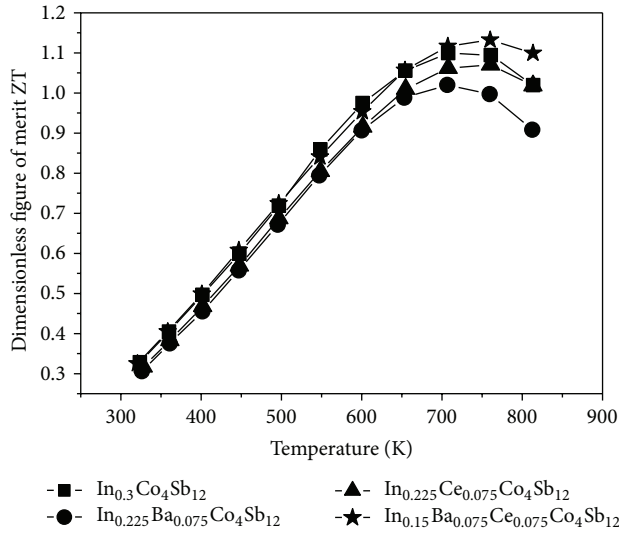


FIGURE 6: The dimensionless figure of merit (ZT) for the $\text{In}_{0.3-x-y}\text{Ba}_x\text{Ce}_y\text{Co}_4\text{Sb}_{12}$ filled skutterudite compounds.

$\text{In}_{0.15}\text{Ba}_{0.075}\text{Ce}_{0.075}\text{Co}_4\text{Sb}_{12}$ and $\text{In}_{0.3}\text{Co}_4\text{Sb}_{12}$ compositions. Tang et al. reported that the total thermal conductivity increased with increasing Ce-filling amount when Ce-filling content was higher than filling limit [23]. They also found that the filling content limit for Ce-filling case was lower than that of Ba-filling case. Further study is needed to explain the high thermal conductivity of a Ce-filled system.

As a result, a maximum ZT value of 1.13 was obtained in the $\text{In}_{0.15}\text{Ba}_{0.075}\text{Ce}_{0.075}\text{Co}_4\text{Sb}_{12}$ composition as shown in Figure 6. The reasons for this high value seem to be attributable to the large Seebeck coefficient because of the In-filler atoms, high electrical conductivity due to the Ce donor effect, and low thermal conductivity by the triple-filled rattlers.

4. Conclusions

The composition dependence of the thermoelectric properties was investigated for specimens with different ratios among three different filler atoms in the $\text{In}_{0.3-x-y}\text{Ba}_x\text{Ce}_y\text{Co}_4\text{Sb}_{12}$ system. The process conditions for the rare-earth and alkali-earth filled skutterudites were appropriately optimized. CoSb_3 skutterudite single phase without any secondary phases like CoSb_2 phase was obtained for all compositions used in this study.

The Seebeck coefficients ($|S|$) of all the compositions manufactured at high temperatures were larger than $200 \mu\text{V/K}$. Both the effect of the InSb secondary phase and the increased effective mass value could be the causes of the large Seebeck coefficients observed in the In-filled skutterudites systems. The electrical conductivity of the $\text{In}_{0.15}\text{Ba}_{0.075}\text{Ce}_{0.075}\text{Co}_4\text{Sb}_{12}$ composition was higher than that of the other compositions. This high electrical conductivity can be explained via the donor effect of the Ce ion, as the charge state of the Ce ion was frequently reported to be $4+$. In spite of its high electrical conductivity, the lattice thermal conductivity of the $\text{In}_{0.15}\text{Ba}_{0.075}\text{Ce}_{0.075}\text{Co}_4\text{Sb}_{12}$ composition

was lowest in this study owing to the triple rattlers that play a role as a phonon resonance scattering center.

Since the ratio of filler atoms and synthesizing process conditions were optimized in an $\text{In}_{0.3-x-y}\text{Ba}_x\text{Ce}_y\text{Co}_4\text{Sb}_{12}$ system, a maximum ZT value of 1.13 was obtained in the $\text{In}_{0.15}\text{Ba}_{0.075}\text{Ce}_{0.075}\text{Co}_4\text{Sb}_{12}$ composition. Accordingly, it seems that the In and Ce increases the Seebeck coefficient and electrical conductivity, respectively, and the triple filled rattlers lower the thermal conductivity.

Conflict of Interests

The authors declare that there is no conflict of interests regarding the publication of this paper.

Acknowledgments

This work was supported by the Defense Acquisition Program Administration (DAPA) and the Agency for Defense Development (ADD) under the Contract no. UC120037GD, Republic of Korea. This work was also supported by a research program for new faculties in 2013 funded by Korea University of Technology and Education.

References

- [1] B. C. Sales, D. Mandrus, and R. K. Williams, "Filled skutterudite antimonides: a new class of thermoelectric materials," *Science*, vol. 272, no. 5266, pp. 1325–1328, 1996.
- [2] V. Keppens, D. Mandrus, B. C. Sales et al., "Localized vibrational modes in metallic solids," *Nature*, vol. 395, no. 6705, pp. 876–878, 1998.
- [3] X. Shi, J. R. Salvador, J. Yang, and H. Wang, "Thermoelectric properties of n-type multiple-filled skutterudites," *Journal of Electronic Materials*, vol. 38, no. 7, pp. 930–933, 2009.
- [4] J. Yang, W. Zhang, S. Q. Bai, Z. Mei, and L. D. Chen, "Dual-frequency resonant phonon scattering in $\text{Ba}_x\text{R}_y\text{Co}_4\text{Sb}_{12}$ ($\text{R}=\text{La}$, Ce , and Sr)," *Applied Physics Letters*, vol. 90, no. 19, Article ID 192111, 2007.
- [5] H. Li, X. Tang, Q. Zhang, and C. Uher, "High performance $\text{In}_x\text{Ce}_y\text{Co}_4\text{Sb}_{12}$ thermoelectric materials with in situ forming nanostructured InSb phase," *Applied Physics Letters*, vol. 94, no. 10, Article ID 102114, 2009.
- [6] J. Y. Peng, J. He, Z. Su, P. N. Alboni, S. Zhu, and T. M. Tritt, "High temperature thermoelectric properties of double-filled $\text{In}_x\text{Yb}_y\text{Co}_4\text{Sb}_{12}$ skutterudites," *Journal of Applied Physics*, vol. 105, no. 8, Article ID 084907, 2009.
- [7] W. Y. Zhao, C. L. Dong, P. Wei et al., "Synthesis and high temperature transport properties of barium and indium double-filled skutterudites $\text{Ba}_x\text{In}_y\text{Co}_4\text{Sb}_{12-z}$," *Journal of Applied Physics*, vol. 102, no. 11, Article ID 113708, 2007.
- [8] H. Li, X. Tang, X. Su, Q. Zhang, and C. Uher, "Nanostructured bulk $\text{Yb}_x\text{Co}_4\text{Sb}_{12}$ with high thermoelectric performance prepared by the rapid solidification method," *Journal of Physics D*, vol. 42, no. 14, Article ID 145409, 2009.
- [9] J. R. Salvador, J. Yang, H. Wang, and X. Shi, "Double-filled skutterudites of the type $\text{Yb}_x\text{Ca}_y\text{Co}_4\text{Sb}_{12}$: synthesis and properties," *Journal of Applied Physics*, vol. 107, no. 4, Article ID 043705, 2010.

- [10] S. Q. Bai, Y. Z. Pei, L. D. Chen, W. Q. Zhang, X. Y. Zhao, and J. Yang, "Enhanced thermoelectric performance of dual-element-filled skutterudites $\text{Ba}_x\text{Ce}_y\text{Co}_4\text{Sb}_{12}$," *Acta Materialia*, vol. 57, no. 11, pp. 3135–3139, 2009.
- [11] X. Shi, H. Kong, C.-P. Li et al., "Low thermal conductivity and high thermoelectric figure of merit in n-type $\text{Ba}_x\text{Yb}_y\text{Co}_4\text{Sb}_{12}$ double-filled skutterudites," *Applied Physics Letters*, vol. 92, no. 18, Article ID 182101, 2008.
- [12] L. D. Chen, T. Kawahara, X. F. Tang et al., "Anomalous barium filling fraction and n-type thermoelectric performance of $\text{Ba}_y\text{Co}_4\text{Sb}_{12}$," *Journal of Applied Physics*, vol. 90, no. 4, pp. 1864–1868, 2001.
- [13] X. F. Tang, Q. J. Zhang, L. D. Chen, T. Goto, and T. Hirai, "Synthesis and thermoelectric properties of p-type-and n-type-filled skutterudite $\text{R}_y\text{M}_x\text{Co}_{4-x}\text{Sb}_{12}$ (R:Ce, Ba, Y,M:Fe, Ni)," *Journal of Applied Physics*, vol. 97, no. 9, Article ID 093712, 2005.
- [14] Z. Xiong, X. Chen, X. Zhao, S. Bai, X. Huang, and L. Chen, "Effects of nano- TiO_2 dispersion on the thermoelectric properties of filled-skutterudite $\text{Ba}_{0.22}\text{Co}_4\text{Sb}_{12}$," *Solid State Sciences*, vol. 11, no. 9, pp. 1612–1616, 2009.
- [15] J. K. Lee, S. M. Choi, W. S. Seo, D. I. Cheong, and I. H. Kim, "Determination of the thermoelectric properties in filled-skutterudite systems by controlling the process variables," *Japanese Journal of Applied Physics*, vol. 51, Article ID 09ML02, 5 pages, 2012.
- [16] J.-K. Lee, S.-M. Choi, W.-S. Seo, Y.-S. Lim, H.-L. Lee, and I.-H. Kim, "Thermoelectric properties of Spark Plasma Sintered $\text{In}_x\text{Yb}_y\text{La}_{0.3-x-y}\text{Co}_4\text{Sb}_{12}$ skutterudite system," *Renewable Energy*, vol. 42, pp. 36–40, 2012.
- [17] J.-K. Lee, S.-M. Choi, W.-S. Seo, H.-L. Lee, and I.-H. Kim, "Thermoelectric properties of the co-doped n-type CoSb_3 compound," *Journal of the Korean Physical Society*, vol. 57, no. 41, pp. 1010–1014, 2010.
- [18] J. P. Heremans, V. Jovovic, E. S. Toberer et al., "Enhancement of thermoelectric efficiency in PbTe by distortion of the electronic density of states," *Science*, vol. 321, no. 5888, pp. 554–557, 2008.
- [19] X. Shi, W. Zhang, L. D. Chen, and J. Yang, "Filling fraction limit for intrinsic voids in crystals: doping in skutterudites," *Physical Review Letters*, vol. 95, no. 18, Article ID 185503, 2005.
- [20] Y. Wang, Y. Sui, X. Wang, and W. Su, "Effects of substituting La^{3+} , Y^{3+} and Ce^{4+} for Ca^{2+} on the high temperature transport and thermoelectric properties of CaMnO_3 ," *Journal of Physics D*, vol. 42, no. 5, Article ID 055010, 2009.
- [21] C. Kittel, *Introduction to Solid State Physics*, John Wiley & Sons, New York, NY, USA, 1976.
- [22] P. F. Qiu, J. Yang, R. H. Liu et al., "High-temperature electrical and thermal transport properties of fully filled skutterudites $\text{RFe}_4\text{Sb}_{12}$ (R=Ca, Sr, Ba, La, Ce, Pr, Nd, Eu, and Yb)," *Journal of Applied Physics*, vol. 109, no. 6, Article ID 063713, 2011.
- [23] X. F. Tang, L. D. Chen, J. Wang, Q. J. Zhang, T. Goto, and T. Hirai, "Effects of filling atoms Ba, Ce, Y and substituting atoms Fe, Ni on lattice thermal conductivity of $\text{R}_y\text{M}_x\text{Co}_{4-x}\text{Sb}_{12}$," *Journal of Alloys and Compounds*, vol. 394, no. 1-2, pp. 259–264, 2005.

Research Article

Fabrication and Enhanced Thermoelectric Properties of Alumina Nanoparticle-Dispersed $\text{Bi}_{0.5}\text{Sb}_{1.5}\text{Te}_3$ Matrix Composites

Kyung Tae Kim and Gook Hyun Ha

Powder & Ceramic Materials Division, Korea Institute of Materials Science, 797 Changwon-daero, Seongsan-gu, Changwon-si, Gyeongnam 642-831, Republic of Korea

Correspondence should be addressed to Kyung Tae Kim; ktkim@kims.re.kr

Received 25 June 2013; Revised 14 September 2013; Accepted 14 October 2013

Academic Editor: Hyung-Ho Park

Copyright © 2013 K. T. Kim and G. H. Ha. This is an open access article distributed under the Creative Commons Attribution License, which permits unrestricted use, distribution, and reproduction in any medium, provided the original work is properly cited.

Alumina nanoparticle-dispersed bismuth-antimony-tellurium matrix ($\text{Al}_2\text{O}_3/\text{BST}$) composite powders were fabricated by using ball milling process of alumina nanoparticle about 10 nm and p-type bismuth telluride nanopowders prepared from the mechanochemical process (MCP). The fabricated $\text{Al}_2\text{O}_3/\text{BST}$ composite powders were a few hundreds of nanometer in size, with a clear $\text{Bi}_{0.5}\text{Sb}_{1.5}\text{Te}_3$ phase. The composite powders were consolidated into p-type bulk composite by spark plasma sintering process. High-resolution TEM images reveal that alumina nanoparticles were dispersed among the grain boundary or in the matrix grain. The sintered 0.3 vol.% $\text{Al}_2\text{O}_3/\text{BST}$ composite exhibited significantly improved power factor and reduced thermal conductivity in the temperature ranging from 293 to 473 K compared to those of pure BST. From these results, the highly increased ZT value of 1.5 was obtained from 0.3 vol.% $\text{Al}_2\text{O}_3/\text{BST}$ composite at 323 K.

1. Introduction

Bismuth telluride (Bi_2Te_3)-based alloys are very attractive thermoelectric (TE) materials due to their high energy conversion efficiency at ambient temperature for achieving power generation without requiring any driving parts or cooling systems in electronic devices [1]. It is well known that the TE conversion efficiency of thermoelectric devices is expressed as the dimensionless figure-of-merit, ZT, which is calculated from $T(\alpha^2/\rho\kappa)$, where T is the absolute temperature, α is the Seebeck coefficient, and ρ and κ are respectively the electrical resistivity and thermal conductivity. Thus, current researches have concentrated on obtaining a reduced thermal conductivity and increased electrical properties, respectively in order to enhance ZT values. Nanostructuring of the microstructure and the incorporation of nanoparticles in bismuth telluride TE alloys have been reported as efficient approaches to achieve high ZT value by controlling carrier and phonon transporting behaviors [2–5].

Recently, many researchers report that controlling electrical conductivity and/or the Seebeck coefficient can be

simultaneously improved by an electron filtering through the use of a composite structure consisting of TE materials and nanoinclusions such as SiC nanoparticles, and carbon nanotubes [6–10]. Furthermore, the concept of the reduction in the lattice thermal conductivity more than increasing electrical resistivity has been widely accepted to improve the ZT value, because phonons are effectively blocked while carriers pass through the dispersed nanoparticles below 10 nm in size due to the difference in the wavelengths between the phonons and carriers. However, most of the bismuth telluride matrix composite is based on binary Bi_2Te_3 -based materials [6, 8, 9]. There have been a few studies on achieving high ZT values of ternary Bi_2Te_3 matrix composite including the separately added nanoparticles.

In this study, we report thermoelectric properties of alumina nanoparticle-dispersed p-type $\text{Bi}_{0.5}\text{Sb}_{1.5}\text{Te}_3$ matrix composite fabricated by high-energy ball milling process and followed by spark plasma sintering (SPS) process. The composites sintered from 0.3 vol.% $\text{Al}_2\text{O}_3/\text{BST}$ composite powders show significantly increased ZT value, 1.5 compared to 1.1 of pure BST materials.

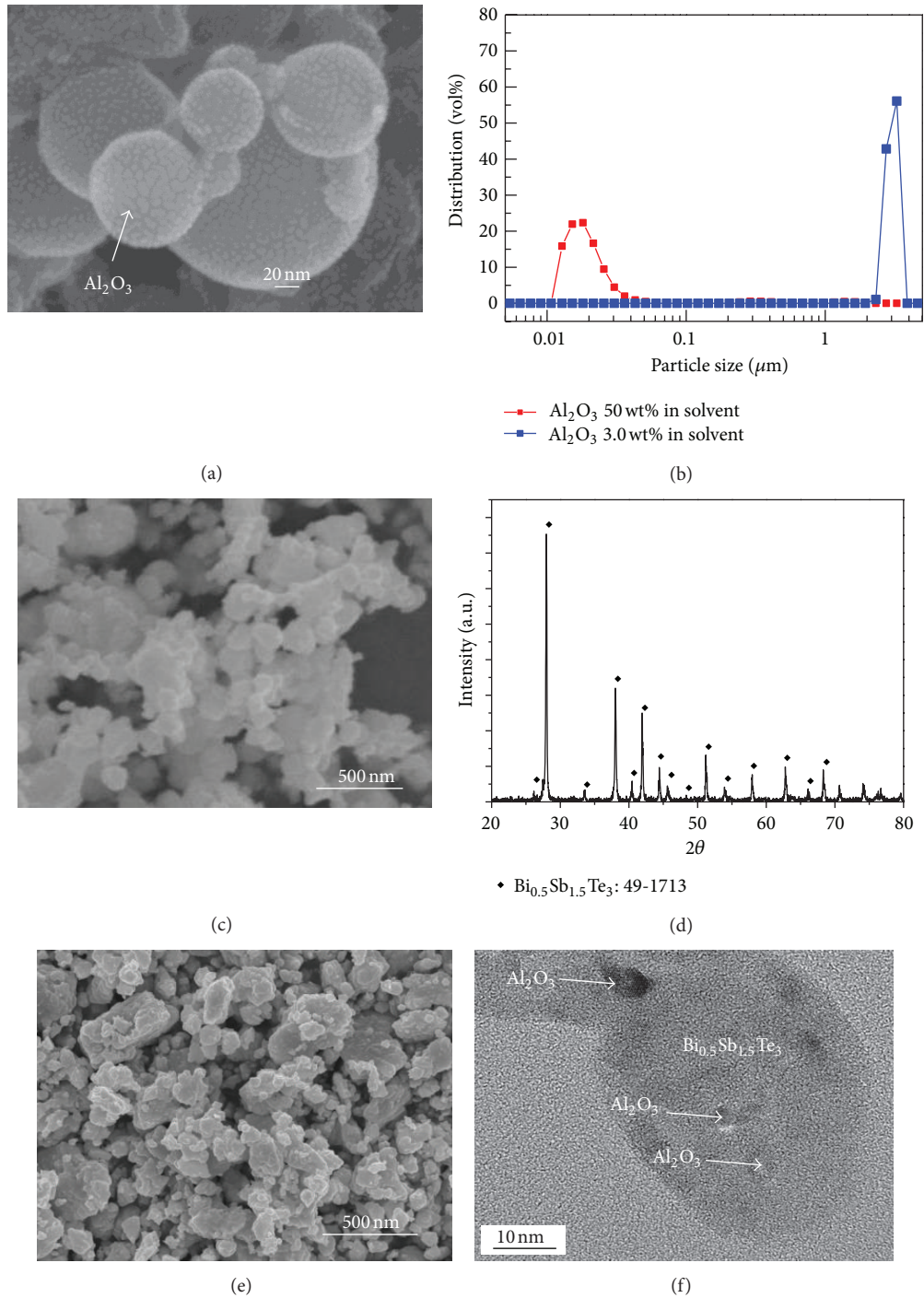


FIGURE 1: (a) FE-SEM image of Al_2O_3 nanoparticles used in this study, (b) size distribution of the nanoparticles in solvent with different concentration, (c) surface morphology of p-type $\text{Bi}_{0.5}\text{Sb}_{1.5}\text{Te}_3$ nanopowders prepared from MCP, (d) XRD patterns of fabricated p-type $\text{Bi}_{0.5}\text{Sb}_{1.5}\text{Te}_3$ nanopowders, (e) the surface morphology of the fabricated $\text{Al}_2\text{O}_3/\text{BST}$ composite powders, and (f) TEM image showing Al_2O_3 nanoparticles dispersed in BST matrix powders.

2. Experimental Procedure

Al_2O_3 nanoparticles used in this study have size of about 10 nm and α -phase. They were chemically treated into a stable colloidal solution in a solvent by adding a surfactant. We

used mechanochemical process to synthesize p-type Bi-Sb-Te (BST) powders with $\text{Bi}_{0.5}\text{Sb}_{1.5}\text{Te}_3$ phase from a solution of $\text{Bi}_2(\text{SO}_4)_3$, SbCl_3 , and TeO_2 powders that are supplied from byproducts of Cu refining process. During the MCP, Bi sulfate, Sb chloride, and Te oxide were homogeneously

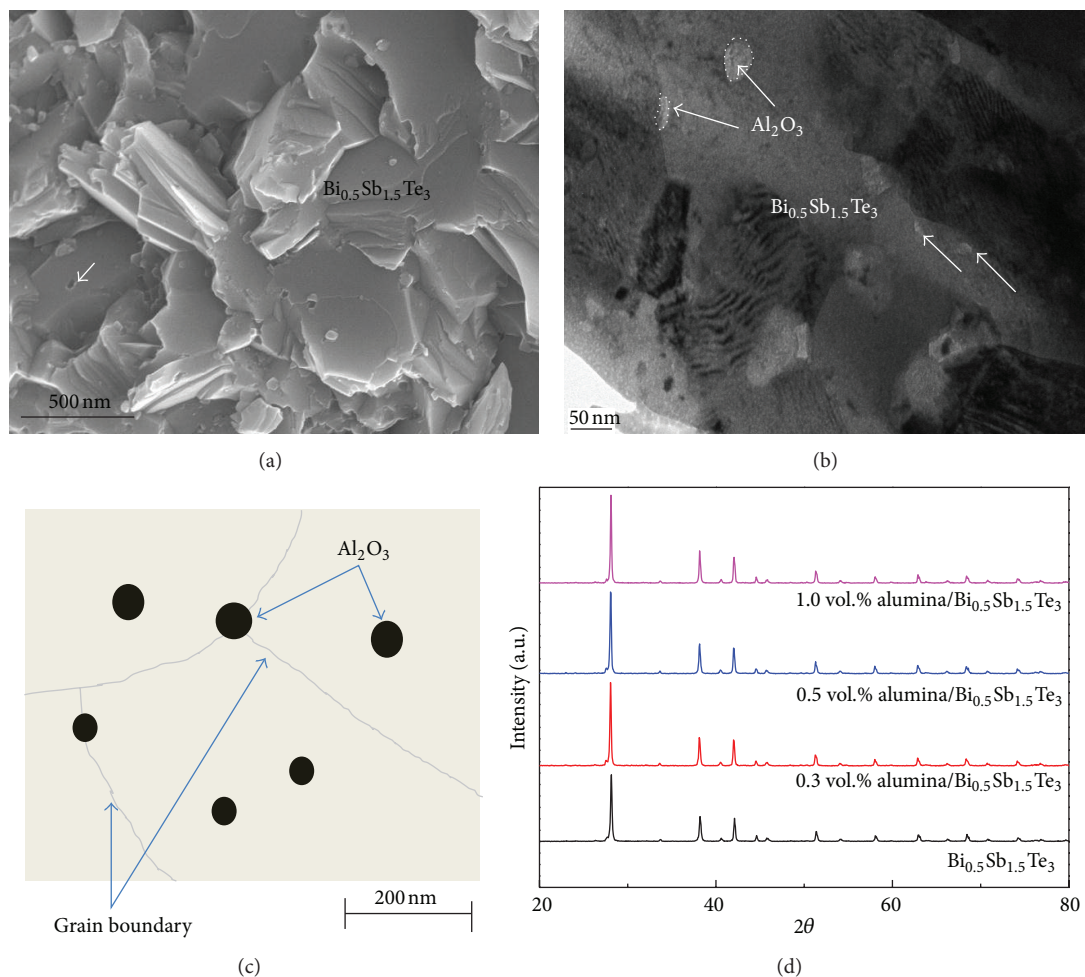


FIGURE 2: (a) FE-SEM image of fracture surface of the sintered $\text{Al}_2\text{O}_3/\text{BST}$ composite, (b) TEM image of $\text{Al}_2\text{O}_3/\text{BST}$ composite, (c) schematic illustration of the microstructure of the composite, and (d) XRD patterns of the composites compared with pure BST material.

mixed by ball milling process, and the milled powders were subsequently dried and calcinated into complex oxide materials. Finally, the calcinated powders were reduced to Bi-Sb-Te-based TE powders (for more detailed experimental procedures, refer to [11]). The synthesized $\text{Bi}_{0.5}\text{Sb}_{1.5}\text{Te}_3$ powders were mixed with Al_2O_3 nanoparticles by a high-energy ball milling process (Planetary Milling Machine, Fritsch) in a hexane solvent. The $\text{Al}_2\text{O}_3/\text{BST}$ composite powders were consolidated by a spark plasma sintering process (SPS, Weltech Co., WL-15-400, Republic of Korea) at 350°C for 10 min [12]. The phase of the powders and consolidated bulk was characterized by the X-ray diffraction method (model no. X'pert MPD 3040 with $\text{CuK}\alpha$ radiation). The microstructures of the powders and bulk composites were analyzed by field emission scanning electron microscopy (FESEM). Embedding of Al_2O_3 nanoparticles in BST matrix powders was characterized by a high-resolution transmission electron microscopy (HR-TEM, FE-TEM, 200 kV JEM2100F, JEOL). The weigh percent of the Al_2O_3 was found to be 0.014 wt%, corresponding to a 0.3 vol.% $\text{Al}_2\text{O}_3/\text{Bi}_{0.5}\text{Sb}_{1.5}\text{Te}_3$ composite when a density of 3.96 g/cc of the Al_2O_3 and a density of 6.88 g/cc of $\text{Bi}_{0.5}\text{Sb}_{1.5}\text{Te}_3$ were applied. The thermoelectric

properties of the sintered body were characterized using ZEM-3 (Ulvac-Rico), and the relative density was evaluated by Archimedes method. Thermal conductivity of the BST and $\text{Al}_2\text{O}_3/\text{BST}$ composites was calculated by the thermal diffusivity measured by the laser flash method (LFA457, Netzsch) and the specific heat measured by a differential scanning calorimeter (DSC) and the density of the sintered body.

3. Results and Discussion

Figure 1(a) shows the surface morphology of dried alumina nanoparticles used in this study. The size of primary nanoparticles is ranging from 10 to 20 nm and the primary nanoparticles are agglomerated into a few hundreds nm in diameters. The shape of the agglomerated nanoparticles is spherical due to reducing the surface energy. Figure 1(b) shows the size distribution of the nanoparticles solved in water solution. When the concentration of Al_2O_3 nanoparticles is 50 wt%, the size of nanoparticles exhibits a few micrometers in average size because of the agglomeration among them. As the concentration is reduced into 3 wt%, the size of about 10~20 nm

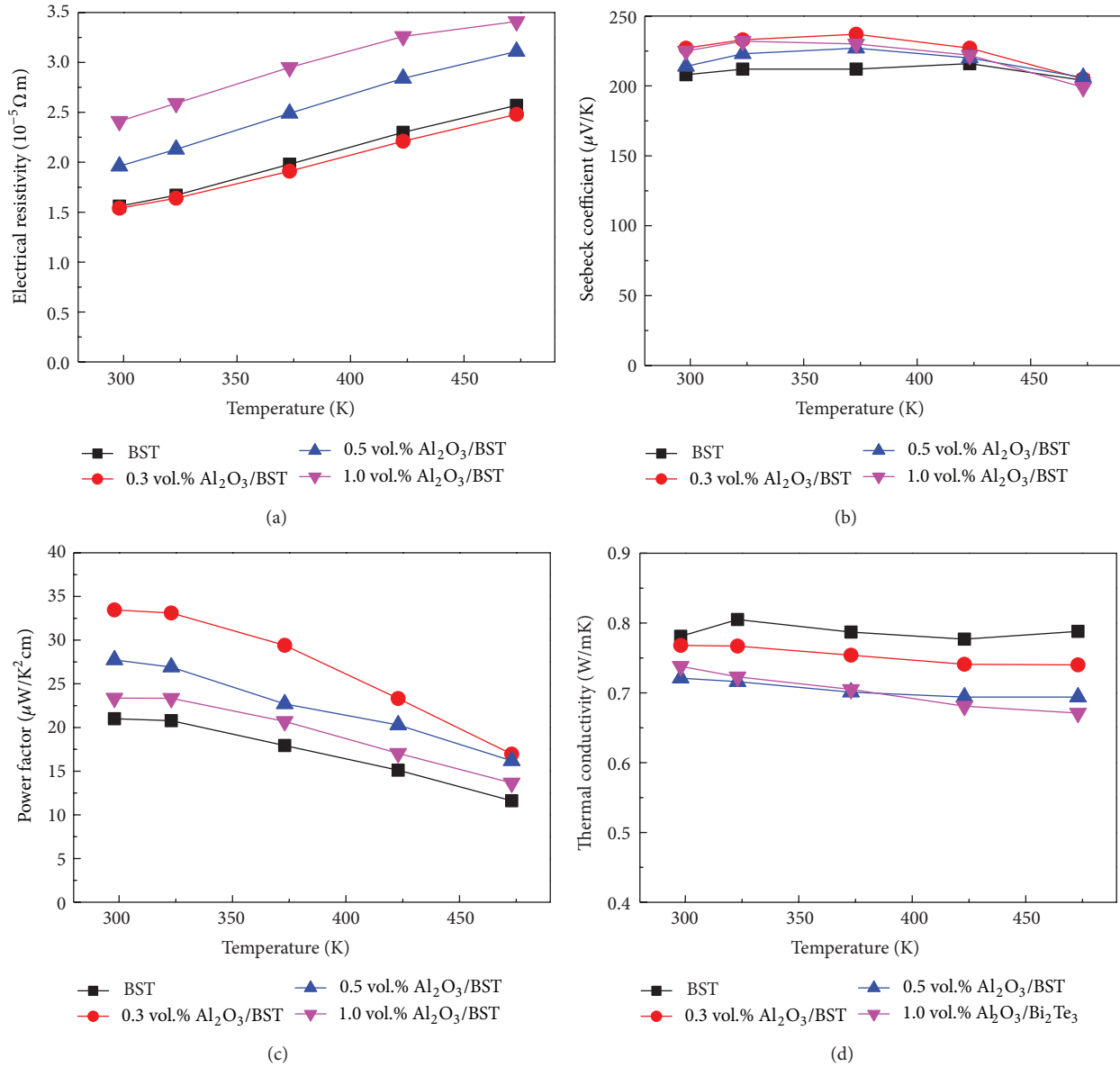


FIGURE 3: Variation of (a) electrical resistivity, (b) Seebeck coefficient, (c) power factor, and (d) thermal conductivity as a function of temperature ranging from 293 K to 473 K.

is revealed in the solvent. Thus, the alumina nanoparticles 3 wt% solution were used for homogeneous mixing with p-type powders. Figure 1(c) shows the morphology of Bi-Sb-Te-based powders prepared from the mechanochemical process (MCP) of the byproducts obtained from the Cu refining process. The BST powders show 100 nm of averaged size and it was found that XRD patterns of the fabricated powders are corresponded to Bi_{0.5}Sb_{1.5}Te₃ phase of JCPDS card no. 49-1713. The FE-SEM image shown in Figure 1(e) exhibits the morphology of Al₂O₃/BST composite powders prepared after ball milling process. The high-resolution TEM image of the composite powders reveals that alumina nanoparticles are embedded or dispersed in the Bi_{0.5}Sb_{1.5}Te₃ matrix powders.

Figure 2(a) shows the fracture surface of the Al₂O₃/BST composite consolidated by SPS process. The SPS provides fast densification time not to agglomerate Al₂O₃/nanoparticles

during the consolidation, even though hot pressing method also gives high density of p-type bismuth telluride powders. Typical brittle fracture of bismuth telluride-based materials is observed and some closed pores are partly revealed on the surface. A TEM image of Figure 2(b) exhibits grain boundaries of BST matrix and dispersed Al₂O₃ nanoparticles which shows bright region as indicated by the arrows. From the microstructure, it was analyzed that the distribution of Al₂O₃ nanoparticles are divided as intragrain type and intergrain type, respectively, as schematically illustrated in Figure 2(c). We expect that this microstructure provides a big benefit reducing total thermal conductivity because of the newly formed extrinsic Al₂O₃/BST interfaces besides the BST grain boundaries. Figure 2(d) shows the variation of XRD patterns of 0.3, 0.5, and 1.0 vol.% Al₂O₃/BST composites compared with pure BST materials. All XRD patterns have

TABLE 1: Comparison of electrical resistivity, carrier density, carrier mobility, and Seebeck coefficient of all samples measured by Hall-effect measurement at room temperature.

Sample	Electrical resistivity (m Ω ·cm)	Carrier density (#/cm ³)	Carrier mobility (cm ² /Vs)	Seebeck coefficient (μ V/K)
BST	1.52	1.81×10^{19}	297	205
0.3 vol.% Al ₂ O ₃ /BST	1.50	1.32×10^{19}	280	225
0.5 vol.% Al ₂ O ₃ /BST	1.94	1.57×10^{19}	226	210
1.0 vol.% Al ₂ O ₃ /BST	2.46	1.45×10^{19}	195	225

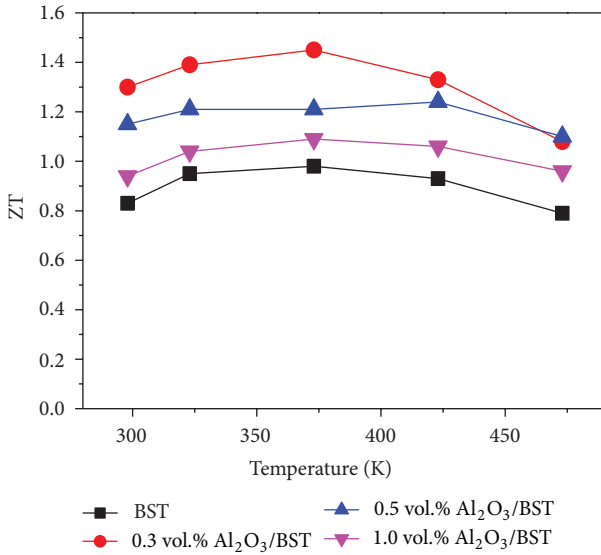


FIGURE 4: Comparison of dimensionless figures-of-merit (ZT) of pure BST and Al₂O₃/BST composites.

no big difference nonetheless contents of Al₂O₃ nanoparticles increase. This implies that the addition of alumina nanoparticles do not affect the phase of BST matrix.

Figure 3 shows thermoelectric properties of pure BST and Al₂O₃/BST composites characterized at the temperature ranging from 293 to 473 K. Figure 3(a) shows the electrical resistivities as a function of temperature. The measured electrical resistivity shows an increasing behavior by increasing temperature. The electrical resistivity of 1.0 vol.% Al₂O₃/BST composite increases from 1.5 to $2.5 \times 10^{-5} \Omega$ m when compared at 293 K and this tendency is still continuously remained by 473 K. Electrical resistivity of Al₂O₃/BST composite is increased as volume fraction of nonconductive Al₂O₃ materials increases. However, 0.3 vol.% Al₂O₃/BST composite shows similar electrical resistivity values with pure BST materials. This behavior means that addition of 0.3 vol.% Al₂O₃ nanoparticles does not affect the carrier transporting behaviors of pure BST. As shown in Table 1, carrier mobility of 0.3 vol.% Al₂O₃/BST composite does not change compared to pure BST.

The measured Seebeck coefficients of all samples show clearly positive values. These mean that the fabricated samples have p-type semiconducting behaviors. Seebeck coefficients of pure BST vary about 205–210 μ V/K as a function of temperature. The maximum Seebeck coefficient, 235 μ V/K, is obtained from the 0.3 vol.% Al₂O₃/BST composite at 373 K.

As shown in Table 1, carrier density of 0.3 vol.% Al₂O₃/BST composite shows the lowest value compared to other samples. It can be considered that the lower Fermi energy level caused by decreasing carrier density results in an increased Seebeck coefficient [13]. Furthermore, the results of Hall effect measurement in Table 1 also show that once Al₂O₃ nanoparticles below 10 nm in diameter are well dispersed under critical volume fraction in the matrix, they affect to carrier mobility and Seebeck coefficient.

Figure 3(c) shows the power factors calculated from the electrical properties. The power factor values of all samples are decreasing with increasing the temperature. However, all power factors of the composites are higher than that of pure BST due to the increased Seebeck coefficients. The peak power factor, 33 μ W/K² cm, was also obtained from the 0.3 vol.% Al₂O₃/BST composite at 293 K. This value is 1.7 times higher than 22 μ W/K² cm of pure BST materials. Although the difference between power factors is reduced as temperature increases, the tendency is continuously remained by 473 K. Figure 3(d) displays variation of thermal conductivity of the composites compared with pure BST materials as a function of temperature. The measured thermal conductivity of BST is about 0.8 W/mK and the values are decreased by the addition of alumina nanoparticles. As the volume fraction of alumina nanoparticles increases from 0.3 to 1.0 vol.%, total thermal conductivity is decreased down to 0.7 W/mK. It is considered that many interfaces generated from Al₂O₃ nanoparticles dispersed in the BST matrix result in the reduction of total thermal conductivity. The result implies that a reduction of the total thermal conductivity in the composites may originate from the newly formed 0.3 vol.% Al₂O₃/BST interfaces, which cause carrier and lattice phonon dissipation, as reported previously by the authors in an alumina nanoparticles/Bi₂Te₃ system [14].

Figure 4 shows the dimensionless figures-of-merit (ZT) of pure BST and the Al₂O₃/BST composites calculated from the thermoelectric properties displayed in Figure 3. The ZT of the composites shows higher values than those of pure BST as a function of temperature ranging from room temperature to 474 K. Furthermore, the maximum ZT value, 1.5, has been obtained from the 0.3 vol.% Al₂O₃/BST composite at 373 K due to significantly increased powder factors.

4. Summary

In summary, p-type BST nanopowders prepared from MCP were mixed with 0.3, 0.5, and 1.0 vol.% Al₂O₃ nanoparticles by a high-energy ball milling process. The fabricated

$\text{Al}_2\text{O}_3/\text{BST}$ composite powders show clear $\text{Bi}_{0.5}\text{Sb}_{1.5}\text{Te}_3$ phase as designed. It was found that the thermoelectric properties of the sintered $\text{Al}_2\text{O}_3/\text{BST}$ composite were significantly changed by the contents of alumina nanoparticles. The maximum ZT, 1.5, was obtained from the 0.3 vol.% $\text{Al}_2\text{O}_3/\text{BST}$ composite that exhibited high power factor and reduced thermal conductivity. These results clarify that the volume fraction of dispersion agents should be considered for the optimization of electrical and thermal transport behaviors in thermoelectric materials.

Acknowledgments

This work was supported by the principal R&D Program of the Korea Institute of Materials Science, Republic of Korea and Kyung Tae Kim appreciates the support by the Basic Science Research Program through the National Research Foundation of Korea (NRF) funded by the Ministry of Education, Science and Technology (Grant no. 2013R1A1A2010377).

References

- [1] R. J. Mehta, Y. Zhang, C. Karthik et al., "A new class of doped nanobulk high-figure-of-merit thermoelectrics by scalable bottom-up assembly," *Nature Materials*, vol. 11, no. 3, pp. 233–240, 2012.
- [2] X. B. Zhao, X. H. Ji, Y. H. Zhang, T. J. Zhu, J. P. Tu, and X. B. Zhang, "Bismuth telluride nanotubes and the effects on the thermoelectric properties of nanotube-containing nanocomposites," *Applied Physics Letters*, vol. 86, Article ID 062111, 2005.
- [3] Y. Q. Cao, X. B. Zhao, T. J. Zhu, X. B. Zhang, and J. P. Tu, "Syntheses and thermoelectric properties of $\text{Bi}_2\text{Te}_3\text{Sb}_2\text{Te}_3$ bulk nanocomposites with laminated nanostructure," *Applied Physics Letters*, vol. 92, Article ID 143106, 2008.
- [4] W. Xie, X. Tang, Y. Yan, Q. Zhang, and T. M. Tritt, "Unique nanostructures and enhanced thermoelectric performance of melt-spun BiSbTe alloys," *Applied Physics Letters*, vol. 94, Article ID 102111, 2009.
- [5] B. Poudel, Q. Hao, Y. Ma et al., "High-thermoelectric performance of nanostructured bismuth antimony telluride bulk alloys," *Science*, vol. 320, no. 5876, pp. 634–638, 2008.
- [6] L.-D. Zhao, B.-P. Zhang, J.-F. Li, M. Zhou, W.-S. Liu, and J. Liu, "Thermoelectric and mechanical properties of nano-SiC-dispersed Bi_2Te_3 fabricated by mechanical alloying and spark plasma sintering," *Journal of Alloys and Compounds*, vol. 455, no. 1–2, pp. 259–264, 2008.
- [7] S. Fan, J. Zhao, Q. Yan, J. Ma, and H. H. Hng, "Influence of nanoinclusions on thermoelectric properties of n-type Bi_2Te_3 nanocomposites," *Journal of Electronic Materials*, vol. 40, no. 5, pp. 1018–1023, 2011.
- [8] G.-D. Zhan, J. D. Kuntz, A. K. Mukherjee, P. Zhu, and K. Koumoto, "Thermoelectric properties of carbon nanotube/ceramic nanocomposites," *Scripta Materialia*, vol. 54, no. 1, pp. 77–82, 2006.
- [9] K. T. Kim, S. Y. Choi, E. H. Shin et al., "The influence of CNTs on the thermoelectric properties of a $\text{CNT}/\text{Bi}_2\text{Te}_3$ composite," *Carbon*, vol. 52, pp. 541–549, 2013.
- [10] Y. Zhang, X. L. Wang, W. K. Yeoh, R. K. Zeng, and C. Zhang, "Electrical and thermoelectric properties of single-wall carbon nanotube doped Bi_2Te_3 ," *Applied Physics Letters*, vol. 101, Article ID 031909, 2012.
- [11] K. T. Kim, K. J. Kim, and G. H. Ha, "Thermoelectric properties of P-type bismuth telluride powders synthesized by a mechanochemical process," *Electronic Materials Letters*, vol. 6, no. 4, pp. 177–180, 2010.
- [12] X. A. Fan, J. Y. Yang, R. G. Chen, W. Zhu, and S. Q. Bao, "Phase transformation and thermoelectric properties of p-type $(\text{Bi}_2\text{Te}_3)_{0.25}(\text{Sb}_2\text{Te}_3)_{0.75}$ prepared by mechanical alloying and hot pressing," *Materials Science and Engineering A*, vol. 438–440, pp. 190–193, 2006.
- [13] K. T. Kim, T. S. Lim, and G. H. Ha, "Improvement in thermoelectric properties of N-type bismuth telluride nanopowders by hydrogen reduction treatment," *Reviews on Advanced Materials Science*, vol. 28, no. 2, pp. 196–199, 2011.
- [14] K. T. Kim, H. Y. Koo, G. G. Lee, and G. H. Ha, "Synthesis of alumina nanoparticle-embedded-bismuth telluride matrix thermoelectric composite powders," *Materials Letters*, vol. 82, pp. 141–144, 2012.

Research Article

Formation of Dense Pore Structure by Te Addition in $\text{Bi}_{0.5}\text{Sb}_{1.5}\text{Te}_3$: An Approach to Minimize Lattice Thermal Conductivity

Syed Waqar Hasan,¹ Hyeona Mun,¹ Sang Il Kim,² Jung Young Cho,² Jong Wook Roh,² Sangsun Yang,³ Soon-Mok Choi,⁴ Kyu Hyoung Lee,² and Sung Wng Kim^{1,5}

¹ Department of Energy Science, Sungkyunkwan University, Suwon, Gyeonggi 440-746, Republic of Korea

² Materials R&D Center, Samsung Advanced Institute of Technology, Samsung Electronics, Yongin, Gyeonggi 446-712, Republic of Korea

³ Powder Technology Department, Powder and Ceramics Division, Korea Institute of Materials Science, Changwon, Gyeongnam 642-831, Republic of Korea

⁴ School of Energy, Materials and Chemical Engineering, Korea University of Technology and Education, Cheonan, Chungnam 330-708, Republic of Korea

⁵ Centre for Integrated Nanostructure Physics, Institute of Basic Science (IBS), Daejeon 305-701, Republic of Korea

Correspondence should be addressed to Kyu Hyoung Lee; kyuhyoung.lee@samsung.com and Sung Wng Kim; kimsungwng@skku.edu

Received 14 June 2013; Accepted 20 September 2013

Academic Editor: Won-Seon Seo

Copyright © 2013 Syed Waqar Hasan et al. This is an open access article distributed under the Creative Commons Attribution License, which permits unrestricted use, distribution, and reproduction in any medium, provided the original work is properly cited.

We herein report the electronic and thermal transport properties of p-type $\text{Bi}_{0.5}\text{Sb}_{1.5}\text{Te}_3$ polycrystalline bulks with dense pore structure. Dense pore structure was fabricated by vaporization of residual Te during the pressureless annealing of spark plasma sintered bulks of Te coated $\text{Bi}_{0.5}\text{Sb}_{1.5}\text{Te}_3$ powders. The lattice thermal conductivity was effectively reduced to the value of $0.35 \text{ W m}^{-1} \text{ K}^{-1}$ at 300 K mainly due to the phonon scattering by pores, while the power factor was not significantly affected. An enhanced ZT of 1.24 at 300 K was obtained in spark plasma sintered and annealed bulks of 3 wt.% Te coated $\text{Bi}_{0.5}\text{Sb}_{1.5}\text{Te}_3$ by these synergetic effects.

1. Introduction

Since 1950s, Bi-Te-based thermoelectric (TE) materials have been intensively investigated in order to realize highly efficient power generation from low-grade heat ($<250^\circ\text{C}$) or solid-state cooling and heating system. However, current applications are restricted to small scale systems such as climate control seat mainly due to their low TE performance. TE conversion efficiency is defined in terms of a dimensionless figure of merit, $ZT = \sigma S^2 T / \kappa_{\text{tot}}$, where σ is the electrical conductivity, S is the Seebeck coefficient, and κ_{tot} is the total thermal conductivity at a given absolute temperature (T). Because ZT value is controlled by electronic (σ and S) and thermal transport properties (κ), we can obtain the

enhanced ZT by following two approaches. The first approach is to reduce the lattice contribution (κ_{lat}) of κ_{tot} by promoting phonon scattering while maintaining the electronic transport properties. The other approach is breaking the tradeoff between σ and S through the density of states (DOS) engineering near at Fermi level.

Recently, nanostructuring has shown to be one of the most effective ways to reduce the κ_{lat} of Bi_2Te_3 -based TE materials. Many works of the literature have confirmed that enhanced phonon scattering at the interfaces can effectively reduce the κ_{lat} without a significant reduction of σ [1–6]. There are two main approaches to prepare Bi_2Te_3 -based nanostructured bulks. The first is the fabrication of nanograined structure to obtain the high density of the grain

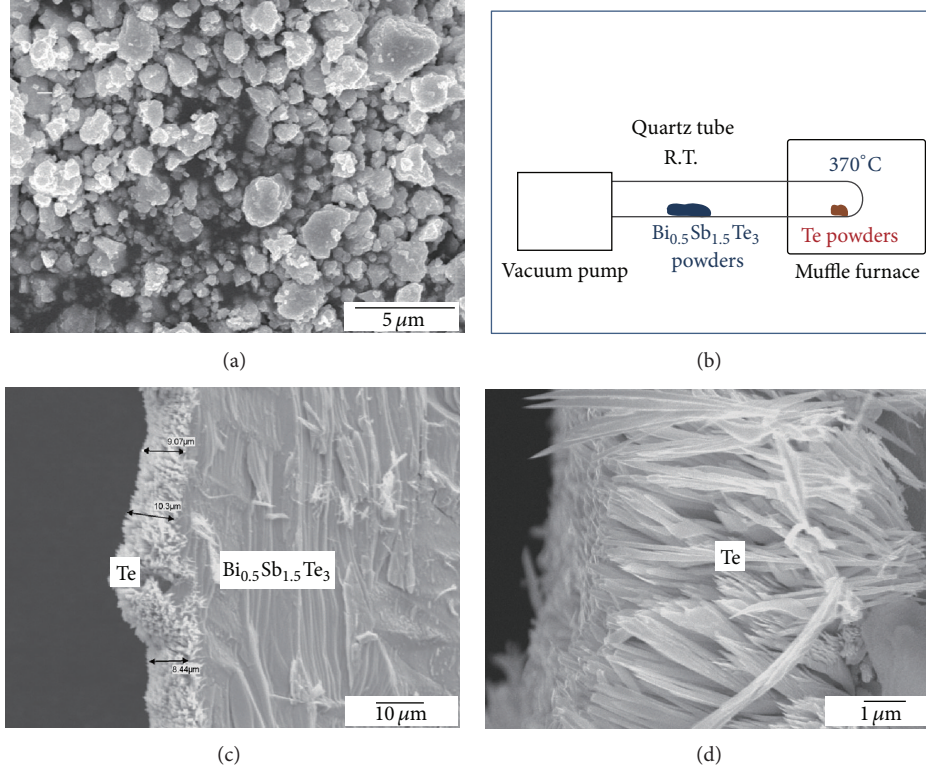


FIGURE 1: (a) The SEM image of $\text{Bi}_{0.5}\text{Sb}_{1.5}\text{Te}_3$ powders, (b) schematic illustration of evaporation process, and (c, d) SEM images of Te coated $\text{Bi}_{0.5}\text{Sb}_{1.5}\text{Te}_3$ by evaporation method.

boundaries to scatter phonons. By formation of nanograined structure, a further reduction of κ_{lat} becomes possible by intensified mid- and long-wavelength phonon scattering. There have been many experimental reports on nanograined structure Bi_2Te_3 -based TE materials with enhanced ZT values [1, 2]. For example, nanograined structure fabricated by high-energy ball milling combined with hot pressing raises the maximum ZT value of p-type $\text{Bi}_{0.5}\text{Sb}_{1.5}\text{Te}_3$ polycrystalline bulk up to 1.4 at 373 K from 1.0 at 300 K for its crystal ingot [1]. The second is the formation of nanoinclusion composite. Phase boundaries between TE material matrix and introduced nanoinclusions can act as effective phonon scattering centers; however, nanoinclusions through this approach limit ZT enhancement up to $\sim 20\%$ so far mainly due to the difficulty of controlling the size and distribution of nanoinclusions [7–9].

Here we report on the newly developed nanostructuring approach for formation of pore structure in Bi-Te-based TE materials. We investigated the relation between the pore structure and TE transport properties. The origin of the enhanced ZT could be elucidated from the viewpoint of the carrier filtering effect in addition to the phonon scattering in the presence of densely formed pore structure.

2. Experimental

$\text{Bi}_{0.5}\text{Sb}_{1.5}\text{Te}_3$ ingots were prepared by conventional solid-state reaction of high-purity elemental Bi, Sb, and Te (>99.99%, 5N Plus). Bi, Sb, and Te granules were weighed with

a stoichiometric ratio of the elements and sealed in an evacuated fused silica tube 12 mm in diameter. The tube was heated to 1073 K in a box furnace for 10 h and then quenched in water. The sample was ball-milled in N_2 -filled stainless steel vessel for 10 min using a high-energy mill (8000D, SPEX, USA). Ground $\text{Bi}_{0.5}\text{Sb}_{1.5}\text{Te}_3$ powders show a wide grain size distribution ranging from a few nanometers to tens of microns as shown in Figure 1(a). Then, Te coated $\text{Bi}_{0.5}\text{Sb}_{1.5}\text{Te}_3$ powders were fabricated by evaporation method. Figure 1(b) illustrates a schematic diagram of evaporation process. Firstly, Te powders (2, 6, 10, 20, 40, 60, and 80 wt.% of $\text{Bi}_{0.5}\text{Sb}_{1.5}\text{Te}_3$ powders) were placed at the end zone of quartz tube and $\text{Bi}_{0.5}\text{Sb}_{1.5}\text{Te}_3$ powders were loaded into the center part of quartz tube. The dead end part of quartz tube (Te powders) was placed in the muffle furnace with the open end of quartz tube connected with the vacuum pump, and then the furnace was heated to 370 °C for 1–6 h, while the zone for $\text{Bi}_{0.5}\text{Sb}_{1.5}\text{Te}_3$ powders keeps maintaining at room temperature.

The Te coated $\text{Bi}_{0.5}\text{Sb}_{1.5}\text{Te}_3$ powders were consolidated in a spark plasma sinter (SPS) using graphite die (diameter = 10.5 mm) in dynamic vacuum under an applied uniaxial pressure of 50 MPa at 753 K for 3 min. Then, the consolidated samples were annealed at 640 K for 20 h by the same evaporation method in order to remove the residual Te. The phases of Te coated $\text{Bi}_{0.5}\text{Sb}_{1.5}\text{Te}_3$ powders were analyzed by powder X-ray diffraction experiments using an X-ray diffractometer equipped with Cu $K\alpha$ radiation ($\lambda = 1.5418 \text{ \AA}$). Seebeck coefficient and electrical conductivity measurements from 300 K to 450 K were performed using an ULVAC ZEM-3

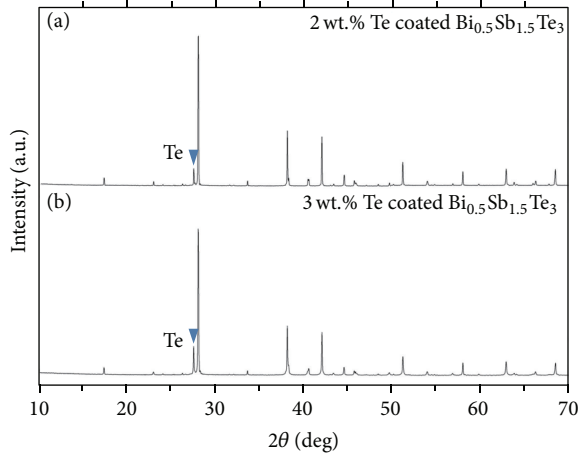


FIGURE 2: Powder X-ray diffraction patterns of Te loaded $\text{Bi}_{0.5}\text{Sb}_{1.5}\text{Te}_3$ by evaporation method. This clearly shows that the stoichiometric composition of $\text{Bi}_{0.5}\text{Sb}_{1.5}\text{Te}_3$ is not changed by the present Te evaporation method.

system. The κ values ($\kappa = \rho_s C_p \lambda$) were calculated from measurements taken separately: sample density (ρ_s), heat capacity (C_p), and thermal diffusivity (λ) measured under vacuum by laser-flash method (TC-9000, ULVAC, Japan), in which C_p was used as a constant value of $0.186 \text{ J g}^{-1} \text{ K}^{-1}$.

3. Results and Discussion

In order to fabricate the pore structure in Bi_2Te_3 -based TE materials, we introduced the Te metal element with high vapor pressure (723 K) onto the surface of $\text{Bi}_{0.5}\text{Sb}_{1.5}\text{Te}_3$ powders using evaporation method. Te layer with 8–11 μm thickness was coated onto the surface of $\text{Bi}_{0.5}\text{Sb}_{1.5}\text{Te}_3$ powders (Figure 1(c)). The Te contents of final Te coated $\text{Bi}_{0.5}\text{Sb}_{1.5}\text{Te}_3$ powders did not show significant change with the weight of Te loading (2–80 wt.%) for evaporation and were ranging from 1 to 3 wt.% of $\text{Bi}_{0.5}\text{Sb}_{1.5}\text{Te}_3$ powders. This might be related to the nanowire-like growth of Te with restricted length and diameter as shown in Figure 1(d). The growth mechanism of Te nanowires will be published elsewhere. The powder X-ray diffraction (XRD) patterns of $\text{Bi}_{0.5}\text{Sb}_{1.5}\text{Te}_3$ and 3 wt.% Te coated $\text{Bi}_{0.5}\text{Sb}_{1.5}\text{Te}_3$ powders are shown in Figure 2. All patterns are indexable to the Bi_2Te_3 as a major phase and small amount of Te was also noticed. Peaks for other phases were not detected in all compositions. From the microstructure and XRD pattern, we concluded that Te coated $\text{Bi}_{0.5}\text{Sb}_{1.5}\text{Te}_3$ powders could be successfully prepared by the present evaporation route.

The relative densities of SPS compacted bulks of x wt.% Te coated $\text{Bi}_{0.5}\text{Sb}_{1.5}\text{Te}_3$ powders ($x\text{TeBST}$, ~95%) did not show significant change compared with SPS compacted bulks of $\text{Bi}_{0.5}\text{Sb}_{1.5}\text{Te}_3$ powders (BST, ~96%). However, both of σ and S values of 2TeBST and 3TeBST were lower than those of BST as shown in Figures 3(a) and 3(b). This result suggests that coated Te remained within the bulks and deteriorated the electronic transport properties due to its metallic characteristics. To remove the residual Te, TeBST

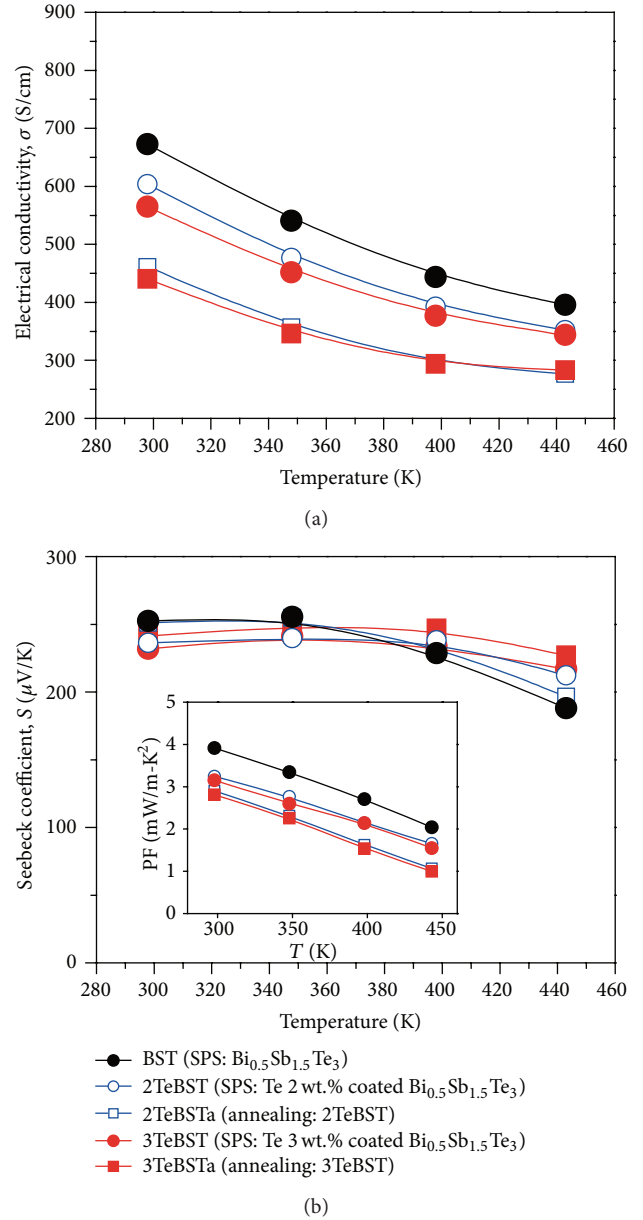


FIGURE 3: The temperature dependences of (a) electrical conductivity and (b) Seebeck coefficient for SPSed Te coated $\text{Bi}_{0.5}\text{Sb}_{1.5}\text{Te}_3$ samples and their annealed samples.

were annealed at 640 K for 20 h under vacuum. Figures 4(a) and 4(b) show the SEM images of fractured surface for SPS compacted and vacuum-annealed 2 (2TeBSTa) and 3 wt.% Te coated $\text{Bi}_{0.5}\text{Sb}_{1.5}\text{Te}_3$ (3TeBSTa). These figures clearly show the formation of dense pore structure with a wide size distribution ranging from a few to hundreds of nanometers. The relative densities of TeBSTa bulks were reduced to the value of 88%, indicating that vaporization of Te during the annealing process generated the pore structure. The σ values of 2TeBSTa and 3TeBSTa were lower than those of BST (Figure 3(a)) because of their low densities, while the S values showed relatively small decrease around room temperature (Figure 3(b)). Thus, the power factors are not much degraded

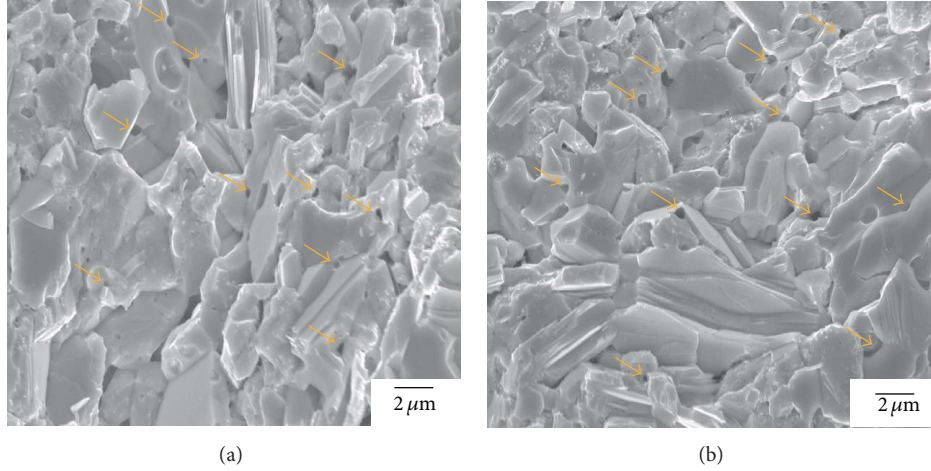


FIGURE 4: The scanning electron microscope (SEM) images of fractured surface for SPSed and vacuum-annealed (a) 2 and (b) 3 wt.% Te coated $\text{Bi}_{0.5}\text{Sb}_{1.5}\text{Te}_3$ samples.

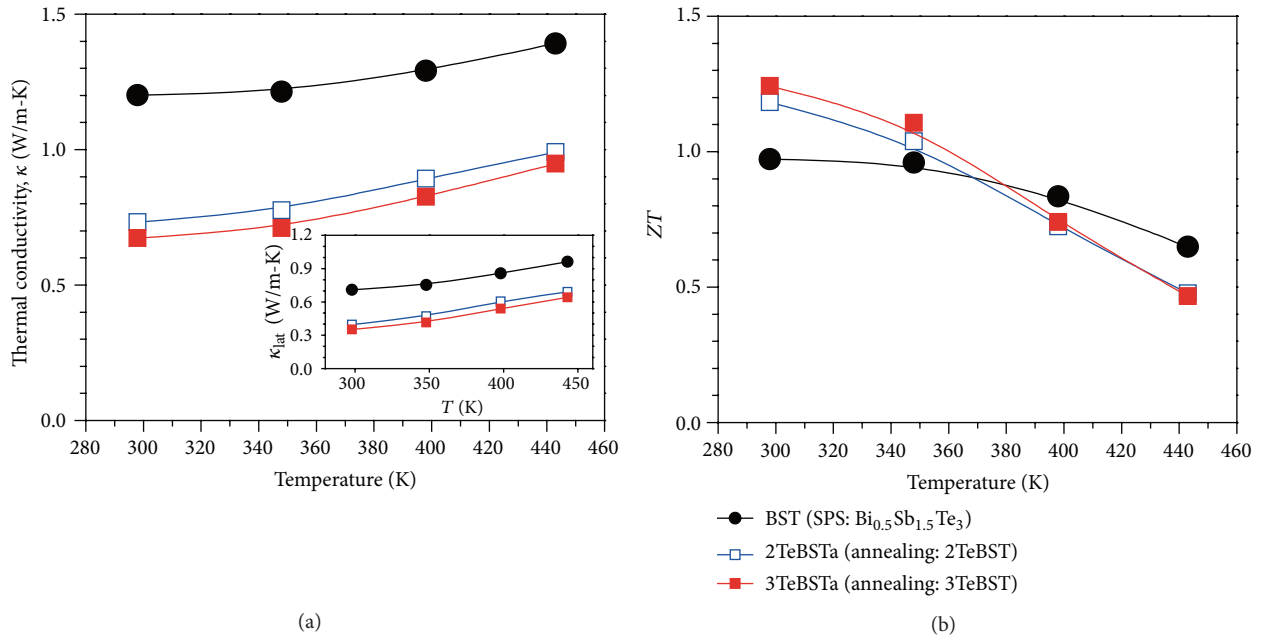


FIGURE 5: (a) The thermal conductivity and (b) dimensionless figure of merit, ZT for SPSed, and vacuum-annealed Te coated $\text{Bi}_{0.5}\text{Sb}_{1.5}\text{Te}_3$ samples.

(inset of Figure 3(b)). This might be considered to be related to the carrier filtering effect at the surface of pores. S is related to the energy derivative of the electronic density of state $n(E)$ and the relaxation time $\tau(E)$ through the Mott relation [10]. Thus S enhancement can be attained by a carrier filtering effect, a strong energy dependence of $\tau(E)$ caused by band bending at the surface of pores [11]. Experimental evidence of an enhancement of S has also been reported in Bi_2Te_3 -based materials [12].

We evaluated the temperature dependence of the κ_{tot} of 2TeBSTa and 3TeBSTa. The results are shown in Figure 5(a). Those of the BST are shown for comparison. Over the whole measured temperature range the value of κ_{tot} shows significant reduction compared to those of BST. In order to

clarify the phonon scattering effect by pores we calculated the κ_{tot} using the following equation (inset of Figure 5): $\kappa_{\text{lat}} = \kappa_{\text{tot}} - \kappa_{\text{ele}}$, where the electronic contribution (κ_{ele}) is estimated from the Wiedemann-Franz law, $\kappa_{\text{ele}} = L_0 \sigma T$, with the Lorentz number $L_0 = 2 \times 10^{-8} \text{ W } \Omega^{-1} \text{ K}^{-2}$. Extremely low values of κ_{lat} ranging from 0.35 to 0.39 $\text{W m}^{-1} \text{ K}^{-1}$ at 300 K were obtained in both the 2TeBSTa and 3TeBSTa. In comparison with the value of reference BST ($\kappa_{\text{lat}} \sim 0.71 \text{ W m}^{-1} \text{ K}^{-1}$ at 300 K), κ_{lat} decreased by about 50%, indicating stronger phonon scattering in the presence of densely formed pore structure.

Figure 5(b) presents the ZT s for 2TeBSTa and 3TeBSTa as a function of temperature. A high ZT above 1.24 at 300 K was realized in 3TeBSTa, and this high ZT value should

be originated from its low κ_{lat} value. By formation of pore structure without significantly affecting the charge carriers, this concept is an effective way to improve the TE performance by scattering phonons in addition to enhancement in S by carrier filtering effect. Nevertheless, a novel processing technique for the generation of nanosize pores with <50 nm diameter is highly needed to realize the maximum ZT by nanostructuring approach-based nanosized pore. Combined technique of nanosized powders fabrication for increasing the Te coating surface and controlled evaporation for forming the nanoscaled Te layer will give the possibility of further improvement of TE performance.

4. Conclusions

We successfully fabricated the dense pore structure in $\text{Bi}_{0.5}\text{Sb}_{1.5}\text{Te}_3$ -based TE materials by evaporation method of Te metal elements. The TE transport properties were investigated in the viewpoint of the pore structure. The characteristic TE properties are summarized as follows.

- (1) The thermal conductivity was largely reduced due to the significant phonon scattering by nanosized pores, leading to the extremely low lattice thermal conductivity of $0.35 \text{ W m}^{-1} \text{ K}^{-1}$ at 300 K.
- (2) The electronic transport properties were not much affected due to the enhancement of Seebeck coefficient, which is presumably attributed to the carrier filtering effect originated from nanosized pores.
- (3) The dense pore structured $\text{Bi}_{0.5}\text{Sb}_{1.5}\text{Te}_3$ TE materials show the enhanced dimensionless figure of merit, ZT of 1.24 at 300 K.

Acknowledgments

This research was supported by the Institute for Basic Science (IBS) in Korea and by the Human Resources Development Program (no. 20124010203270) of the Korea Institute of Energy Technology Evaluation and Planning (KETEP) grant funded by the Korean Government's Ministry of Trade, Industry and Energy.

References

- [1] B. Poudel, Q. Hao, Y. Ma et al., "High-thermoelectric performance of nanostructured bismuth antimony telluride bulk alloys," *Science*, vol. 320, no. 5876, pp. 634–638, 2008.
- [2] W. Xie, J. He, H. J. Kang et al., "Identifying the specific nanostructures responsible for the high thermoelectric performance of $(\text{Bi,Sb})_2\text{Te}_3$ nanocomposites," *Nano Letters*, vol. 10, no. 9, pp. 3283–3289, 2010.
- [3] R. J. Mehta, Y. Zhang, C. Karthik et al., "A new class of doped nanobulk high-figure-of-merit thermoelectrics by scalable bottom-up assembly," *Nature Materials*, vol. 11, no. 3, pp. 233–240, 2012.
- [4] J. S. Son, M. K. Choi, M. Han et al., "N-type nanostructured thermoelectric materials prepared from chemically synthesized ultrathin Bi_2Te_3 nanoplates," *Nano Letters*, vol. 12, no. 2, pp. 640–647, 2012.
- [5] A. Soni, Z. Yanyuan, Y. Ligen, M. K. K. Aik, M. S. Dresselhaus, and Q. Xiong, "Enhanced thermoelectric properties of solution grown $\text{Bi}_2\text{Te}_{3-x}\text{Se}_x$ nanoplatelet composites," *Nano Letters*, vol. 12, no. 3, pp. 1203–1209, 2012.
- [6] Y. Min, J. W. Roh, H. Yang et al., "Surfactant-free scalable synthesis of Bi_2Te_3 and Bi_2Se_3 nanoflakes and enhanced thermoelectric properties of their nanocomposites," *Advanced Materials*, vol. 25, no. 10, pp. 1425–1429, 2013.
- [7] M. Popov, S. Buga, P. Vysikaylo et al., " C_{60} -doping of nanostructured Bi-Sb-Te thermoelectrics," *Physica Status Solidi A*, vol. 208, no. 12, pp. 2783–2789, 2011.
- [8] M. Y. Kim, B. K. Yu, and T. S. Oh, "Thermoelectric characteristics of the p-type $(\text{Bi}_{0.2}\text{Sb}_{0.8})_2\text{Te}_3$ nanocomposites processed with SbTe nanowire dispersion," *Electronic Material Letters*, vol. 8, no. 3, pp. 269–273, 2012.
- [9] V. D. Blank, S. G. Buga, V. A. Kulbachinskii et al., "Thermoelectric properties of $\text{Bi}_{0.5}\text{Sb}_{1.5}\text{Te}_3/\text{C}_{60}$ nanocomposites," *Physical Review B*, vol. 86, no. 7, Article ID 075426, 2012.
- [10] M. Cutler and N. F. Mott, "Observation of anderson localization in an electron gas," *Physical Review*, vol. 181, no. 3, pp. 1336–1340, 1969.
- [11] M. Ohtaki and K. Araki, "Thermoelectric properties and thermopower enhancement of Al-doped ZnO with nanosized pore structure," *Journal of the Ceramic Society of Japan*, vol. 119, no. 1395, pp. 813–816, 2011.
- [12] S. I. Kim, S. Hwang, J. W. Roh et al., "Experimental evidence of enhancement of thermoelectric properties in tellurium nanoparticle-embedded bismuth antimony telluride," *Journal of Materials Research*, vol. 27, no. 19, pp. 2449–2456, 2012.

Research Article

Effect of Mechanical Deformation on Thermoelectric Properties of p-Type $(\text{Bi}_{0.225}\text{Sb}_{0.775})_2\text{Te}_3$ Alloys

Sung-Jin Jung,^{1,2} Seong Keun Kim,¹ Hyung-Ho Park,² Dow-Bin Hyun,¹
Seung-Hyub Baek,^{1,3} and Jin-Sang Kim¹

¹ Future Convergence Research division, Korea Institute of Science and Technology, Seoul 136-791, Republic of Korea

² Department of Material Engineering, Yonsei University, Seoul 120-749, Republic of Korea

³ Department of Nanomaterials Science and Technology, University of Science and Technology, Daejeon 305-333, Republic of Korea

Correspondence should be addressed to Seung-Hyub Baek; shbaek77@kist.re.kr and Jin-Sang Kim; jskim@kist.re.kr

Received 13 June 2013; Revised 11 September 2013; Accepted 13 September 2013

Academic Editor: Chan Park

Copyright © 2013 Sung-Jin Jung et al. This is an open access article distributed under the Creative Commons Attribution License, which permits unrestricted use, distribution, and reproduction in any medium, provided the original work is properly cited.

The effect of mechanical deformation and annealing on thermoelectric properties of p-type $(\text{Bi}_{0.225}\text{Sb}_{0.775})_2\text{Te}_3$ was performed. The ingots were prepared by melting, followed by quenching method using source materials with compositions of $(\text{Bi}_{0.225}\text{Sb}_{0.775})_2\text{Te}_3$. Rectangular shaped specimens ($5 \times 5 \times 12 \text{ mm}^3$) were cut from ingots and then cold-pressed at 700 MPa for 2 to 20 times by changing the press direction perpendicular to previous one. The cold-pressed samples have been annealed in a quartz ampoule at 573 K. The grain size of the samples was controlled by the number of cold-pressing process and annealing time. Fine grain structure with a grain size of not more than $10 \mu\text{m}$ is obtained in highly deformed samples. The Seebeck coefficient of the deformed samples were gradually increased with annealing and converged to the similar value of about $225 \mu\text{V/K}$ after 30 hrs. The small grain size in highly deformed sample enables a rapid increase of Seebeck coefficient with annealing time (~ 2 hrs.), indicating that the thermal energy needed to recrystallize in highly deformed specimens is lower than that in low deformed specimens. Z values are rapidly increased with annealing time especially in highly deformed alloys, and converge to about $3.0 \times 10^{-3}/\text{K}$ at room temperature. A higher thermoelectric performance could be expected by the optimization of composition and microstructural adjustment. The present study experimentally demonstrates a simple and cost-effective method for fabricating Bi-Te-based alloys with higher thermoelectric performance.

1. Introduction

Bi_2Te_3 -related compounds such as solid solutions of Bi_2Te_3 and Sb_2Te_3 have been widely studied over the past decades due to their excellent properties for use in thermoelectric cooling and power generation near the room temperature [1–3]. Currently, one stream of thermoelectric researches follows the improving thermoelectric dimensionless Figure-of-Merit ($ZT = \alpha^2 \sigma T / \kappa$, where α , σ , κ , and T are the Seebeck coefficient, electrical conductivity, thermal conductivity, and absolute temperature) by fabricating nanostructures with existing thermoelectric (TE) materials [4–6]. Thermoelectric nanostructures can be produced by many techniques, such as hydrothermal methods [7], wet chemical reactions [8], and ball milling [2, 4]. Conventional ball milling has been

employed to produce large quantities of fine particles with a size of one to several microns and this process can be readily scaled up for commercial use at reasonable cost. In order to obtain TE materials, the TE particles should be consolidated into a dense solid using various methods, such as spark plasma sintering [5, 9], hot-pressing [2, 4, 7, 10], and extrusion methods [11, 12].

Generally cold-pressing only mechanically compacts the particles and thus the density of cold-pressed composites tend to be low, resulting in a material with poor mechanical and thermoelectric properties. To improve the mechanical and electrical properties of the composites, the cold-pressing should be followed by sintering at appropriated temperatures. Thus, the techniques used to produce TE nanocomposites can be any combination of a powder preparation method

and a composited consolidation methods. As a powder preparation method, high energy ball milling is generally used with source materials of crystalline Bi-Sb-Te alloy ingots which are prepared by zone melting and Bridgman methods [5, 9, 11, 13].

In this paper, we introduce a simple fabrication method of randomly oriented polycrystalline Bi-Sb-Te based alloys which is not employing conventional powdering process. $(\text{Bi}_{0.225}\text{Sb}_{0.775})_2\text{Te}_3$ compound was prepared by melting the source elements followed by serial processing with cold-pressing process and recovery annealing. The effects of degree of deformation and annealing time on the thermoelectric properties were investigated. Thermoelectric properties are discussed on the point of view of microstructural evolution of cold-pressed sample with annealing.

2. Experimental Procedures

Elemental bismuth (Bi), antimony (Sb), and tellurium (Te), with purity of 99.99% were used as starting materials for synthesis of $(\text{Bi}_{0.225}\text{Sb}_{0.775})_2\text{Te}_3$ compounds. Each of three materials was weighed according to the chemical formula of $(\text{Bi}_{0.225}\text{Sb}_{0.775})_2\text{Te}_3$, loaded into quartz ampoules, and sealed under a vacuum of 10^{-6} Torr. Before loading the mixture, the quartz ampoule, whose inner diameter was 11 mm, was chemically etched with 10% HF + 90% HNO_3 and then washed with deionized water to remove any surface impurities. Bi, Sb, and Te were melted and rocked at 1023 K for 4 hrs and then rapidly cooled to room temperature. The cylindrical ingots were then cut into bar-shaped specimen ($5 \times 5 \times 12 \text{ mm}^3$) for the measurement of thermoelectric properties and cold-pressing. Cold-pressing was performed by applying the mechanical pressure of 700 MPa using tool-steel die. The press direction was perpendicular to the $5 \text{ mm} \times 5 \text{ mm}$ plane of the specimen. After the first pressing step, the specimen was removed from the press die and pressed again with the press direction perpendicular to newly formed $5 \text{ mm} \times 5 \text{ mm}$ face of deformed specimen. These cold-press steps were carried out for 2 to 20 times to change the amount of mechanical deformation and then annealed at 573 K up to 30 hrs.

X-ray diffraction patterns of quenched ingot, compacted pallets after pressing and annealing process were obtained using a BRUKER D8 diffractometer. Specimen density was calculated from precise measurements of the specimen's dimension and mass. The electrical resistivity (ρ) was measured by the conventional AC four-probe method. The Seebeck coefficient was measured by a method based on the slope of a voltage versus temperature-difference curve. The thermoelectric properties of the same samples were also measured by using commercial equipment (ZEM-2M, Ulvac Inc.) and two sets of measurements are within $\pm 1\%$ of each other. Microstructural analysis was carried out using a scanning electron microscope (Hitachi S-4300) equipped with an Electron Back-Scatter Diffraction (EBSD, Bruker e-Flash) system. The Figure-of-Merit (Z) was determined by the Harman method in vacuum chamber (10^{-5} Torr). Four Pt-wires with $40 \mu\text{m}$ in diameter were bonded to both ends

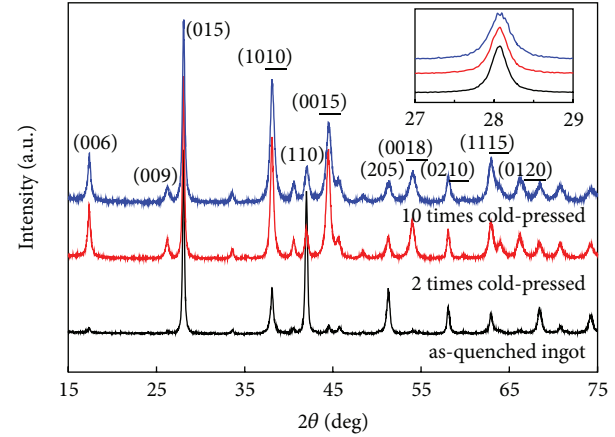


FIGURE 1: X-ray diffraction patterns of as-quenched ingot and $(\text{Bi}_{0.225}\text{Sb}_{0.775})_2\text{Te}_3$ alloys with different number of cold pressing.

of rectangular-shaped sample, two for current flow and the other two for voltage measurement.

3. Results and Discussion

Figure 1 shows the X-ray diffraction patterns of the as-quenched $(\text{Bi}_{0.225}\text{Sb}_{0.775})_2\text{Te}_3$ ingot and cold-pressed pallets on the surface perpendicular to the press direction. The peak intensities were normalized by (015) diffraction peaks of the samples. All diffraction peaks were assigned to a rhombohedral $\text{Bi}_2\text{Te}_3\text{-Sb}_2\text{Te}_3$ structure. The presence of strong diffraction peaks in the cold-pressed samples such as (006), (009), (0015), and (0018) indicates the alignment of grains along the $[00\ell]$ direction, that is, reorientation of the ab planes of the grains took place during the repressing process even at room temperature. Inset of Figure 1 is magnified (015) diffraction peak. The more re-pressing process, the more broadened the peaks are in the patterns suggest that fine grain-sized particles are formed and/or complicated natures of the residual stress and strain remain in pallets.

Figure 2 shows the X-ray diffraction patterns of cold-pressed samples taken perpendicular to the direction of press with different annealing times. Solid dots in the figure are the positions of peak heights with standard intensities of powder patterns for rhombohedral $(\text{Bi}_{0.2}\text{Sb}_{0.8})_2\text{Te}_3$ phases (JCPDS number 72-1836). In 10 times cold-pressed and 30 hrs annealed sample, the peaks position and intensities exhibited almost the same as that of standard powder patterns, which indicates that the ab oriented grains which are aligned perpendicular to press direction in cold-pressed specimen were randomly rearranged by recrystallization during the annealing process. It was also noted that the diffraction peaks of the annealed samples were narrowed with the increase of annealing time (shown in the inset of Figures 2(a) and 2(b)), supporting that the grain growth took place during the heat treatment.

To obtain detailed information on the microstructures, especially the grain-boundary characteristics, Electron Back-Scatter Diffraction (EBSD) analysis according to the number

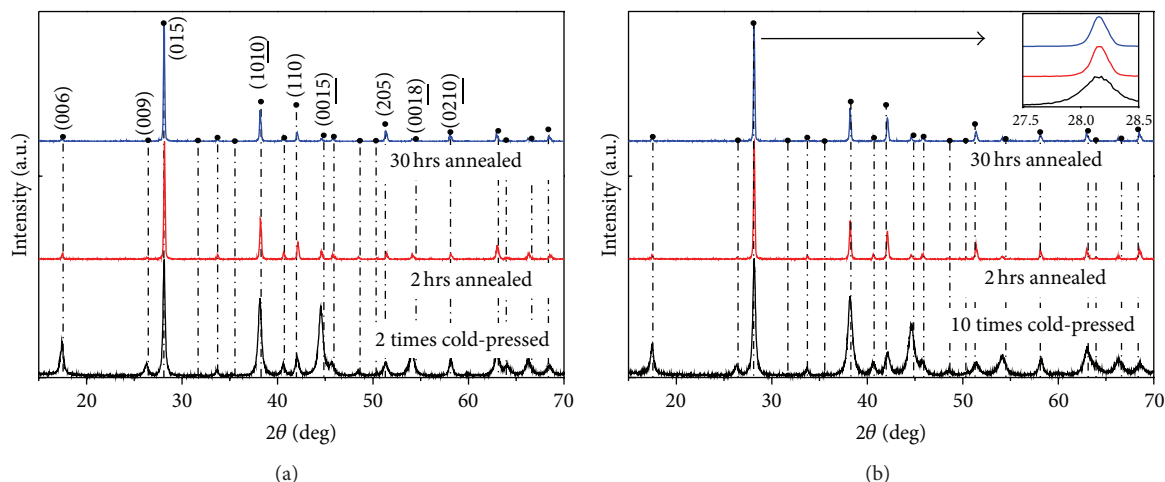


FIGURE 2: X-ray diffraction patterns of $(\text{Bi}_{0.225}\text{Sb}_{0.775})_2\text{Te}_3$ versus annealing time at 573 K for (a) 2 times cold-pressed, and (b) 10 times cold-pressed samples. Solid dots represent the position of peak heights from standard powder pattern (JCPDS # 72-1836). Inset in (b) indicates magnified (0015) diffraction peaks of the samples.

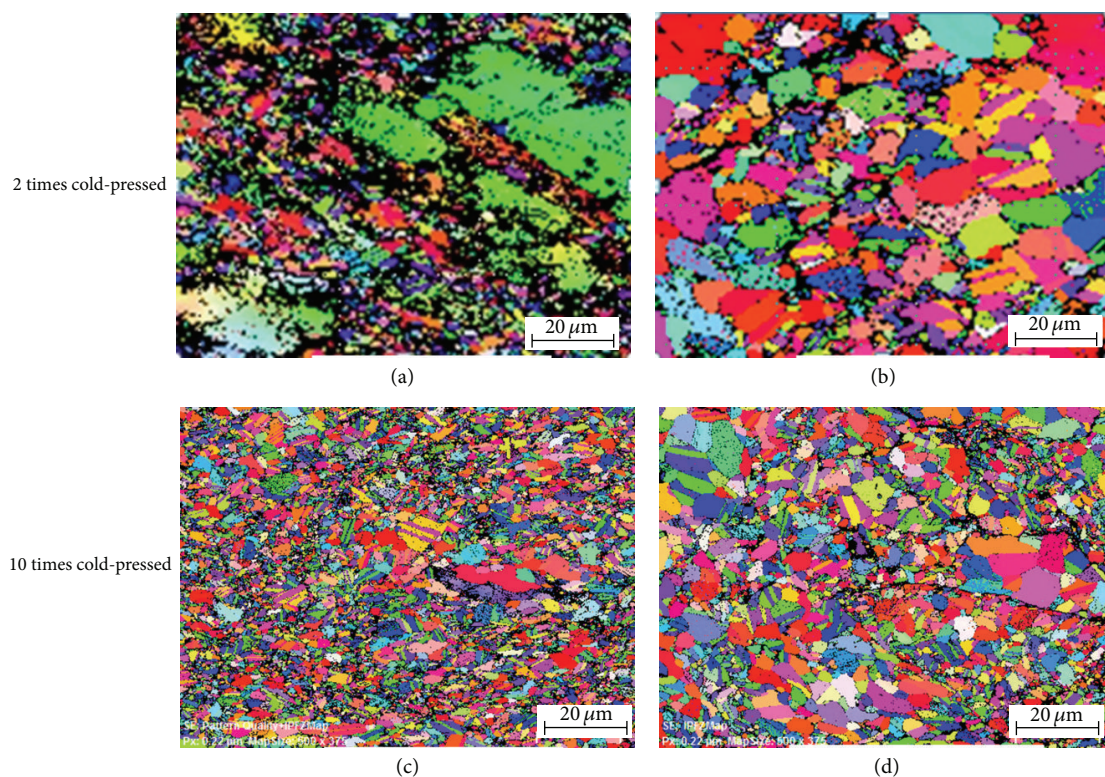


FIGURE 3: Electron Back-Scatter Diffraction (EBSD) images of $(\text{Bi}_{0.225}\text{Sb}_{0.775})_2\text{Te}_3$ alloys versus annealing time at 573 K with different number of cold-pressing. 2 times cold-pressed and annealed for (a) 2 hrs, (b) 30 hrs, 10 times cold-pressed and annealed for (c) 2 hrs, and (d) 30 hrs.

of cold-pressing and annealing time was carried out. Figure 3 illustrates an EBSD image of the samples which were cold-pressed 2 and 10 times followed by annealing for 2 and 30 hrs, respectively. It is clear that the more repetition of pressing process of the sample, the smaller the grain can be found. Dark areas in Figures 3(a) and 3(b) are due to the lattice distortions, such as dislocations and vacancies. The image

in Figure 3(a) exhibits unclear grain structure and further annealing leads to grain structure with the size of a few tens of micrometers (Figure 3(b)). The decrease of the dark areas especially inside the 2 times cold-pressed grains means the recovery happened during the annealing process. However, it is easily recognized from Figures 3(c) and 3(d) that the annealing led to dynamic recrystallization and significant

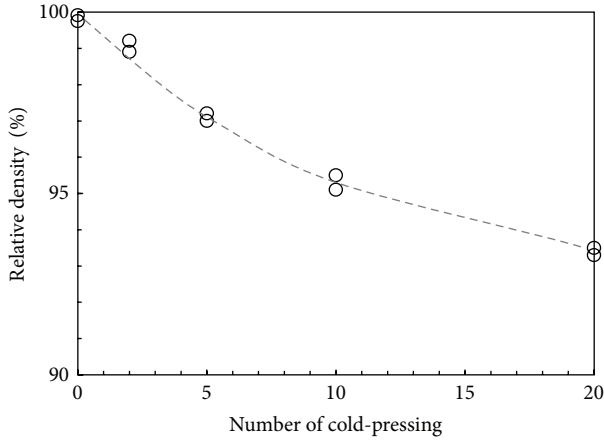


FIGURE 4: Change of relative density for $(\text{Bi}_{0.225}\text{Sb}_{0.775})_2\text{Te}_3$ alloys with the number of cold-pressing.

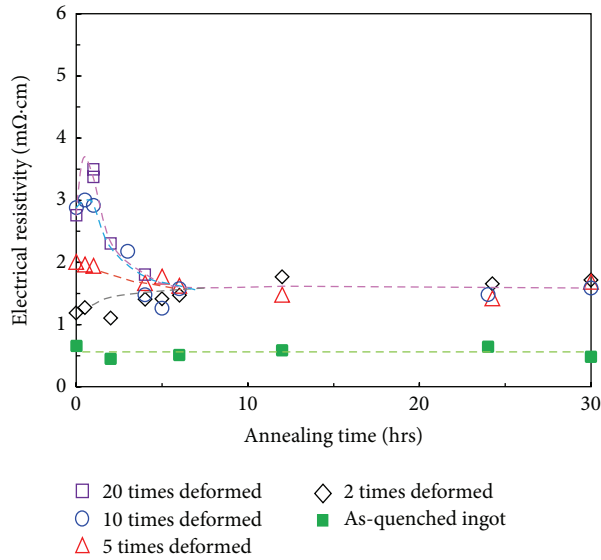


FIGURE 5: Change of the electrical resistivity of $(\text{Bi}_{0.225}\text{Sb}_{0.775})_2\text{Te}_3$ alloys with the number of cold-pressing and annealing time at 573 K.

increase of grain size for the 10 times cold-pressed samples. The change of the microstructure during annealing may cause changes in thermoelectric properties such as resistivity and Seebeck coefficient.

The relative density of the samples with the number of cold-pressing is shown in Figure 4, and the electrical resistivity with different annealing time is shown in Figure 5. Initially, a pronounced electrical resistivity increase is observed in the highly deformed samples. Heat treatment process produces a strong decrease of electrical resistivity especially for highly deformed sample and the values were saturated after 6 hrs of heat treatment. The relative density values were decreased with an increase of the number of cold-pressing process. The annealing of the specimen does not lead to densification in the whole observed region.

In general, when a metal is deformed below its recrystallization temperature, it is said to be “cold-worked.” All

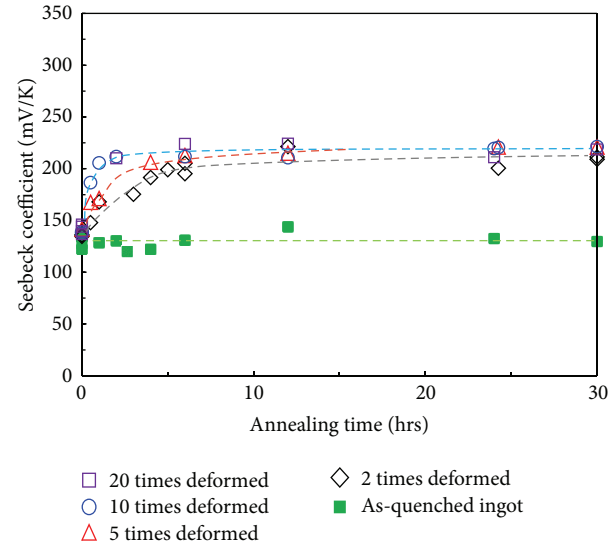


FIGURE 6: Change of the Seebeck coefficient of $(\text{Bi}_{0.225}\text{Sb}_{0.775})_2\text{Te}_3$ alloys with the number of cold-pressing and annealing time at 573 K.

the properties of a metal that are dependent on the lattice structure are affected by plastic deformation or cold-working [14, 15]. Cold-pressing process in this work produces very high deformation enough to fracture the ingot into fine particles. This is related to relatively low ductility and mechanical strength of the Bi-Te-based alloy compared to a metal and the presence of cleavage planes. The decrease of relative density in Figure 4 may be attributed to the increase of fine particles with cold-working since large grains have broken into smaller pieces and as they are smaller their porosity constantly increases.

The electrical resistivity in polycrystalline structures can depend on a grain size, porosity, carrier density, and its mobility [16, 17]. It is well known that the electrical resistivity is determined competitively by carrier concentration and mobility as described by the relationship: $\rho = 1/ne\mu$, where n , μ , and e are the carrier concentration, carrier mobility, and electron charge, respectively. The decrease of electrical resistivity with annealing time, especially in highly deformed samples (10 and 20 times cold-pressed samples in Figure 5, can be explained by an increased electrical mobility because of the grain growth during the annealing process. This would be associated with a decrease in total scattering of charge carriers and annihilation of deformed stress in the sample, leading to enhanced conductivity.

Figure 6 shows the Seebeck coefficient of cold-pressed samples as a function of annealing time. The positive values of Seebeck coefficient indicate that all the samples are p-type materials. All the as-deformed specimens showed the same Seebeck coefficient of about $140 \mu\text{V/K}$. However, these values were increased with increase of annealing time. Interestingly, the Seebeck coefficient of the samples cold-pressed 10 and 20 times repetition were sharply increased in relatively short annealing periods of about 2 hrs, and saturated to the value of

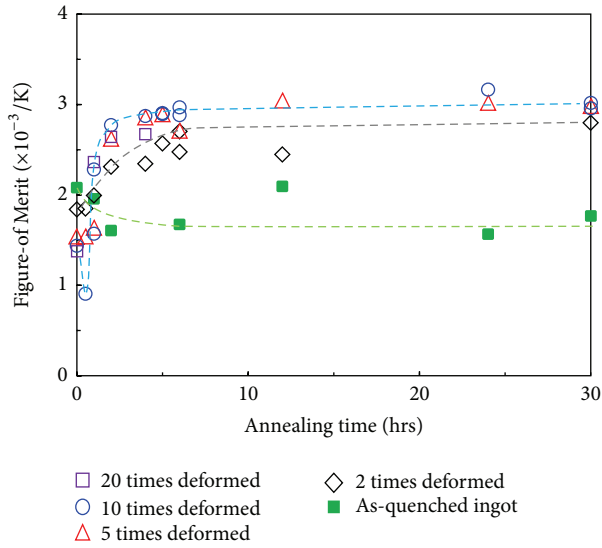


FIGURE 7: Change of the Figure-of-Merit of $(\text{Bi}_{0.225}\text{Sb}_{0.775})_2\text{Te}_3$ alloys with the number of cold-pressing and annealing time at 573 K.

about $220 \mu\text{V/K}$. The Seebeck coefficient of the samples cold-pressed 2 or 5 times repetition increased slowly compared to that of the samples cold-pressed 10 and 20 times.

It is well known that Seebeck coefficient is mostly governed by effective mass and carrier concentrations, and independent of the grain size. In highly deformed samples, it should be pointed out that large amount of dislocations, point defects, and antistructure defects may increase the electrical carriers with very low mobility, and these are responsible for high electrical resistivity. More detailed analysis on exact structure of generated defects according to cold-pressing and how these defects affect thermoelectric properties is beyond the scope of this paper. Accordingly, it is thought that the time needed for recrystallization of crushed particles in the cold-pressed Bi-Sb-Te compounds depend on the number of cold-pressing process. The enhancement of Seebeck coefficient with annealing can be considered by two aspects: the reduction of carrier concentration with annihilation of residual defects and recrystallization.

Room temperature Figure-of-Merit (Z) of the cold-pressed alloys as a function of annealing time are plotted in Figure 7, respectively. Z values are rapidly increased with annealing time especially in highly deformed alloy. The highest Figure-of-Merit of the sample reaches about $3.0 \times 10^{-3}/\text{K}$ at 300 K, which is lower than the zone-melted one and that of state-of-art Bi_2Te_3 - Sb_2Te_3 -based materials [2, 18]. The power factors of as-quenched ingot and 10 times deformed sample are plotted as the function of the annealing time in Figure 8. As shown in the figure, the power factors of annealed ingot exhibited similar values to those in deformed samples after annealing. Even though the low Seebeck values are in as-quenched ingot, the low resistivity of the ingot resulted in similar values for power factors with highly deformed samples after annealing. Thus, the improvement of Z value in a highly deformed sample is mainly attributed to

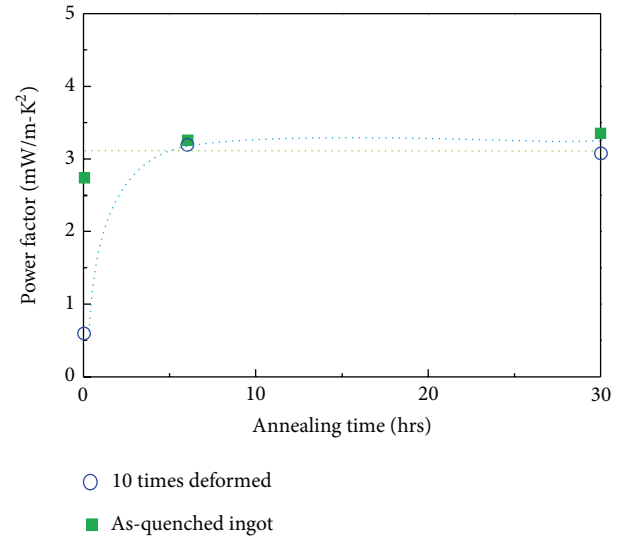


FIGURE 8: Change of the power factor of $(\text{Bi}_{0.225}\text{Sb}_{0.775})_2\text{Te}_3$ alloys of as-quenched ingot and the 10 times cold-pressing with annealing time at 573 K.

reduced thermal conductivity. During the annealing process, new grain structure with a submicron size is generated by the recrystallization and grain coarsening. Although the Z value is still low, the fabrication method of bulk Bi_2Te_3 -based compounds introduced here is more cost effective. It is also much easier compared to other powder-base fabrication techniques for bulk thermoelectric materials and it can be easily scaled up for commercial applications.

4. Conclusions

The effects of the repetition of cold-pressings followed by recovery annealing on the thermoelectric properties were investigated for $(\text{Bi}_{0.225}\text{Sb}_{0.775})_2\text{Te}_3$ alloys. Generally, the plastic deformation increases dislocation density and changes grain size distribution in single and polycrystalline materials. In this experiment, the mechanical pressure of 700 MPa is high enough to fracture the as-quenched ingot into fine particles. Thus, high density of dislocation as well as the reduction of grain size may be expected in our cold-pressed samples. The grain size of cold-pressed samples was controlled by the number of cold-press processing and annealing times. The high electrical resistivity in highly deformed samples is mainly attributed to the increase of grain boundary scattering due to the reduction of grain size and high porosity. The enhancement of the Seebeck coefficient with annealing is mainly related to the recovery and recrystallization of the deformed samples. The recrystallization process can be obtained by diffusion process or annihilation of generated defect. The time needed for recrystallization with annealing depend on the grain size and porosity; the smaller the grain size, the shorter the diffusion distances. The fast saturation of Seebeck coefficient in highly deformed samples with annealing indicates that the Seebeck coefficient is independent of the grain size. However, further decrease in electrical resistivity

was observed after Seebeck coefficient saturation. Increase in mobility could occur due to the grain growth which reduces the grain boundary scattering for electron transport.

It is worth mentioning that our cold-press processing does not employ any methods to prepare powder of the materials. Even we did not use powdering process; fine grained structure is obtained by simple repetition of cold-pressing followed by annealing. Accordingly, it seems reasonable to conclude that the improvement of thermoelectric performance in $(\text{Bi}_{0.225}\text{Sb}_{0.775})_2\text{Te}_3$ compound is possible by using cold-deformation and recovery annealing process. Investigations on optimization of composition and microstructural adjustment are required for further enhancement of ZT . Our approaches provide cost-effective fabrication method of Bi_2Te_3 -based alloys with high thermoelectric performance.

Conflict of Interests

The authors declare that there is no conflict of interests regarding the publication of this paper.

Acknowledgment

This research was supported by the Converging Research Center Program through the Ministry of Education, Science and Technology (2013K000168).

References

- [1] D. M. Rowe, *CRC Handbook of Thermoelectrics*, CRC, 1995.
- [2] B. Poudel, Q. Hao, Y. Ma et al., "High-thermoelectric performance of nanostructured bismuth antimony telluride bulk alloys," *Science*, vol. 320, no. 5876, pp. 634–638, 2008.
- [3] R. Venkatasubramanian, E. Siivola, T. Colpitts, and B. O'Quinn, "Thin-film thermoelectric devices with high room-temperature figures of merit," *Nature*, vol. 413, no. 6856, pp. 597–602, 2001.
- [4] Y. Ma, Q. Hao, B. Poudel et al., "Enhanced thermoelectric figure-of-merit in p-type nanostructured bismuth antimony tellurium alloys made from elemental chunks," *Nano Letters*, vol. 8, no. 8, pp. 2580–2584, 2008.
- [5] W. Xie, J. He, H. J. Kang et al., "Identifying the specific nanostructures responsible for the high thermoelectric performance of $(\text{Bi,Sb})_2\text{Te}_3$ nanocomposites," *Nano Letters*, vol. 10, no. 9, pp. 3283–3289, 2010.
- [6] G. Joshi, H. Lee, Y. Lan et al., "Enhanced thermoelectric figure-of-merit in nanostructured p-type silicon germanium bulk alloys," *Nano Letters*, vol. 8, no. 12, pp. 4670–4674, 2008.
- [7] Y. Q. Cao, X. B. Zhao, T. J. Zhu, X. B. Zhang, and J. P. Tu, "Syntheses and thermoelectric properties of Bi_2Te_3 , Sb_2Te_3 bulk nanocomposites with laminated nanostructure," *Applied Physics Letters*, vol. 92, no. 14, Article ID 143106, 2008.
- [8] Y. Zhao, J. S. Dyck, B. M. Hernandez, and C. Burda, "Enhancing thermoelectric performance of ternary nanocrystals through adjusting carrier concentration," *Journal of the American Chemical Society*, vol. 132, no. 14, pp. 4982–4983, 2010.
- [9] X. Tang, W. Xie, H. Li, W. Zhao, Q. Zhang, and M. Niino, "Preparation and thermoelectric transport properties of high-performance p-type Bi_2Te_3 with layered nanostructure," *Applied Physics Letters*, vol. 90, no. 1, Article ID 012102, 2007.
- [10] D.-B. Hyun, J.-S. Hwang, J.-D. Shim, and T. S. Oh, "Thermoelectric properties of $(\text{Bi}_{0.25}\text{Sb}_{0.75})_2\text{Te}_3$ alloys fabricated by hot-pressing method," *Journal of Materials Science*, vol. 36, no. 5, pp. 1285–1291, 2001.
- [11] S. Miura, Y. Sato, K. Fukuda, K. Nishimura, and K. Ikeda, "Texture and thermoelectric properties of hot-extruded Bi_2Te_3 compound," *Materials Science and Engineering A*, vol. 277, no. 1-2, pp. 244–249, 2000.
- [12] S. S. Kim, S. Yamamoto, and T. Aizawa, "Thermoelectric properties of anisotropy-controlled p-type Bi-Te-Sb system via bulk mechanical alloying and shear extrusion," *Journal of Alloys and Compounds*, vol. 375, no. 1-2, pp. 107–113, 2004.
- [13] J.] Jiang, L. Chen, S. Bai, Q. Yao, and Q. Wang, "Fabrication and thermoelectric performance of textured n-type $\text{Bi}_2(\text{Te, Se})_3$ by spark plasma sintering," *Materials Science and Engineering B*, vol. 117, no. 3, pp. 334–338, 2005.
- [14] C. S. Çetinarslan, "Effect of cold plastic deformation on electrical conductivity of various materials," *Materials and Design*, vol. 30, no. 3, pp. 671–673, 2009.
- [15] Z.-C. Chen, K. Suzuki, S. Miura, K. Nishimura, and K. Ikeda, "Microstructural features and deformation-induced lattice defects in hot-extruded Bi_2Te_3 thermoelectric compound," *Materials Science and Engineering A*, vol. 500, no. 1-2, pp. 70–78, 2009.
- [16] J. Jaklovszky, R. Ionescu, N. Nistor, and A. Chiculita, "Grain size effect on the figure of merit of sintered solid solutions based on Bi_2Te_3 ," *Physica Status Solidi*, vol. 27, no. 2, pp. 329–332, 1975.
- [17] A. Kumar, D. Singh, and D. Kaur, "Grain size effect on structural, electrical and mechanical properties of NiTi thin films deposited by magnetron co-sputtering," *Surface and Coatings Technology*, vol. 203, no. 12, pp. 1596–1603, 2009.
- [18] T. M. Tritt, "Holey and unholey semiconductors," *Science*, vol. 283, no. 5403, pp. 804–805, 1999.

Research Article

Thermoelectric Properties of Carbon Nanotube and Nanofiber Based Ethylene-Octene Copolymer Composites for Thermoelectric Devices

P. Slobodian,^{1,2} P. Riha,³ R. Olejnik,^{1,2} M. Kovar,^{1,4} and P. Svoboda^{2,4}

¹ Polymer Centre, Faculty of Technology, T. Bata University, T.G.M. 275, 762 72 Zlin, Czech Republic

² Centre of Polymer Systems, University Institute, T. Bata University, Nad Ovcirnou 3685, 760 01 Zlin, Czech Republic

³ Institute of Hydrodynamics, Academy of Sciences, Pod Patankou 5, 166 12 Prague 6, Czech Republic

⁴ Department of Polymer Engineering, Faculty of Technology, T. Bata University in Zlin, T.G.M. 275, 762 72 Zlin, Czech Republic

Correspondence should be addressed to P. Slobodian; slobodian@ft.utb.cz

Received 12 June 2013; Revised 30 August 2013; Accepted 31 August 2013

Academic Editor: Jung-Kun Lee

Copyright © 2013 P. Slobodian et al. This is an open access article distributed under the Creative Commons Attribution License, which permits unrestricted use, distribution, and reproduction in any medium, provided the original work is properly cited.

Polymer composites have been created from multiwalled carbon nanotubes or carbon nanofibers and ethylene-octene copolymer. The composites have thermoelectric properties and exhibit thermoelectric effect, that is, the conversion of temperature differences into electricity. The thermoelectric efficiency of created composites with nanotube or nanofiber concentration of 30 wt% evaluated by a thermoelectric power at room temperature is $13.3 \mu\text{V/K}$ and $14.2 \mu\text{V/K}$, respectively. The flexible thermoelectric device (thermopile) was constructed with three different composite legs to produce electric current and the output voltage was measured in the range of temperature difference from -15 to 25°C .

1. Introduction

Thermoelectric devices are capable to convert thermal energy into electricity when there is a different temperature between the hot and cold junctions of two dissimilar conductive or semiconductive materials. Thermoelectric electricity generation is based on a phenomenon called Seebeck effect. The heat supplied at the hot junction causes an electric current to flow that can be harnessed as useful voltage [1]. At the atomic scale, the temperature difference causes charge carriers in the material to diffuse from the hot side to the cold side.

The classical thermoelectric materials used in devices are metals and metallic alloys, for example, Al, Cu, Ni, Bi, Sb, chromel, and alumel as well as semiconductors PbTe and Bi₂Te₃. The common feature of these materials is not only high thermoelectric efficiency but also high cost of production, weight, and scarcity. Consequently, the alternative thermoelectric materials are investigated including organic polymers with carbon nanotube fillers [2–8]. Though the

thermoelectric efficiency of organic thermoelectrics is currently lower than that of the inorganic ones, their mechanical flexibility, processability, light weight, and low manufacturing costs may be desirable in applications.

The composites containing pristine or doped carbon nanotubes and polymers like polyvinylidene fluoride [2, 3], polyester [4], polyaniline [5], polyvinyl acetate [6, 7], and poly(3-hexylthiophene) [8] have shown great promise as n-type or p-type thermoelectrics. The thermoelectric figure of merit of the polymer composites is typically in the range 0.001–0.01 at room temperature. Though the thermoelectric efficiency is considerably lower than that of classical thermoelectric materials, the polymer thermoelectrics may be, in view of other properties, a desirable technological and environment-friendly alternative.

Traditional inorganic thermoelectric semiconductors have some limitations in their applications like low efficiency and high material cost of low-abundance materials [9] in addition to brittleness and difficulty in large-area deposition

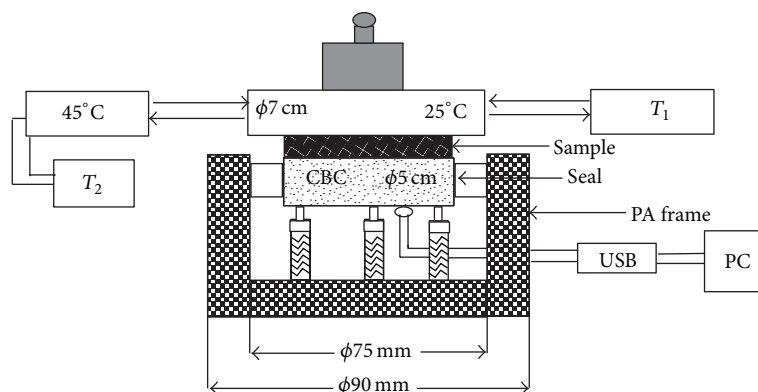


FIGURE 1: Experimental setup for the measurement of thermal conductivity of composites.

[10]. On the other hand novel organic semiconductors (molecules, oligomers, and polymers) possess some unique features. There can be mentioned their low density, low manufacturing cost, easy synthesis, and processing and versatile processability; they have low thermal conductivity, and they are flexible finally with natural abundance of environmentally friendly materials [11, 12]. They can be composed of net organic conducting polymers [11] or copolymers [13] even as a combination of polymer-inorganic materials [14] or as a polymeric nanocomposite mainly in course to further improve its thermoelectric efficiency. Metal nanoparticles [12] or different kinds of carbon nanotubes, CNT, as usually used as an electrically conductive filler used in either non-conducting polymeric matrix (PVAC) [7] or conductive polymer matrix [8, 15–17].

In the present paper, the effect of different carbon-base fillers in ethylene-octene copolymer composites on their thermoelectric power at room temperature 22°C was studied. The composites were prepared with pristine multiwalled carbon nanotubes (MWCNT) and carbon nanofibers (CNF). The thermoelectric efficiency of the composites was calculated on basis of the measured electrical and thermal conductivities and the induced electric voltage.

2. Experimental

The ethylene-octene copolymer (EOC) with 45 wt% of octene content (ENGAGE 8842) was purchased from Dow Chemicals. The density of EOC was 0.8595 g cm^{-3} .

The purified multiwalled carbon nanotubes (MWCNT) produced by acetylene chemical vapor deposition method were purchased from Sun Nanotech Co., Ltd., China with purity $>90\%$ and electrical resistivity $0.12\text{ }\Omega\text{cm}$. Further details on the nanotubes denoted further on MWCNT(Sun) were obtained by means of the transmission electron microscopy analysis presented in our previous papers [18, 19]. From the corresponding micrographs the diameter of individual nanotubes was determined to be between 10 and 60 nm, their length from tens of micrometers up to $3\text{ }\mu\text{m}$. The maximum aspect ratio of the nanotubes is about 300.

The other kind of MWCNTs produced by chemical vapor deposition and marked Baytubes C70 P was provided by

the Bayer MaterialScience AG, Germany (C-purity $>95\text{ wt}\%$, outer mean diameter $\sim 13\text{ nm}$, inner mean diameter $\sim 4\text{ nm}$, length $>1\text{ }\mu\text{m}$, and declared bulk density of MWCNT of agglomerates of micrometric size $45\text{--}95\text{ kg/m}^3$). The nanotubes are denoted further on MWCNT(Bayer).

The carbon nanofibers with trade name VGCF (Vapor Grown Carbon Fibers) were supplied by Showa Denko K.K. (Japan). The fiber diameter was 150 nm , length $10\text{ }\mu\text{m}$, and electrical resistivity $0.012\text{ }\Omega\text{cm}$.

The composites were prepared by ultrasonication of dispersions of MWCNT or CNF in EOC/toluene (5% solution of EOC in toluene). The chosen filler concentration in the composites was 30 wt% which is well above the percolation threshold. The sonication process was carried out using thermostatic ultrasonic bath (Bandelin electronic DT 103H) for 3 h at 80°C . Then the dispersion was poured into acetone which is not solvent of EOC but mixes with toluene and forms a precipitate. Finally, the composite sheets were prepared by compression molding at 100°C .

Morphology of the prepared composites was studied using scanning electron microscope (SEM). SEM analysis was carried out using Vega II LMU (Tescan, Czech Republic) with a beam acceleration voltage set at 10 kV .

The apparent electrical conductivity of composites, hereafter called simply electrical conductivity, was measured by a two-point method using Broadband Dielectric/Impedance Spectrometer (Novocontrol Technologies) in N_2 atmosphere across the composite sample thickness. Thickness of the sample was about 1.1 mm and the diameter 20 mm . The values of electrical DC conductivity were determined at frequency 0.1 Hz when the conductivity is constant.

The apparent thermal conductivity of the composites, hereafter called simply thermal conductivity, was measured using experimental setup shown schematically in Figure 1 according to the method described in [20, 21]. At the beginning of the measurement, the central brass cylinder (CBC) was annealed to a temperature 45°C using a hollow cylinder connected to a water thermostat. Then the hollow cylinder was removed and replaced by the composite sample (diameter 5 cm , thickness 2 mm) on top of which the hollow brass cylinder kept at 25°C is then placed and loaded to ensure good contact with the sample. The software LabVIEW

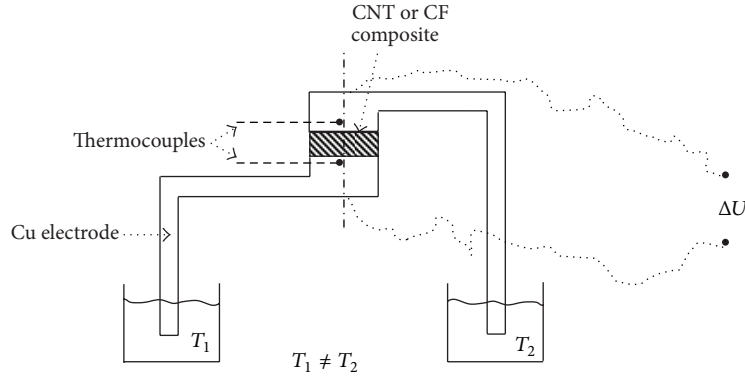


FIGURE 2: Schematics diagram of the setup for the measurement of electric voltage induced in the composite in response to a temperature difference.

SignalExpress 2.5 was used for the decreasing temperature acquisition from CBC. The mathematical analysis of the measured data and calculation of thermal conductivity is presented in detail in Section 3.

The thermoelectric power measurement was carried out for all the samples using a setup illustrated in Figure 2. The schematic diagram shows that the circular composite sample (diameter 20 mm, thickness 2 mm) is placed between two copper electrodes. The ends of each Cu electrode were immersed in a thermostatic silicone oil baths set to different temperatures. The temperature at the copper/composite interfaces was measured by a digital thermometer. The arising thermoelectric current is measured with a Keithley 2000 Digital Multimeter.

3. Calculation of Thermal Conductivity

To describe the temperature time dependence of the central brass cylinder (Figure 1), the following heat balance equation is used [21]:

$$-C \frac{dT}{dt} = \frac{s\lambda(T - T_2)}{h} + \psi(T - T_2), \quad (1)$$

where T denotes the temperature of the CBS, C the heat capacity of the CBC, t the time, s and h the sample area and thickness, respectively, λ the thermal conductivity of the sample, T_2 the temperature of hollow brass cylinder 25°C , and Ψ the coefficient accounting for a heat loss. The first term of (1) on the right side represents heat flow through the measured sample and the second one the heat loss to surroundings.

The left side of (1) represents heat output of the central brass cylinder form monitored by the temperature T from the initial temperature $T_1 = T(t = 0) = 45^\circ\text{C}$ to the equilibrium temperature $T_2 = 25^\circ\text{C}$. The solution of (1) is

$$T = T_1 - (T_1 - T_2) \exp[-(A_1 + A_2)t], \quad (2)$$

where A_1 and A_2 are coefficients, $A_1 = s\lambda/hC$, and $A_2 = \psi/C$.

The heat loss was determined by the so called “the blind experiment”. The heat loss was determined by the so called

“the blind experiment”. In this course the specimen with very small thermal conductivity (expanded polystyrene with $\lambda = 0.035 \text{ Wm}^{-1}\text{K}^{-1}$) is used as calibration standard. Equation (2) can be simplified to $y = y_0 + a \exp(-bt)$ for the nonlinear regression of the measured temperature decay of the CBS. From a nonlinear regression of “the blind experiment” the coefficient b follows equal to the heat loss coefficient $A_2 = 0.000368 \text{ s}^{-1}$. Thermal capacity of the central brass cylinder was determined $C = 94.107 \text{ JK}^{-1}$. The size of samples $h = 0.002 \text{ m}$ and $s = 0.001963 \text{ m}^2$.

To determine, for example, the thermal conductivity of CNF/EOC (30 wt%) composite, the coefficient b , obtained from the fitting of the time dependent temperature decrease of the central brass cylinder, is $b = 0.001211 \text{ s}^{-1}$. Consequently, $A_1 = b - A_2 = 0.001211 - 0.000368 = 0.0008422 \text{ s}^{-1}$, and the thermal conductivity of the composite,

$$\begin{aligned} \lambda &= \frac{A_1 h C}{s} \\ &= \frac{0.0008422 * 0.002 * 94.107}{0.001963} = 0.8081 \text{ Wm}^{-1}\text{K}^{-1}. \end{aligned} \quad (3)$$

4. Results

Figure 3 shows SEM analysis of the surface of multiwalled carbon nanotubes and carbon nanofibers networks, respectively. The networks were formed from the aqueous dispersion of MWCNTs or CNFs on the surface of the interdigitated electrode by a drop method. The obtained micrographs in Figure 3 show some differences, namely, the larger diameters of pores of CNF layer than the ones of the carbon nanotube layer. The cross-sections of the composites in Figure 4 show good dispersion of MWCNT(Sun) and CNF fillers.

The effect of the filler concentration on the electric (σ) and thermal conductivity (λ) of composites is presented in Figure 5. The figure demonstrates that both conductivities considerably increase with the filler concentration when a percolation threshold is reached. The results show that in the composite with longer CNFs (about $10 \mu\text{m}$), the conducting paths are created at lower concentration in comparison

TABLE 1: Thermoelectric properties of the composite samples. The electrical conductivity σ , the thermal conductivity λ , the thermoelectric power S , the power factor $S^2\sigma$, and the figure of merit ZT .

Sample	σ (S/m)	λ (W/mK)	S (μ V/K)	$S^2\sigma$ (μ W/mK ²)	ZT
CNF/EOC	0.21	0.8081	14.2	4.2×10^{-5}	1.5×10^{-2}
MWCNT(Sun)/EOC	0.13	0.4087	13.3	2.3×10^{-5}	1.6×10^{-2}
MWCNT(Bayer)/EOC	0.12	0.2859	6.4	4.9×10^{-6}	5.0×10^{-3}

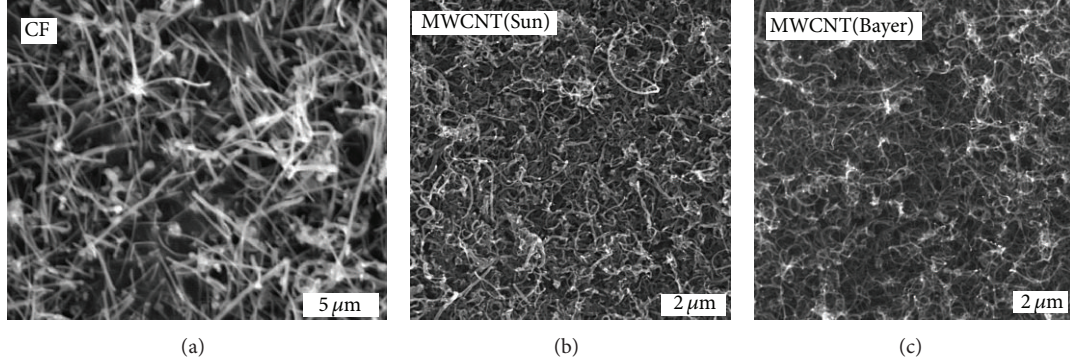


FIGURE 3: SEM micrographs of the layer surface made of three different materials: (a) carbon nanofibers, (b) MWCNT(Sun), and (c) MWCNT(Bayer).

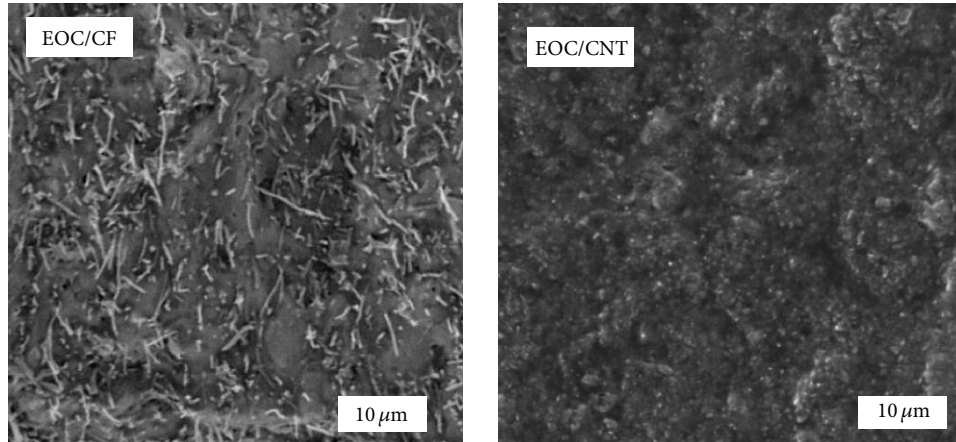


FIGURE 4: SEM micrographs of the cross-section of CNF/EOC and MWCNT(Sun)/EOC composites.

with EOC composite filled by MWCNT(Sun)s (length about 3 mm). The lower resistivity of CNFs (0.012 Ω cm) with respect to MWCNT resistivity (0.12 Ω cm) also probably contributes to the electrical conductivity difference between both composites. For the evaluation of the composite thermoelectric properties, the composites with the filler concentration 30%, what is well above the percolation threshold, were used. The values of conductivities for this filler concentration are summarized in Table 1 among other values of thermal properties.

Figure 6 shows the values of induced electric voltage in response to a temperature difference across the measured sample of all investigated composites. From the slope of the linear temperature-difference (ΔT) dependence of resulting electric voltage V_{TEV} , the thermoelectric power S , which is defined $S = V_{TEV}/\Delta T$, can be obtained. The thermoelectric

power is comparable for CNF and MWCNT(Sun) composites (Table 1). On the other hand, the electrical conductivities differentiate the values of power factor ($S^2\sigma$) of CNF and MWCNT(Sun) composites in the dimensionless figure of merit ZT ($ZT = (S^2\sigma/\lambda) T$, where T is temperature). The power factor is important value since it is directly related to the usable power attainable from the thermoelectric material [2]. The factor thus evaluates thermoelectric performance when precise data on the thermal conductivity are not available. Obviously, a high value of the figure of merit ZT is achieved by creating a material with a high power factor and low thermal conductivity.

Figure 7 shows thermoelectric device (thermopile) built up of MWCNT (Bayer) and CNF/EOC flexible composite films and the schematic diagram showing the material junctions in series alternating hot/cold temperatures with each

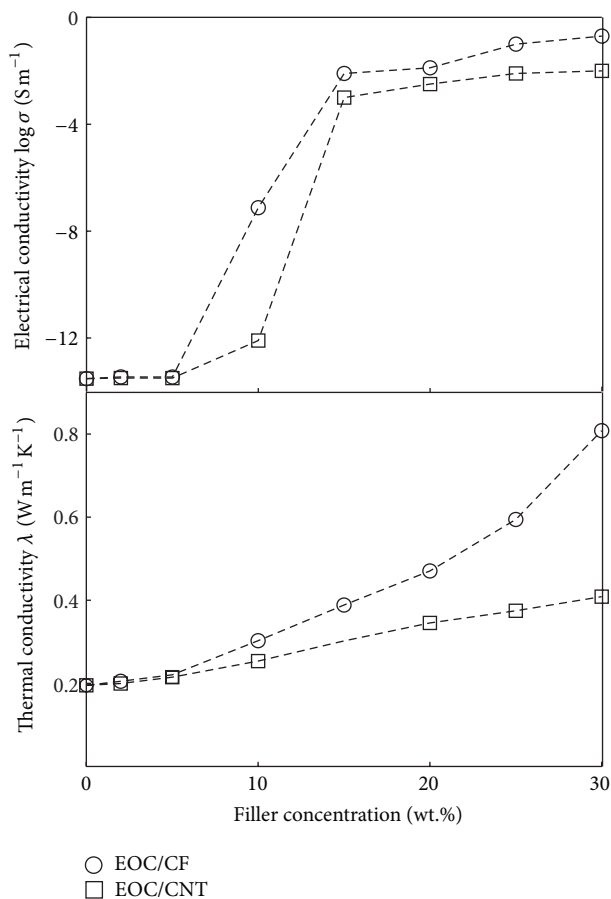


FIGURE 5: Filler concentration-dependent electrical and thermal conductivities of NCF/EOC composite and MWCNT(Sun)/EOC composite.

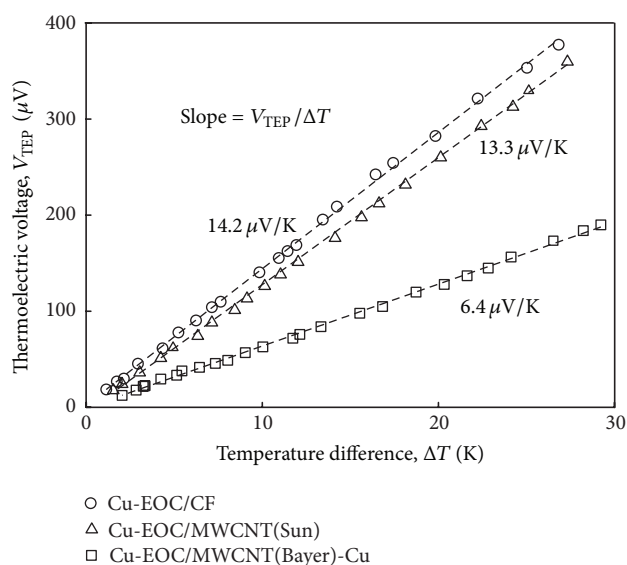


FIGURE 6: Generated electric voltage versus temperature difference for all investigated composites (filler concentration 30 wt%) together with the indicated thermoelectric power in $\mu\text{V/K}$.

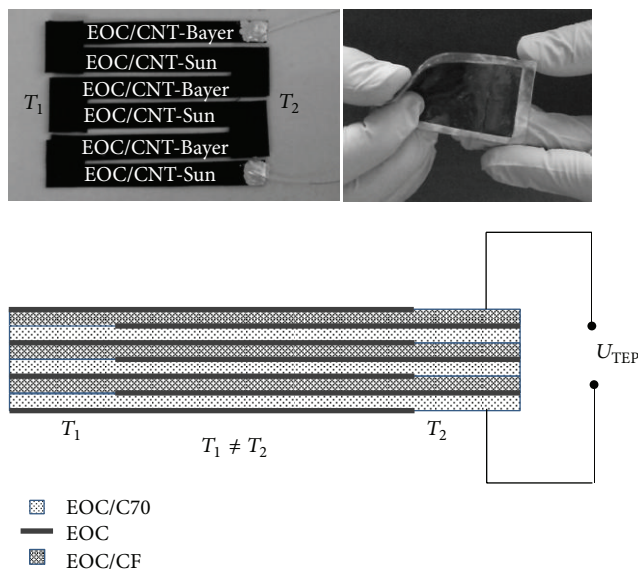


FIGURE 7: Thermoelectric device (thermopile) built up of MWCNT (Bayer) and CNF/EOC flexible composite films and the schematic diagram showing the material junctions in series alternating hot/cold temperatures with each junction.

junction. The measured temperature difference dependence of thermopile output voltage in the range of temperature difference -15 to 25°C is presented in Figure 8.

Our results showing the through-thickness thermoelectric properties of continuous CNF/EOC and MWCNT/EOC composites demonstrate that the electrical conductivity of polymer composites can be significantly increased by incorporating conductive nanoparticles, while the thermal conductivity increases moderately, in particular in case of MWCNT(Sun) filling. This behavior results probably from prevailing thermally disconnected but electrically well connected dispersed nanotubes. The low thermal conductivity of the composites contributes to a high figure of merit at room temperature. The decisive role of nanocomposite filler, the possible modification of its properties by a proper functionalization, dispersion, and concentration or arrangement into a segregated entangled network, makes it feasible to tune thermoelectric properties in favor of thermoelectric efficiency.

5. Conclusions

We have prepared deformable composites composed of multiwalled carbon nanotubes or carbon nanofibers and ethylene-octene copolymer. Their thermoelectric properties—the electric and thermal conductivity and the electric voltage produced per degree temperature difference—were measured. The calculated thermoelectric power values for MWCNT(Bayer)/EOC ($6.4 \mu\text{V/K}$), MWCNT(Sun)/EOC ($13.3 \mu\text{V/K}$), and CNF/EOC ($14.2 \mu\text{V/K}$) are in comparison with the thermoelectric power of classical metallic thermoelectrics low, but their thermal conductivity below 1 W/mK allows for a sustained temperature difference across the

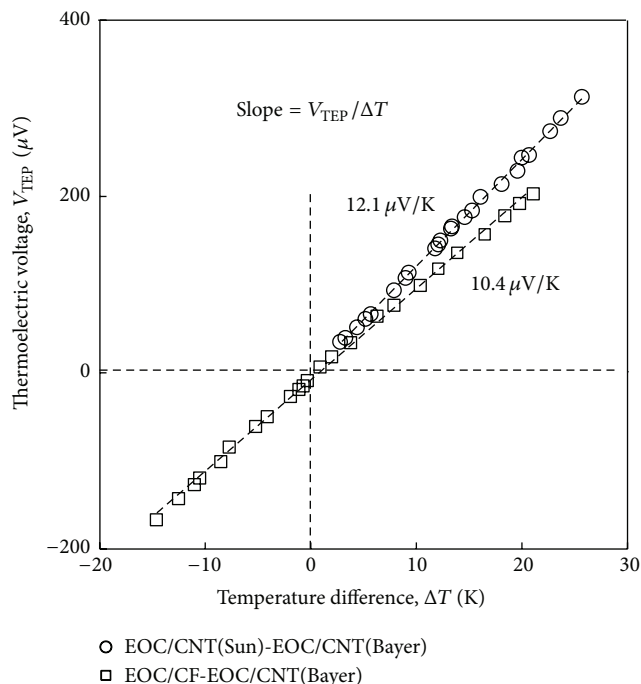


FIGURE 8: Temperature difference dependence of generated electric voltage by MWCNT(Sun)/EOC-MWCNT(Bayer)/EOC and MWCNT(Bayer)/EOC-CNF/EOC thermopiles.

composite. Moreover, the composite films are flexible and the created thermopile can be adjusted easily to a limited space and/or shape. Thus the combination of mechanical and thermoelectric properties of the composites may be advantageous, for instance, in applications where sources of waste heat have arbitrary shapes.

Conflict of Interests

The authors declare that they have no conflict of interests.

Acknowledgments

This project was supported by an internal Grant from TBU in Zlin no. IGA/FT/2013/018 funded by the resources of Specific University Research, by the Operational Program Research and Development for Innovations cofunded by the European Regional Development Fund (ERDF), by the National Budget of the Czech Republic within the framework of the Centre of Polymer Systems Project (registration no. CZ.1.05/2.1.00/03.0111), by the Operational Program “Education for Competitiveness” cofunded by the European Social Fund (ESF) and the National Budget of the Czech Republic within the “Advanced Theoretical and Experimental Studies of Polymer Systems” project (registration no. CZ.1.07/2.3.00/20.0104), and by the fund of Institute of Hydrodynamics AV0Z20600510.

References

- [1] B. I. Ismail and W. H. Ahmed, “Thermoelectric power generation using waste-heat energy as an alternative green technology,” *Recent Patents on Electrical Engineering*, vol. 2, no. 1, pp. 27–39, 2009.
- [2] C. A. Hewitt, A. B. Kaiser, S. Roth, M. Craps, R. Czerw, and D. L. Carroll, “Multilayered carbon nanotube/polymer composite based thermoelectric fabrics,” *Nano Letters*, vol. 12, no. 3, pp. 1307–1310, 2012.
- [3] C. A. Hewitt, A. B. Kaiser, S. Roth, M. Craps, R. Czerw, and D. L. Carroll, “Varying the concentration of single walled carbon nanotubes in thin film polymer composites, and its effect on thermoelectric power,” *Applied Physics Letters*, vol. 98, no. 18, Article ID 183110, 2011.
- [4] C. Yu, Y. S. Kim, D. Kim, and J. C. Grunlan, “Thermoelectric behavior of segregated-network polymer nanocomposites,” *Nano Letters*, vol. 8, no. 12, pp. 4428–4432, 2008.
- [5] J. Chen, X. Gui, Z. Wang et al., “Superlow thermal conductivity 3D carbon nanotube network for thermoelectric applications,” *ACS Applied Materials and Interfaces*, vol. 4, no. 1, pp. 81–86, 2012.
- [6] G. P. Moriarty, J. N. Wheeler, C. Yu, and J. C. Grunlan, “Increasing the thermoelectric power factor of polymer composites using a semiconducting stabilizer for carbon nanotubes,” *Carbon*, vol. 50, no. 3, pp. 885–895, 2012.
- [7] D. D. Freeman, K. Choi, and C. Yu, “N-type thermoelectric performance of functionalized carbon nanotube-filled polymer composites,” *PLoS ONE*, vol. 7, Article ID e47822, 2012.
- [8] C. Bounioux, P. Diaz-Chao, M. Campoy-Quiles et al., “Thermoelectric composites of poly(3-hexylthiophene) and carbon nanotubes with a large power factor,” *Energy and Environmental Science*, vol. 6, pp. 918–925, 2013.
- [9] Y. Du, S. Z. Shen, K. Cai, and P. S. Casey, “Research progress on polymer-inorganic thermoelectric nanocomposite materials,” *Progress in Polymer Science*, vol. 37, pp. 820–841, 2012.
- [10] G. H. Kim, L. Shao, K. Zhang, and K. P. Pipe, “Engineered doping of organic semiconductors for enhanced thermoelectric efficiency,” *Nature Materials*, vol. 12, pp. 719–723, 2013.
- [11] O. Bubnova and X. Crispin, “Towards polymer-based organic thermoelectric generators,” *Energy and Environmental Science*, vol. 5, pp. 9345–9362, 2012.
- [12] N. Toshima, N. Jiravanichanun, and H. Marutani, “Organic thermoelectric materials composed of conducting polymers and metal nanoparticles,” *Journal of Electronic Materials*, vol. 41, pp. 1735–1742, 2012.
- [13] R. Yue, S. Chen, C. Liu et al., “Synthesis, characterization, and thermoelectric properties of a conducting copolymer of 1,12-bis(carbazolyl)dodecane and thieno[3,2-b]thiophene,” *Journal of Solid State Electrochemistry*, vol. 16, no. 1, pp. 117–126, 2012.
- [14] K. Chatterjee, M. Mitra, K. Kargupta, S. Ganguly, and D. Banerjee, “Synthesis, characterization and enhanced thermoelectric performance of structurally ordered cable-like novel polyaniline-bismuth telluride nanocomposite,” *Nanotechnology*, vol. 24, Article ID 215703, 2013.
- [15] G. P. Moriarty, S. De, P. J. King et al., “Thermoelectric behavior of organic thin film nanocomposites,” *Journal of Polymer Science B*, vol. 51, pp. 119–123, 2013.
- [16] C. Yu, K. Choi, L. Yin, and J. C. Grunlan, “Light-weight flexible carbon nanotube based organic composites with large thermoelectric power factors,” *ACS Nano*, vol. 5, no. 10, pp. 7885–7892, 2011.

- [17] Z. Antar, J. F. Feller, H. Noël, P. Glouannec, and K. Elleuch, "Thermoelectric behaviour of melt processed carbon nanotube/graphite/poly(lactic acid) conductive biopolymer nanocomposites (CPC)," *Materials Letters*, vol. 67, no. 1, pp. 210–214, 2012.
- [18] P. Slobodian, P. Riha, A. Lengalova, and P. Saha, "Compressive stress-electrical conductivity characteristics of multiwall carbon nanotube networks," *Journal of Materials Science*, vol. 46, no. 9, pp. 3186–3190, 2011.
- [19] P. Slobodian, P. Riha, and P. Saha, "A highly-deformable composite composed of an entangled network of electrically-conductive carbon-nanotubes embedded in elastic polyurethane," *Carbon*, vol. 50, pp. 3446–3453, 2012.
- [20] J. E. Lozano, *Fruit Manufacturing: Scientific Basis, Engineering Properties, and Deteriorative Reactions of Technological Importance*, Springer, New York, NY, USA, 2006.
- [21] P. Svoboda, R. Theravalappil, S. Poongavalappil et al., "A study on electrical and thermal conductivities of ethylene-octene copolymer/expandable graphite composites," *Polymer Engineering and Science*, vol. 52, pp. 1241–1249, 2012.

Research Article

All-Solution-Processed $\text{InGaO}_3(\text{ZnO})_m$ Thin Films with Layered Structure

Sung Woon Cho,¹ Jun Hyeon Kim,¹ Sangwoo Shin,²
Hyung Hee Cho,² and Hyung Koun Cho¹

¹ School of Advanced Materials Science and Engineering, Sungkyunkwan University, 2066 Seobu-ro, Jangan-gu, Suwon, Gyeonggi-do 440-746, Republic of Korea

² Department of Mechanical Engineering, Yonsei University, Seoul 120-749, Republic of Korea

Correspondence should be addressed to Hyung Koun Cho; chohk@skku.edu

Received 14 June 2013; Revised 29 August 2013; Accepted 29 August 2013

Academic Editor: Chan Park

Copyright © 2013 Sung Woon Cho et al. This is an open access article distributed under the Creative Commons Attribution License, which permits unrestricted use, distribution, and reproduction in any medium, provided the original work is properly cited.

We fabricated the crystallized InGaZnO thin films by sol-gel process and high-temperature annealing at 900°C. Prior to the deposition of the InGaZnO, ZnO buffer layers were also coated by sol-gel process, which was followed by thermal annealing. After the synthesis and annealing of the InGaZnO, the InGaZnO thin film on the ZnO buffer layer with preferred orientation showed periodic diffraction patterns in the X-ray diffraction, resulting in a superlattice structure. This film consisted of nanosized grains with two phases of $\text{InGaO}_3(\text{ZnO})_1$ and $\text{InGaO}_3(\text{ZnO})_2$ in InGaZnO polycrystal. On the other hand, the use of no ZnO buffer layer and randomly oriented ZnO buffer induced the absence of the InGaZnO crystal related patterns. This indicated that the ZnO buffer with high *c*-axis preferred orientation reduced the critical temperature for the crystallization of the layered InGaZnO. The InGaZnO thin films formed with nanosized grains of two-phase $\text{InGaO}_3(\text{ZnO})_m$ superlattice showed considerably low thermal conductivity ($1.14 \text{ W m}^{-1} \text{ K}^{-1}$ at 325 K) due to the phonon scattering from grain boundaries as well as interfaces in the superlattice grain.

1. Introduction

The complex materials based on PbTe and SiGe have been considered for thermoelectric application due to high ZT values at mid- (500–900 K) and high- (>900 K) temperature range. Recently, it was reported that nanosized inclusions (in bulk system) or nanocomposites (in low-dimensional system) in host material enhance dimensionless thermoelectric figure of merit, $ZT = S^2\sigma T/\kappa$ (*S*: Seebeck coefficient, σ : electrical conductivity, *T*: temperature, and κ : thermal conductivity). There are two principle reasons for ZT increase. First, Seebeck coefficient is remarkably increased by energy filtering for electrons or holes with low energy. Second, thermal conductivity is decreased due to more frequent phonon scattering by new generated interfaces, which is the main reason for the dramatic ZT increase [1]. In PbTe

based materials, it was proven that nanoinclusions related to Pb, Sb, and Bi decrease thermal conductivity by forming numerous interfaces in PbTe matrix, theoretically [2] and experimentally [3]. In addition, p-type SiGe nanocomposite synthesized by sintering nanopowder also showed a half of thermal conductivity ($\kappa_{\text{nanocomposite}} = \sim 2.3 \text{ W m}^{-1} \text{ K}^{-1}$ at 1000 K) compared to that ($\kappa_{\text{bulk}} = \sim 4.5 \text{ W m}^{-1} \text{ K}^{-1}$ at 1000 K) of SiGe bulk due to new generated grain boundaries [4]. The oxide thermoelectric materials such as $\text{Na}_{0.75}\text{CoO}_2$ [5], $\text{Ca}_3\text{Co}_4\text{O}_9$ [6], and SrTiO_3 [7] have been researched for thermoelectric application at high temperature due to high chemical and thermal stability as well as nontoxic elements.

Over the past ten years, there has been a rising amount of interest in fabricating $\text{RAO}_3(\text{MO})_m$ (*R* = In and rare earth elements; *A* = Ga, In, Al, and Fe; *M* = Mg, Co, Cu, and Zn;

m = integer) superlattice structures due to their unexpected physical properties by quantum confinement effects [8, 9]. Thus, a multilayered oxide material with long-range periodic atomic arrangement shows exceptional properties, such as high field-effect mobility in thin-film transistors (TFTs) [10], giant magnetoresistance in ferromagnetic materials [11], and extremely high Seebeck coefficient as well as low thermal conductivity in thermoelectric materials [7]. Hosono group first suggested the $\text{InGaO}_3(\text{ZnO})_m$ film with multilayered structure on sapphire substrate by reactive solid-phase epitaxy method based on vacuum process [12]. In addition, the InGaZnO TFT using the $\text{InGaO}_3(\text{ZnO})_5$ superlattice grown by reactive solid-phase epitaxy as a channel layer exhibited high field-effect mobility ($\sim 80 \text{ cm}^2 \text{ V}^{-1} \text{ s}^{-1}$) [10]. As a similar approach, our group produced the $\text{InGaO}_3(\text{ZnO})_m$ superlattice film using advanced process based on solution process for thermoelectric application [13], because Dresselhaus et al. proposed that multilayered structure (superlattice) can remarkably improve thermoelectric properties [1].

In this study, an all-solution process for fabricating InGaZnO superlattice structure was developed based on the chemical reaction of InGaZnO solution and reactive solid phase epitaxy growth proposed by the Hosono group [12]. ZnO films were first deposited on sapphire substrates by sol-gel coating and then annealed at 900°C for 2 hours. Repeated coating processes led to the formation of ZnO thin film preferentially oriented along the c -axis. Then, amorphous InGaZnO was deposited on ZnO buffer by sol-gel coating and annealed at 900°C for 9 hours. This study is the first report on the synthesis of oxide thin films with superlattice structure based on all-solution method.

2. Experiments

The deposition of the ZnO buffer layer and amorphous InGaZnO layer was performed by sol-gel method. Indium nitrate hydrate [$\text{In}(\text{NO}_3)_3 \cdot \text{H}_2\text{O}$, Aldrich], gallium nitrate hydrate [$\text{Ga}(\text{NO}_3)_3 \cdot \text{H}_2\text{O}$, Aldrich], and zinc acetate dehydrate [$\text{Zn}(\text{CH}_3\text{COO})_2$, Aldrich] were used as the metal precursors, and 2-methoxyethanol (2ME, $\text{C}_3\text{H}_8\text{O}_2$) and monoethanolamine (MEA, $\text{C}_2\text{H}_7\text{NO}$) were employed as the solvent and stabilizer, respectively. First, ZnO buffer layers were prepared on sapphire substrates by repeated spin coating processes. The solution mixture consisted of zinc acetate dehydrate, 0.2 M 2ME and 0.3 M MEA, and was processed in a glove box under a nitrogen atmosphere (O_2 and H_2O < 10 ppm). After constant magnetic stirring at 400 rpm on a 70°C hot plate for 1 hour, stable ZnO sol was spin-coated on sapphire substrates at 3000 rpm for 30 s and dried at 250°C for 10 min. The coating process was repeated several times to achieve proper thickness, and postannealing was performed at 900°C for 2 hours for the crystallization of the ZnO film. Next, the zinc acetate, indium nitrate, and gallium nitrate were blended at a ratio of 1:1:1 and spin-coated on the ZnO buffer layer for the formation of the InGaZnO thin films, which was followed by postannealing at 900°C for 9 hours. The overall process for fabricating the InGaZnO thin films is schematically presented in Figure 1. This approach is the

same as the one from our previous report [13] except for the synthesis of ZnO seed layer.

Thermogravimetric analysis (TGA) and differential thermal analysis (DTA) were performed at temperatures ranging from room temperature to 400°C with a heating rate of $8^\circ\text{C}/\text{min}$ in air for regulating the chemical reaction temperature. The crystal phase of the crystallized InGaZnO thin films was investigated by X-ray diffraction (XRD) and transmission electron microscopy (TEM). The surface morphology of the buffer layers was observed by field-emission scanning electron microscopy (FE-SEM).

3. Results and Discussion

The TG-DTA results of InGaZnO sol are shown in Figure 2. There are two stages that can be seen at $55\text{--}110^\circ\text{C}$ and $230\text{--}250^\circ\text{C}$. The first weight loss at $55\text{--}110^\circ\text{C}$ indicates that Zn acetate, In nitrate, and Ga nitrate were decomposed and hydrolyzed to Zn-OH , In-OH , and Ga-OH . The second weight loss at $230\text{--}250^\circ\text{C}$ indicates dehydroxylation reaction of M-OH to M-O ($\text{M} = \text{Zn, In, Ga}$), and most organic products such as 2ME, CH_3COOH , and HNO_3 , as well as H_2O , were evaporated. The overall chemical reaction of the metal precursors for the formation of Zn-O , In-O , and Ga-O was explained in previous research [14]. The coating process was established with TG/DTA results, and high-temperature postannealing was performed for crystallization of these films. For the coating of the ZnO buffer layers, different solute concentrations and repetitions were used to induce different surface morphologies and to achieve proper buffer thicknesses, respectively. As shown in Figure 3(a), the solute concentration of 0.5 M with 2 coatings induced a rough surface with island shape, due to inhomogeneous Zn-O distribution coming from excessive solvent concentration. On the other hand, the solute concentration of 0.2 M with 5 coatings led to a homogeneous and flat surface (Figure 3(b)), after post annealing at 900°C for 2 hours similar to previous research [15]. In addition, the flat surface of the ZnO buffer layer was closely related to the strong c -axis preferred orientation. A more intense ZnO (0002) diffraction peak was observed in the InGaZnO thin film/flat ZnO buffer structure than in the InGaZnO thin film/rough ZnO buffer structure, as shown in Figures 4(b) and 4(c).

Through the solution-based synthesis of the ZnO and InGaZnO and thermal annealing, the crystallized InGaZnO thin films were grown on sapphire substrates with the help of the ZnO buffer layer with high c -axis preferred orientation. Figure 4 shows XRD patterns of InGaZnO thin films before and after annealing at 900°C for 9 hours on different ZnO buffer layers, where the InGaZnO thin film without ZnO buffer was used for comparison. In our study, the ZnO layer oriented along the c -axis acts as a seed layer for the enhanced crystallization of the InGaZnO thin films and finally disappears due to the complete intermixing of the ZnO and InGaZnO layers. The intermixing can be confirmed by no sign of the ZnO diffraction peaks after thermal annealing, as shown in Figures 4(e) and 4(f). As confirmed in Figures 4(a)

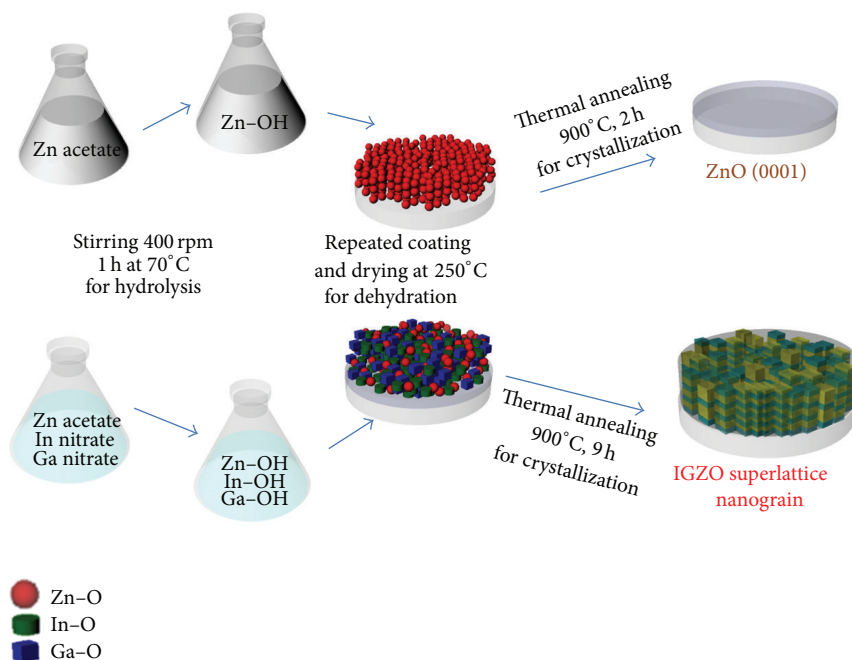


FIGURE 1: The overall fabrication process of the crystallized InGaZnO thin films with nanosize $\text{InGaO}_3(\text{ZnO})_m$ superlattice grains, which consisted of sol preparation, spin coating, and thermal annealing.

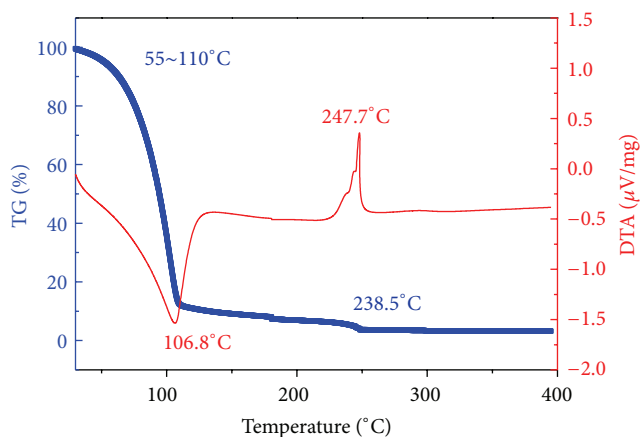


FIGURE 2: Thermogravimetric analysis and differential thermal analysis curves of the InGaZnO sol.

and 4(d), the sample without ZnO buffer shows faint crystallized diffraction patterns that are indexed as GaO, GaZnO, and so forth and are not related to any InGaZnO crystals. This indicates that higher annealing temperature is required for the crystallization of the InGaZnO thin film. Also, a similar result was observed in the sample with rough ZnO buffer layer (or less c -axis preferred orientation), as shown in Figure 4(e). However, it is noticeable that many InGaZnO-phases-related peaks were observed from the InGaZnO thin film on the ZnO buffer layer with strong c -axis preferred orientation, as shown in Figure 4(f). From the XRD data and JCPDS cards (nos. 38-1104 and 40-0252), the 2θ peaks at 10.2,

20.4, and 30.9° correspond to the (0003), (0006), and (0009) planes of the $\text{InGaO}_3(\text{ZnO})_1$ crystal phase, respectively, and the 2θ peaks at 15.8, 23.8, and 31.9° are in accordance with the (0004), (0006), and (0008) planes of the $\text{InGaO}_3(\text{ZnO})_2$ crystal phase, respectively. This result indicates that the ZnO buffer layer with c -axis preferred orientation promotes the crystallization of the InGaZnO thin films, and significantly reduces the crystallization temperature [16].

Figures 5(a)–5(c) show cross-sectional bright-field (BF) TEM image, selective area diffraction pattern (SADP), and high-resolution transmission electron microscopy image obtained from InGaZnO thin film using ZnO buffer layer with strong c -axis preferred orientation, respectively. The cross-sectional BF TEM image revealed that the InGaZnO film consists of nano-size grains with the dimension of 100~150 nm, and the film is polycrystal. The nano-size grains have the width of ~150 nm and the height of ~100 nm. As shown in Figures 5(b) and 5(c), SADP and HRTEM image show the existence of $\text{InGaO}_3(\text{ZnO})_m$ superlattice along the vertical direction, which is equivalent with XRD data. One nanograin in the bottom region of cross-sectional HRTEM image certainly shows $\text{InGaO}_3(\text{ZnO})_m$ superlattice in polycrystalline InGaZnO film.

We had already proven the effectiveness of the $\text{InGaO}_3(\text{ZnO})_m$ superlattice structure for improved thermoelectric properties [17], which was attributed to frequent phonon scattering at the interface of InO_2^- and $\text{GaO}(\text{ZnO})_m^+$ layer. In this survey, InGaZnO thin film fabricated by all-solution process is polycrystalline with nano-size grains of two-phase $\text{InGaO}_3(\text{ZnO})_m$ superlattice, which is expected to induce low thermal conductivity due to

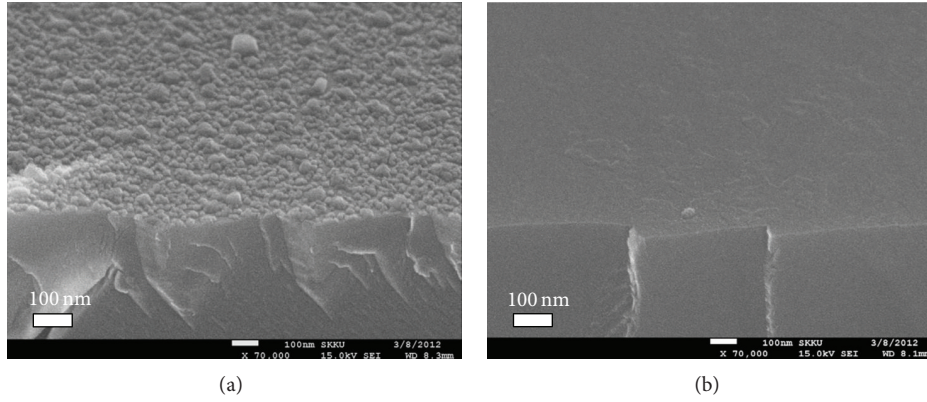


FIGURE 3: FE-SEM images of ZnO buffer layers with different coating conditions after annealing at 900°C for 2 hours; (a) 0.5 M, 2-time coated ZnO layer and (b) 0.2 M, 5-time coated ZnO layer.

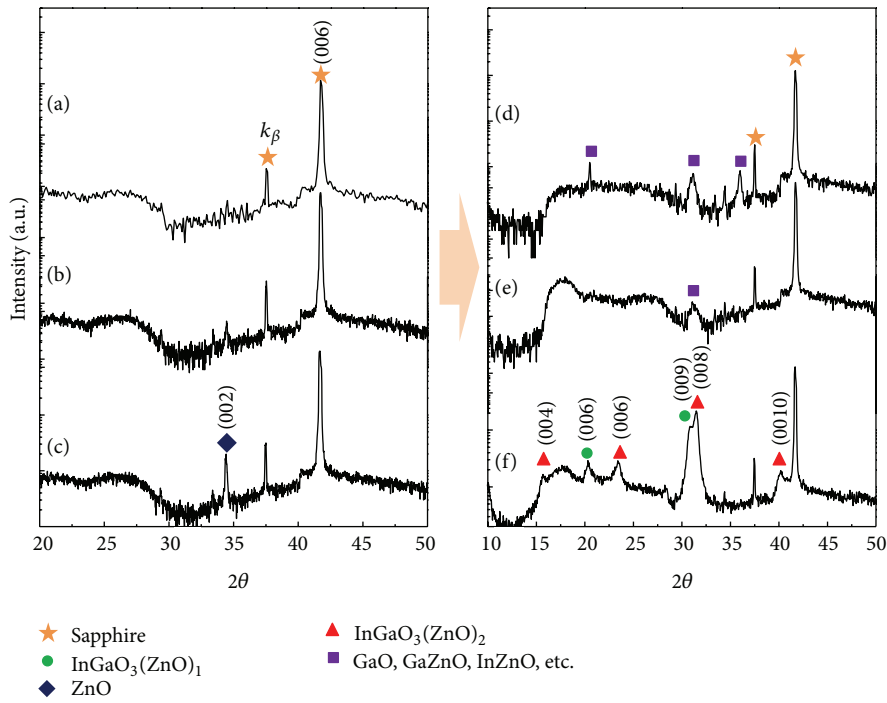


FIGURE 4: XRD patterns of InGaZnO thin films (a)–(c) before and (d)–(f) after annealing on different buffer layers. (a) and (d) without ZnO buffer, (b) and (e) randomly oriented ZnO buffer layer, and (c) and (f) preferentially oriented ZnO buffer layer.

frequent phonon scattering at the surface of nanograins as well as many interfaces in each $\text{InGaO}_3(\text{ZnO})_m$ superlattice nanograin, as shown in Figure 5(d). In previous report by Seo et al. [17], the polycrystalline InGaZnO thin film fabricated by sputtering exhibited high thermal conductivity ($7.53 \text{ Wm}^{-1} \text{ K}^{-1}$ at 300 K). In addition, thermal conductivities of ZnO-based materials were also quite high ($2\sim 10 \text{ Wm}^{-1} \text{ K}^{-1}$) [18–20]. On the contrary, the polycrystalline InGaZnO thin film with superlattice nanograins fabricated by all-solution process showed considerably low thermal conductivity ($1.14 \text{ Wm}^{-1} \text{ K}^{-1}$ at 325 K and $0.99 \text{ Wm}^{-1} \text{ K}^{-1}$ at 355 K).

4. Conclusions

Semiconducting ZnO-based oxide thin films had been developed for various electronic and optoelectronic applications such as transparent TFTs, optical and chemical sensors, and thermoelectrics. These applications can be improved by using layered structures as an active layer. In this study, InGaZnO thin films were fabricated by an all-solution process. Unlike the single phase $\text{InGaO}_3(\text{ZnO})_m$ observed in InGaZnO thin film using an epitaxial ZnO buffer grown by vacuum deposition process, the solution-processed ZnO buffer layer with preferred orientation along the c -axis resulted in polycrystalline InGaZnO

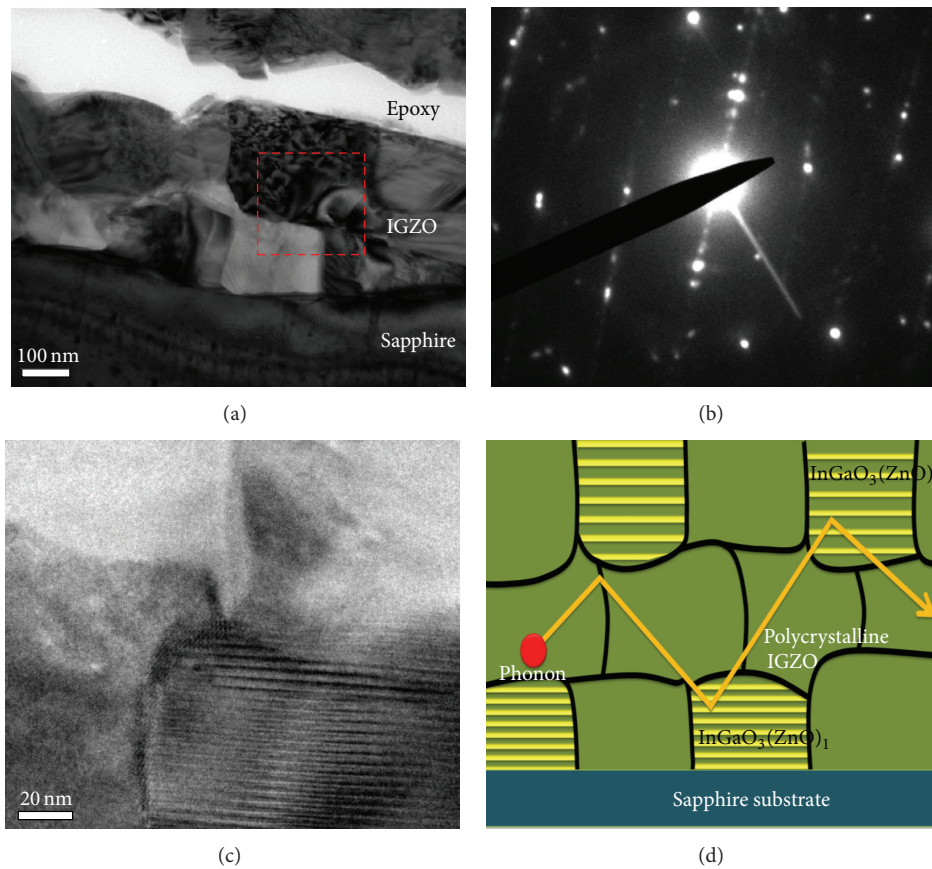


FIGURE 5: (a) Cross-sectional bright-field TEM image, (b) selective area diffraction pattern (SADP) and (c) HRTEM image obtained from $\text{InGaO}_3(\text{ZnO})_m$ thin film on ZnO buffer layer with strong c -axis preferred orientation. (d) Frequent phonon scattering at the surface of nano-grains as well as the interfaces of the $\text{InGaO}_3(\text{ZnO})_m$ superlattice.

film formed with the crystal grains of two phases, such as $\text{InGaO}_3(\text{ZnO})_1$ and $\text{InGaO}_3(\text{ZnO})_2$. We also obtained extremely low thermal conductivity ($1.14 \text{ Wm}^{-1} \text{ K}^{-1}$ at 325 K). This was due to frequent phonon scattering at the surface of nanograins as well as the interfaces of the $\text{InGaO}_3(\text{ZnO})_m$ superlattice.

Authors' Contribution

Sung Woon Cho and Jun Hyeon Kim contributed equally to this work.

Acknowledgments

This research was supported by the Basic Science Research Program (2012-0001447) and the Mid-Career Researcher Program (Grant no. 2012-003849) through the National Research Foundation of Korea (NRF) funded by the Ministry of Education, Science and Technology.

References

- [1] M. S. Dresselhaus, G. Chen, M. Y. Tang et al., "New directions for low-dimensional thermoelectric materials," *Advanced Materials*, vol. 19, no. 8, pp. 1043–1053, 2007.
- [2] S. V. Faleev and F. Léonard, "Theory of enhancement of thermoelectric properties of materials with nanoinclusions," *Physical Review B*, vol. 77, no. 21, Article ID 214304, 2008.
- [3] J. He, J. R. Sootsman, S. N. Girard et al., "On the origin of increased phonon scattering in nanostructured pbte based thermoelectric materials," *Journal of the American Chemical Society*, vol. 132, no. 25, pp. 8669–8675, 2010.
- [4] G. Joshi, H. Lee, Y. Lan et al., "Enhanced thermoelectric figure-of-merit in nanostructured p-type silicon germanium bulk alloys," *Nano Letters*, vol. 8, no. 12, pp. 4670–4674, 2008.
- [5] I. Terasaki, Y. Sasago, and K. Uchinokura, "Large thermoelectric power in NaCo_2O_4 single crystals," *Physical Review B*, vol. 56, no. 20, pp. R12685–R12687, 1997.
- [6] M. Shikano and R. Funahashi, "Electrical and thermal properties of single-crystalline $(\text{Ca}_2\text{CoO}_3)_{0.7}\text{CoO}_2$ with a $\text{Ca}_3\text{Co}_4\text{O}_9$ structure," *Applied Physics Letters*, vol. 82, no. 12, pp. 1851–1853, 2003.
- [7] H. Ohta, S. Kim, Y. Mune et al., "Giant thermoelectric Seebeck coefficient of a two-dimensional electron gas in SrTiO_3 ," *Nature Materials*, vol. 6, no. 2, pp. 129–134, 2007.
- [8] H. Hiramatsu, W. S. Seo, and K. Koumoto, "Electrical and optical properties of radio-frequency-sputtered thin films of $(\text{ZnO})_5\text{In}_2\text{O}_3$," *Chemistry of Materials*, vol. 10, no. 10, pp. 3033–3039, 1998.
- [9] J. L. F. Da Silva, Y. Yan, and S. H. Wei, "Rules of structure formation for the homologous $\text{InMO}_3(\text{ZnO})_n$ compounds," *Physical Review Letters*, vol. 100, no. 25, Article ID 255501, 2008.

- [10] K. Nomura, H. Ohta, K. Ueda, T. Kamiya, M. Hirano, and H. Hosono, "Thin-film transistor fabricated in single-crystalline transparent oxide semiconductor," *Science*, vol. 300, no. 5623, pp. 1269–1272, 2003.
- [11] K. Ueda, H. Tabata, and T. Kawai, "Ferromagnetism in LaFeO_3 - LaCrO_3 superlattices," *Science*, vol. 280, no. 5366, pp. 1064–1066, 1998.
- [12] H. Ohta, K. Nomura, M. Orita et al., "Single-crystalline films of the homologous series $\text{InGaO}_3(\text{ZnO})_m$ grown by reactive solid-phase epitaxy," *Advanced Functional Materials*, vol. 13, no. 2, pp. 139–144, 2003.
- [13] J. H. Kim, D. K. Seo, C. H. Ahn, S. W. Shin, H. H. Cho, and H. K. Cho, "Hybrid solution processed $\text{InGaO}_3(\text{ZnO})_m$ thin films with periodic layered structures and thermoelectric properties," *Journal of Materials Chemistry*, vol. 22, no. 32, pp. 16312–16317, 2012.
- [14] G. H. Kim, H. S. Shin, B. D. Ahn, K. H. Kim, W. J. Park, and H. J. Kim, "Formation mechanism of solution-processed nanocrystalline InGaZnO thin film as active channel layer in thin-film transistor," *Journal of the Electrochemical Society*, vol. 156, no. 1, pp. H7–H9, 2009.
- [15] M. Ohyama, H. Kozuka, and T. Yoko, "Sol-gel preparation of ZnO films with extremely preferred orientation along (002) plane from zinc acetate solution," *Thin Solid Films*, vol. 306, no. 1, pp. 78–85, 1997.
- [16] D. K. Seo, B. H. Kong, and H. K. Cho, "Composition controlled superlattice $\text{InGaO}_3(\text{ZnO})_m$ thin films by thickness of ZnO buffer layers and thermal treatment," *Crystal Growth and Design*, vol. 10, no. 10, pp. 4638–4641, 2010.
- [17] D. K. Seo, S. Shin, H. H. Cho, B. H. Kong, D. M. Whang, and H. K. Cho, "Drastic improvement of oxide thermoelectric performance using thermal and plasma treatments of the InGaZnO thin films grown by sputtering," *Acta Materialia*, vol. 59, no. 17, pp. 6743–6750, 2011.
- [18] Z. X. Huang, Z. A. Tang, J. Yu, and S. Bai, "Thermal conductivity of nanoscale polycrystalline ZnO thin films," *Physica B*, vol. 406, no. 4, pp. 818–823, 2011.
- [19] Y. Masuda, M. Ohta, W. S. Seo, W. Pitschke, and K. Koumoto, "Structure and thermoelectric transport properties of iso-electronically substituted $(\text{ZnO})_5\text{In}_2\text{O}_3$," *Journal of Solid State Chemistry*, vol. 150, no. 1, pp. 221–227, 2000.
- [20] L. D. Zhao, Y. L. Pei, Y. Liu, D. Berardan, and N. Dragoe, " InFeZnO_4 as promising thermal barrier coatings," *Journal of the American Ceramic Society*, vol. 94, no. 6, pp. 1664–1666, 2011.

Research Article

Thermoelectric Properties of Al-Doped Mesoporous ZnO Thin Films

**Min-Hee Hong,¹ Chang-Sun Park,¹ Won-Seon Seo,²
Young Soo Lim,² Jung-Kun Lee,³ and Hyung-Ho Park¹**

¹ Department of Materials Science and Engineering, Yonsei University, Seoul 120-749, Republic of Korea

² Korea Institute of Ceramic Engineering and Technology, Seoul 153-801, Republic of Korea

³ Department of Mechanical Engineering and Materials Science, University of Pittsburgh, Pittsburgh, PA 15261, USA

Correspondence should be addressed to Hyung-Ho Park; hypark@yonsei.ac.kr

Received 7 June 2013; Accepted 25 August 2013

Academic Editor: Chan Park

Copyright © 2013 Min-Hee Hong et al. This is an open access article distributed under the Creative Commons Attribution License, which permits unrestricted use, distribution, and reproduction in any medium, provided the original work is properly cited.

Al-doped mesoporous ZnO thin films were synthesized by a sol-gel process and an evaporation-induced self-assembly process. In this work, the effects of Al doping concentration on the electrical conductivity and characterization of mesoporous ZnO thin films were investigated. By changing the Al doping concentration, ZnO grain growth is inhibited, and the mesoporous structure of ZnO is maintained during a relatively high temperature annealing process. The porosity of Al-doped mesoporous ZnO thin films increased slightly with increasing Al doping concentration. Finally, as electrical conductivity was increased as electrons were freed and pore structure was maintained by inhibiting grain growth, the thermoelectric property was enhanced with increasing Al concentration.

1. Introduction

Development of alternative energy is very important because fossil fuels are being rapidly depleted. Thermoelectricity is a very important green energy conversion technique, as waste heat could be used. When materials have a temperature gradient, electric current is generated in the materials. To maintain a high thermoelectric property, factors of Seebeck coefficient, electrical conductivity, and thermal conductivity need to be controlled individually. However, among thermoelectric factors, electrical conductivity and thermal conductivity have a proportional relationship. To overcome this problem, studies on structure change have been performed, including studies on nanostructures, nanowires, and superlattices [1]. Of the structures studied, mesoporous structures could be adapted to thermoelectrics because mesoporous structures have low thermal conductivity. Mesoporous materials have pores that range between 2 and 50 nm [2]. Because of their pore structure, mesoporous structures have properties such as a high specific surface area, low dielectric constant, and low thermal conductivity. In the evaporation-induced self-assembly (EISA) process, a micelle structure is formed and

an ordered pore structure is synthesized after the annealing process. When the surfactant concentration exceeds the critical micelle concentration, the EISA process progresses. Good thermoelectric materials have high Seebeck coefficient and electrical conductivity and low thermal conductivity. The order of the pore structure is very important to controlling the electrical conductivity and the thermal conductivity individually because the inelastic mean free path of electrons and phonons is different. This difference is generally referred to as the phonon-glass electron crystal (PGEC) effect. Because the inelastic mean free path of an electron is longer than that of a phonon, phonons are scattered effectively in ordered mesoporous structures [3, 4]. In order to maximize the PGEC effect, a doping source with an inhibited grain growth property is used because its ordered pore structure is less prone to collapse.

Zinc oxide (ZnO) is an important n-type wide band gap semiconductor material used in various applications such as photovoltaic devices [5], gas sensors [6], and solar cells [7]. By using physical vapor deposition, chemical vapor deposition, and the sol-gel process [8–10], ZnO thin films can be easily synthesized. In this work, the sol-gel process was

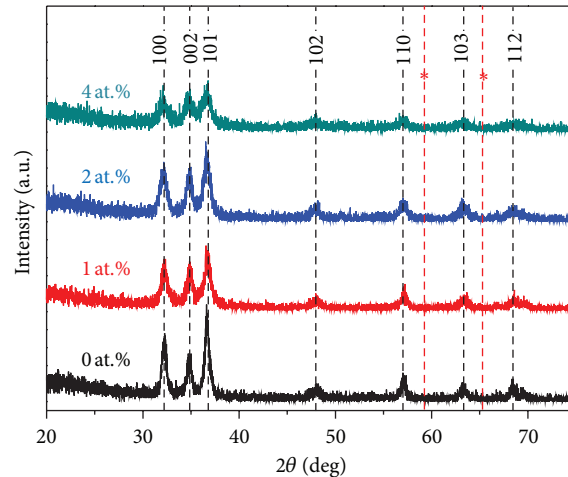


FIGURE 1: Wide-angle XRD patterns of Al-doped mesoporous ZnO thin films with various Al doping concentrations (* represents a typical diffraction peak position of ZnAl_2O_4 at high angle 2 theta region).

selected to adapt the EISA process. ZnO could be doped with various group III materials such as In, Ga, and Al. Among the many doping materials, Al-doped ZnO thin films are most important for this application. Because Al-doped ZnO thin films have high thermal stability and are inexpensive, they have been studied as possible next-generation materials to replace indium tin oxides [11]. In this work, Al was doped to increase its thermoelectric properties. When Al was doped in ZnO, the electrical conductivity was increased [12]. Moreover, the grain growth of ZnO was effectively inhibited [13]. In Al doping, Al ions are substituted at Zn ion sites. In this process, the hexagonal wurtzite structure is distorted because of the difference in the radius of Al^{3+} (0.054 nm) and Zn^{2+} (0.074 nm). Finally, the crystalline structure deteriorates because when stress forms in thin films, the grain growth of the hexagonal wurtzite structure is inhibited. In a mesoporous structure, high temperature stability is essential to maintaining an ordered pore structure. An Al-doped mesoporous ZnO thin film could have good thermoelectric properties because it has a high electrical conductivity and high temperature stability due to inhibited grain growth. In this paper, the effects of Al concentration on the pore arrangement in mesoporous ZnO thin films and on the crystallization, pore structure, porosity, and thermoelectric property of the film were analyzed.

2. Experimental Procedure

Al-doped mesoporous ZnO thin films were prepared on SiO_2/Si substrates by sol-gel and spin coating processes. Zinc acetate dihydrate [$\text{Zn}(\text{CH}_3\text{COO})_2 \cdot \text{H}_2\text{O}$], n-propanol, Brij-76 ($\text{C}_{58}\text{H}_{118}\text{O}_{21}$, Aldrich, MW 711), aluminum nitrate nonahydrate [$\text{Al}(\text{NO}_3)_3 \cdot 9\text{H}_2\text{O}$], and monoethanolamine (MEA) were used as Zn precursor, solvent, surfactant, dopant source, and complex agent, respectively. The molar ratios of MEA/Zn precursor and surfactant/Zn precursor were fixed at 1 and 0.05 in this work. The molar ratio of zinc acetate dihydrate : Brij-76 : MEA : n-propanol was 1 : 0.05 : 1 : 34.5. The atomic ratio

of Al precursor and Zn precursor was changed from 0 at.% to 4 at.%. The precursor solutions were spin coated onto SiO_2/Si substrate. Solvent was evaporated during the spin coating process. Then, the EISA process was started in the thin films and a micelle structure was synthesized. As-prepared thin films were preheated at 300°C for 10 min to remove residual organics. After preheating, Al-doped mesoporous ZnO thin films were annealed at 650°C for 4 h. To investigate the resulting ordered pore structure, small-angle X-ray diffraction (SAXRD) was performed with Cu $K\alpha$ radiation ($\lambda = 1.5418 \text{ \AA}$) at angles of 1° to 5° . Grazing incidence small-angle X-ray scattering (GISAXS) at the 3C beam line ($\lambda = 1.54 \text{ \AA}$ and $\Delta\lambda/\lambda = 5 \times 10^{-4}$) of the Pohang Light Source (PLS) in Korea was also used to investigate the pore arrangement of the thin film [14]. Porosity was measured with an ellipsometer (Gatan LII7C, 632.8 nm He-Ne laser) and calculated using the Lorentz-Lorenz equation [15]. The thermoelectric properties of Al-doped ZnO thin films were measured by detecting the Seebeck voltage with SEEPEL thermoelectric properties measurement system (TEP 850) and the temperature difference from 323 K to 478 K at intervals of 50 K in flowing helium gas atmosphere.

3. Results and Discussion

Regardless of Al concentration, all mesoporous ZnO thin films have a hexagonal wurtzite structure. Diffraction peaks at 31.8° , 33.4° , and 36.2° were indexed as 100, 002, and 101, respectively. A distinguished diffraction peak from ZnAl_2O_4 secondary phase was not observed at around 59.3° and 65.2° of 2 theta (JCPDS card no. 82-1043), although a formation of ZnAl_2O_4 has been reported with doping of Al more than solubility limit in ZnO structure, for example, around 3 at.% of Al [16]. However, all samples had the same crystal phase and hexagonal wurtzite structure, peak intensity decreased with increasing Al concentration, as shown in Figure 1. Because of the smaller radius of Al^{3+} (0.054 nm) compared with that of Zn^{2+} (0.074 nm), crystallization of ZnO was

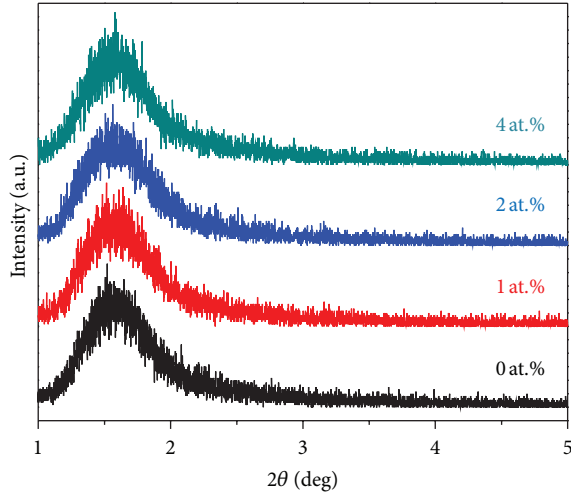


FIGURE 2: Small-angle XRD patterns of Al-doped mesoporous ZnO thin films with various Al doping concentrations.

inhibited by Al doping. Furthermore undetected ZnAl_2O_4 secondary phase from the XRD measurement might act a grain boundary pinning site, that is, grain growth inhibitor. Based on this result, the grain growth of ZnO was inhibited with increasing Al concentration. The Al doping process enhances electrical conductivity via n-type dopant and pore structure reinforcement in a mesoporous ZnO structure, which acts as a grain growth inhibitor during the high-temperature annealing process. In general, the crystallization of ZnO is started at low temperatures in the sol-gel process [12]. Because of grain growth in skeleton-structured ZnO, the pore structure of mesoporous ZnO could collapse easily. However, with Al doping, grain growth could be inhibited effectively and pore structure could be maintained compared with mesoporous pure ZnO. To investigate the relationship between crystallization and an ordered pore structure, SAXRD was used in the range of 1° to 5° . As shown in Figure 2, broad SAXRD peaks could be observed at around 1.61° of 2θ in all samples. All samples showed broad diffraction peaks, which suggests that a partially ordered pore structure is present in the thin films [17]. Because of the high-temperature annealing, the ordered pore structure collapsed and was replaced with a partially ordered pore structure, as shown at Figure 2. The partially ordered structure showed a broad peak at around 1.61° . Regardless of Al concentration, peak intensity was also very similar to pure mesoporous ZnO and Al-doped samples. All samples showed an interpore distance of 5.47 nm. The hexagonal wurtzite structure is inhibited by Al doping [18] so that the pore structure is affected. GISAXS analysis was used to analyze the pore structure in more detail. When an X-ray is scattered at the surface of a sample at a low grazing incidence, an X-ray is emitted due to changes in the surface density. Because the emitted X-ray strikes the two-dimensional detector in the horizontal and vertical dimensions, the pore structure can be analyzed in detail [19]. As shown in Figure 3, the GISAXS pattern was enlarged in the horizontal directions

with increasing Al concentration. In GISAXS, enlargement in the scattering pattern in the horizontal or vertical directions indicates an ordered pore structure in the horizontal or vertical directions in the thin film. In the case of pure mesoporous ZnO thin films, a partially ordered pore structure pattern and scattering pattern were observed together, meaning that the ordered pore structure exists partially in the horizontal and vertical direction in thin films. However, as the Al doping concentration increased, the partially ordered pore structure scattering pattern in the horizontal direction became more apparent. As shown in Figure 3, the ordering of the pore arrangement was enhanced by increased Al concentration. Based on this result, the partially ordered pore structures of Al-doped mesoporous ZnO thin films were maintained because the grain growth of hexagonal wurtzite was effectively inhibited.

The grain growth of ZnO was prevented by Al doping. The pore arrangement also changed, as shown in Figure 3. This change in the pore arrangement could affect porosity. The variation in porosity with Al doping in the mesoporous structure was calculated using the Lorentz-Lorenz equation.

Consider

$$1 - F_p = \frac{(n_f^2 - 1) / (n_f^2 + 2)}{(n_a^2 - 1) / (n_a^2 + 2)}, \quad (1)$$

where F_p is the pore volume fraction, n_f is the refractive index of the film, and n_a is the refractive index of air. Figure 4 shows the variation in the porosity of Al-doped mesoporous ZnO thin films. As Al concentration changed, porosity also changed slightly from 34% to 39%. Although the porosity was decreased at 4 at.% Al doping, the porosity tends to increase slightly with Al doping concentration. Because the grain growth of ZnO was inhibited, the pore structure collapsed less at the same annealing temperature, and the porosity increased slightly. Based on this result, we conclude that about 5% of porosity could be affected by grain growth.

Figure 5 shows the change in the Seebeck coefficient at various Al doping concentrations. All Seebeck coefficient values are in the negative range because ZnO is n-type. When the Al concentration increases to 2 at.%, the Seebeck coefficient is decreased. Because the number of free electrons increases, the carrier concentration in the ZnO thin film increases. In general, the Seebeck coefficient and carrier concentration are inversely related. The Seebeck coefficient value decreases as the Al doping process progresses. When Al is doped at 0 at.% in mesoporous ZnO thin films, the highest Seebeck coefficient at 383 K is $-75.72 \mu\text{V/K}$. Although the Seebeck coefficient is at a minimum when the Al concentration is 2 at.% with a value of $-63.58 \mu\text{V/K}$ at 383 K, the decrease in the Seebeck coefficient was not large. The electrical conductivity was higher due to the increase in free electrons. The thermal conductivity declined because the ordered pore structure was maintained better than in pure mesoporous ZnO.

Electrical conductivity at various Al concentrations is shown in Figure 6. The electrical conductivity increased with increased Al concentration. The average electrical conductivity values of 0, 1, 2, and 4 at.% Al-doped mesoporous ZnO thin

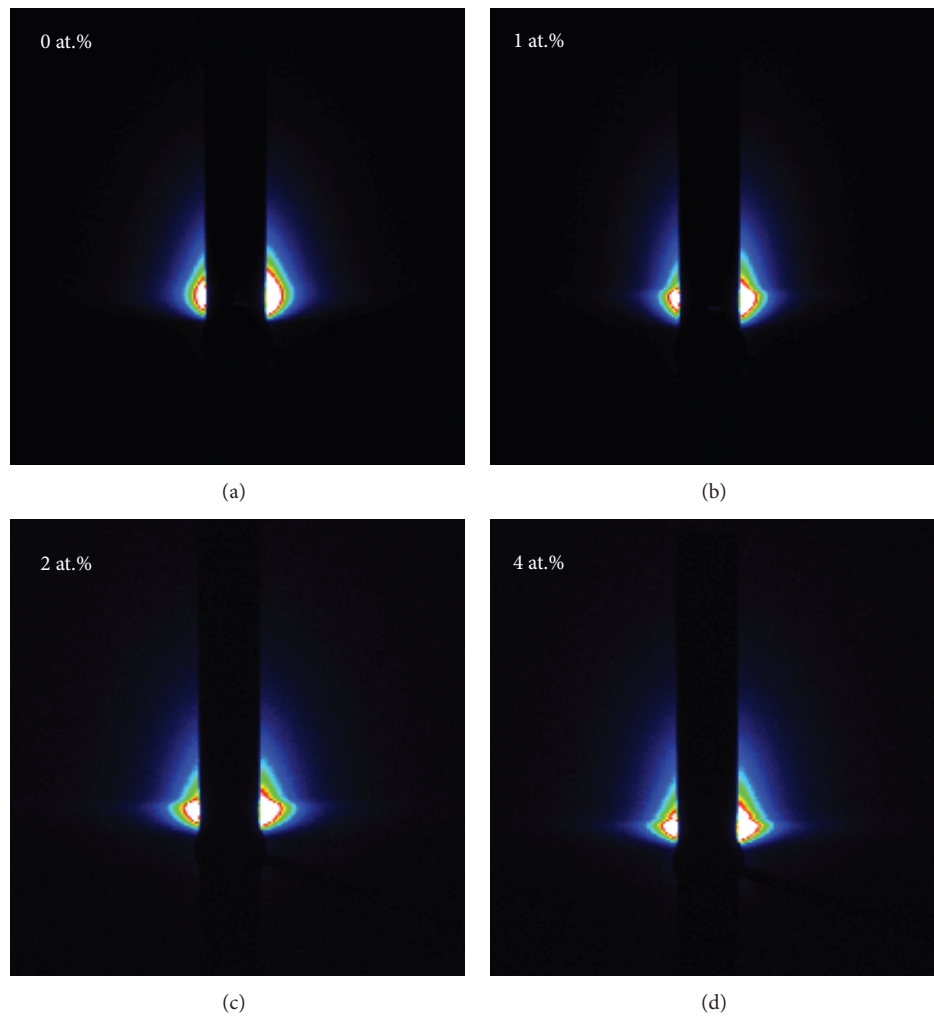


FIGURE 3: GISAXS patterns of Al-doped mesoporous ZnO thin films with various Al doping concentrations.

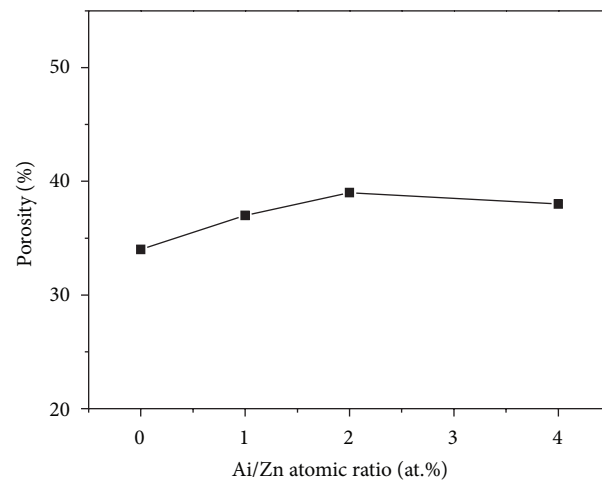


FIGURE 4: Porosity change in Al-doped mesoporous ZnO thin films with various Al doping concentrations.

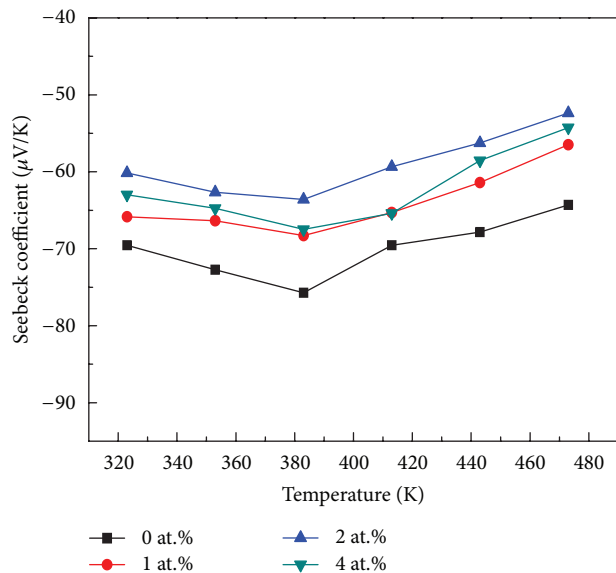


FIGURE 5: Seebeck coefficients of Al-doped mesoporous ZnO thin films with various Al doping concentrations.

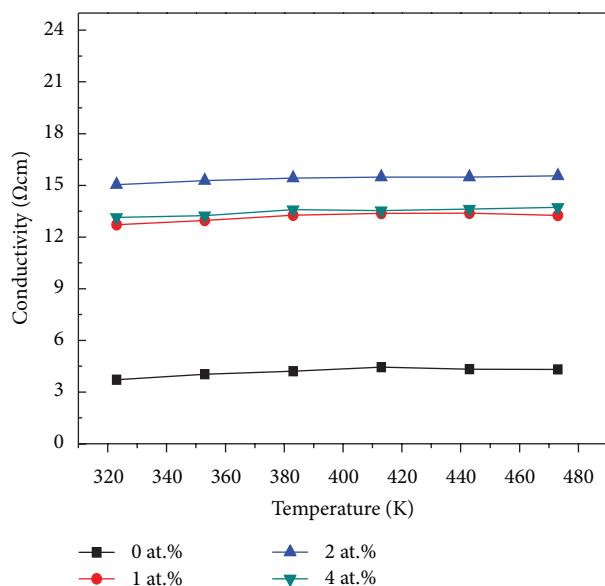


FIGURE 6: Electrical conductivity changes in Al-doped mesoporous ZnO thin films with various Al doping concentrations.

films were 4.17, 13.15, 15.37, and 13.47/ Ωcm . When compared with pure mesoporous ZnO, the electrical conductivities increased by about 3.5 times. Mesoporous ZnO thin films with 2 at.% Al doping showed the highest electrical conductivity. However, in the case of 4 at.% Al doping, the electrical conductivity decreased slightly due to increased scattering at the center due to excess Al doping [20]. Comparing the Seebeck coefficient and electrical conductivity, it can be seen that Al doping in mesoporous ZnO enhanced the thermoelectric properties. Although the Seebeck coefficient decreased, the increase in electrical conductivity is very

high, and thus the thermoelectric properties increased. For example, when Al is doped in mesoporous ZnO, the Seebeck coefficient decreases by about 20%. However, electrical conductivity increases by about 3.5 times. For this reason, the power factor ($S^2\sigma$) increased by a factor of 3. When Al is used to dope ZnO, the thermal conductivity of the electron term is increased. However, the contribution of the electron in thermal conductivity was very small [21]. The thermal conductivity of the phonon might have decreased, because the grain growth in ZnO is inhibited, which maximizes the PGEC effect. Finally, the thermoelectric properties of mesoporous ZnO thin films could be increased with an Al doping process.

4. Conclusion

In this work, Al-doped mesoporous ZnO thin film was synthesized. The Al doping concentration was varied from 0 at.% to 4 at.% to investigate the crystal structure and thermoelectric properties. The phase formation of ZnO with hexagonal wurtzite structure and the grain growth were inhibited from an increased doping concentration of Al. Therefore, a partially ordered pore structure could be maintained after anneal by doping with Al. Although the Seebeck coefficient was decreased with increasing Al concentration, the decrease in the Seebeck coefficient was relatively small and the increase in the electrical conductivity was large. The thermoelectric properties were enhanced by a factor of 3 as the Al doping concentration increased. As a result, the mesoporous ZnO thin film showed better thermoelectric properties after Al doping.

Acknowledgments

This research was supported by a Grant from the Fundamental R&D Program (Grant no. K0006007) for the Core Technology of Materials funded by the Ministry of Knowledge Economy, Republic of Korea. This work was also supported by the National Research Foundation of Korea (NRF) Grant funded by the Korean government (MEST) (no. 2012R1A2A2A01011014). Experiments at PLS were supported in part by MEST and POSTECH.

References

- [1] M. S. Dresselhaus and L. D. Hicks, "Effect of quantum-well structures on the thermoelectric figure of merit," *Physical Review B*, vol. 47, no. 19, pp. 12727–12731, 1993.
- [2] G. J. Soler-Illia, C. Sanchez, B. Lebeau, and J. Patarin, "Chemical strategies to design textured materials: from microporous and mesoporous oxides to nanonetworks and hierarchical structures," *Chemical Reviews*, vol. 102, no. 11, pp. 4093–4138, 2002.
- [3] D. M. Rowe, *CRC Handbook of Thermoelectrics*, CRC Press, New York, NY, USA, 1995.
- [4] G. J. Snyder, M. Christensen, E. Nishibori, T. Caillat, and B. B. Iversen, "Disordered zinc in Zn_4Sb_3 with phonon-glass and electron-crystal thermoelectric properties," *Nature Materials*, vol. 3, no. 7, pp. 458–463, 2004.

- [5] Q. Zhang, C. S. Dandeneau, X. Zhou, and C. Cao, "ZnO nanostructures for dye-sensitized solar cells," *Advanced Materials*, vol. 21, no. 41, pp. 4087–4108, 2009.
- [6] H.-W. Ra, K.-S. Choi, J.-H. Kim, Y.-B. Hahn, and Y.-H. Im, "Fabrication of ZnO nanowires using nanoscale spacer lithography for gas sensors," *Small*, vol. 4, no. 8, pp. 1105–1109, 2008.
- [7] Q. Zhang, C. S. Dandeneau, X. Zhou, and C. Cao, "ZnO nanostructures for dye-sensitized solar cells," *Advanced Materials*, vol. 21, no. 41, pp. 4087–4108, 2009.
- [8] Y. Natsume and H. Sakata, "Zinc oxide films prepared by sol-gel spin-coating," *Thin Solid Films*, vol. 372, no. 1-2, pp. 30–36, 2000.
- [9] M. Smirnov, C. Baban, and G. I. Rusu, "Structural and optical characteristics of spin-coated ZnO thin films," *Applied Surface Science*, vol. 256, no. 8, pp. 2405–2408, 2010.
- [10] T. Sahoo, M. Kim, M.-H. Lee et al., "Nanocrystalline ZnO thin films by spin coating-pyrolysis method," *Journal of Alloys and Compounds*, vol. 491, no. 1-2, pp. 308–313, 2010.
- [11] S. Fujihara, C. Sasaki, and T. Kimura, "Crystallization behavior and origin of c-axis orientation in sol-gel-derived ZnO:Li thin films on glass substrates," *Applied Surface Science*, vol. 180, no. 3-4, pp. 341–350, 2001.
- [12] Z.-Q. Xu, H. Deng, Y. Li, and H. Cheng, "Al-doping effects on structure, electrical and optical properties of c-axis-orientated ZnO:Al thin films," *Materials Science in Semiconductor Processing*, vol. 9, no. 1–3, pp. 132–135, 2006.
- [13] S. Mridha and D. Basak, "Aluminium doped ZnO films: electrical, optical and photoresponse studies," *Journal of Physics D*, vol. 40, no. 22, pp. 6902–6907, 2007.
- [14] B. Lee, I. Park, J. Yoon et al., "Structural analysis of block copolymer thin films with grazing incidence small-angle X-ray scattering," *Macromolecules*, vol. 38, no. 10, pp. 4311–4323, 2005.
- [15] M. R. Baklanov, K. P. Mogilnikov, V. G. Polovinkin, and F. N. Dultsev, "Determination of pore size distribution in thin films by ellipsometric porosimetry," *Journal of Vacuum Science and Technology B*, vol. 18, no. 3, pp. 1385–1391, 2000.
- [16] M. H. Yoon, S. H. Lee, H. L. Park, H. K. Kim, and M. S. Jang, "Solid solubility limits of Ga and Al in ZnO," *Journal of Materials Science Letters*, vol. 21, no. 21, pp. 1703–1704, 2002.
- [17] D. Grosso, G. J. Soler-Illia, F. Babonneau et al., "Highly organized mesoporous titania thin films showing mono-oriented 2D hexagonal channels," *Advanced Materials*, vol. 13, no. 14, pp. 1085–1090, 2001.
- [18] J.-H. Lee and B.-O. Park, "Characteristics of Al-doped ZnO thin films obtained by ultrasonic spray pyrolysis: effects of Al doping and an annealing treatment," *Materials Science and Engineering B*, vol. 106, no. 3, pp. 242–245, 2004.
- [19] D. A. Doshi, A. Gibaud, V. Goletto et al., "Peering into the self-assembly of surfactant templated thin-film silica mesophases," *Journal of the American Chemical Society*, vol. 125, no. 38, pp. 11646–11655, 2003.
- [20] H.-M. Zhou, D.-Q. Yi, Z.-M. Yu, L.-R. Xiao, and J. Li, "Preparation of aluminum doped zinc oxide films and the study of their microstructure, electrical and optical properties," *Thin Solid Films*, vol. 515, no. 17, pp. 6909–6914, 2007.
- [21] S. O. Kasap, *Principles of Electronic Materials and Devices*, McGraw-Hill, New York, NY, USA, 3rd edition, 2006.

Research Article

Submicron Features in Higher Manganese Silicide

Yatir Sadia, Mor Elegrably, Oren Ben-Nun, Yossi Marciano, and Yaniv Gelbstein

Department of Materials Engineering, Ben-Gurion University of the Negev, Beer Sheva, Israel

Correspondence should be addressed to Yatir Sadia; yatttir@yahoo.com

Received 13 June 2013; Accepted 14 August 2013

Academic Editor: Jung-Kun Lee

Copyright © 2013 Yatir Sadia et al. This is an open access article distributed under the Creative Commons Attribution License, which permits unrestricted use, distribution, and reproduction in any medium, provided the original work is properly cited.

The world energy crisis had increased the demand for alternative energy sources and as such is one of the topics at the forefront of research. One way for reducing energy consumption is by thermoelectricity. Thermoelectric effects enable direct conversion of thermal into electrical energy. Higher manganese silicide (HMS, $\text{MnSi}_{1.75}$) is one of the promising materials for applications in the field of thermoelectricity. The abundance and low cost of the elements, combined with good thermoelectric properties and high mechanical and chemical stability at high temperatures, make it very attractive for thermoelectric applications. Recent studies have shown that Si-rich HMS has improved thermoelectric properties. The most interesting of which is the unusual reduction in thermal conductivity. In the current research, transmission (TEM) and scanning (SEM) electron microscopy as well as X-ray diffraction methods were applied for investigation of the govern mechanisms resulting in very low thermal conductivity values of an Si-rich HMS composition, following arc melting and hot-pressing procedures. In this paper, it is shown that there is a presence of sub-micron dislocations walls, stacking faults, and silicon and HMS precipitates inside each other apparent in the matrix, following a high temperature (0.9 Tm) hot pressing for an hour. These are not just responsible for the low thermal conductivity values observed but also indicate the ability to create complicate nano-structures that will last during the production process and possibly during the application.

1. Introduction

Recent trends in clean energy have given rise to the need for alternative energy sources. One such source is thermoelectric materials, which can utilize waste heat to increase the efficiency of devices with high heat loss. The currently available thermoelectric materials are either not abundant enough for mass production, expensive, toxic, or have too low efficiency to be attractive. The metal silicides are thermoelectric material with low production costs, made from abundant elements, nontoxic and highly stable materials both thermally and mechanically [1]. The most promising *p*-type materials in this family are the higher manganese silicides (HMS) containing several very similar phases including Mn_4Si_7 , $\text{Mn}_{11}\text{Si}_{19}$, $\text{Mn}_{15}\text{Si}_{26}$, and $\text{Mn}_{27}\text{Si}_{47}$ [2]. While HMS offers one of the few materials which in addition to good thermoelectric properties, low cost, and high abundance can also operate in atmospheric conditions [3, 4], it is yet not high enough in efficiency.

One of the most important measures to the efficiency of a thermoelectric material is the dimensionless figure of

merit (ZT) defined as the square of Seebeck coefficient times the temperature over the electric resistivity time of the thermal conductivity. While the all three transport properties are related to the carrier concentration and are therefore optimized mainly by introducing an optimal amount of charge carriers into the materials, research in the field showed [5] that ZT values can be also enhanced by increasing the structure complexity and thereby decreasing the thermal conduction by phonons without adversely affecting the charge carrier concentration.

In recent publications, a low thermal conductivity was realized for HMS samples [6]. In the current research, the influence of apparent submicro features on reduction of the thermal conductivity, following an arc melting and hot pressing, was investigated.

2. Experimental Procedures

2.1. Synthesis. The samples were all synthesized from pure silicon (7 N) and manganese (99.5%) pieces. The manganese pieces were cleaned using 50% hydrochloric acid and 50%

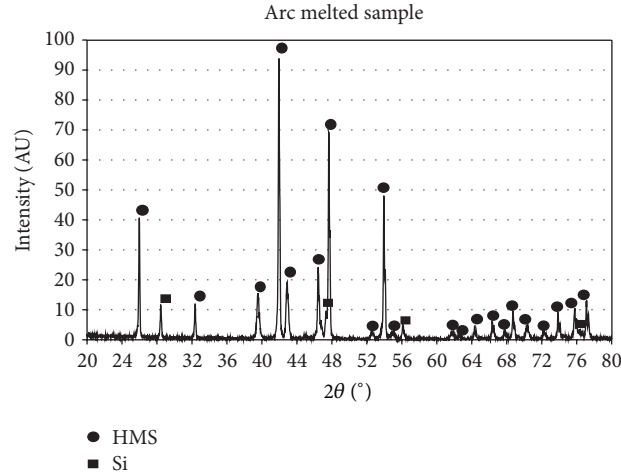


FIGURE 1: X-ray diffraction of eutectic arc melted specimen following hot pressing: ●: silicon; ■: higher manganese silicide peaks.

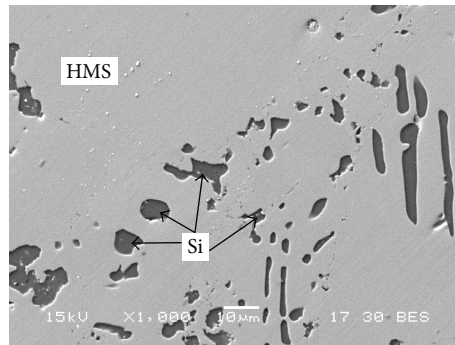


FIGURE 2: SEM micrograph following hot pressing, indicating dark silicon precipitates embedded in a light HMS matrix.

ethanol solution for 10 seconds and flushing in ethanol. The Mn and Si pieces of the eutectic composition of $\text{MnSi}_{1.91}$ were taken to an arc melting furnace and melted. The resulting ingots were crushed into a powder of $63\text{ }\mu\text{m}$ and taken to a hot-press. Hot pressing was done in a graphite die at 1000°C for 60 minutes under a mechanical pressure of 50 MPa in an argon atmosphere.

2.2. Structural Measurements. TEM specimens were prepared by cutting a 3 mm disc using EDM (electric discharge machining) and polished using TEM Minimet Polisher to $100\text{ }\mu\text{m}$. The center was polished using a dimple grinder down to a $0.25\text{ }\mu\text{m}$ alumina finish. The final preparation was done using a precision ion polishing system. Transmission electron microscopy was performed using a JEOL FasTEM-2010 electron microscope.

Scanning electron microscopy was employed for microstructural characterizations using JEOL JSM-5600.

The X-ray data were collected on a Rigaku DMAX 2100 powder diffractometer with a graphite monochromator on the diffracted beam provided by Cu K α radiation and operating at $V = 40\text{ kV}$, $I = 30\text{ mA}$.

2.3. Electronic Transport Properties. Seebeck coefficient and the electrical resistivity measurements were carried out in

a home-built apparatus up to $\sim 450^\circ\text{C}$ (and a heating rate of $3^\circ\text{C}/\text{min}$) under an Ar atmosphere. For the measurement of the Seebeck coefficient, an auxiliary heater was used to maintain a temperature difference of 10°C between the extremities of the samples. The electrical resistivity was measured by the “four-probe” method using an alternating power source of 1 V/50 Hz.

2.4. Thermal Properties. The thermal conductivity was measured from room temperature up to 500°C using the flash diffusivity method (LFA 457, Netzsch). Thermal conductivity (κ) values were calculated using the equation $\kappa = \alpha \cdot \rho \cdot C_p$, where α is the thermal diffusivity, C_p is the specific heat (measured using differential scanning calorimetry, STA 449-Netzsch), and ρ is the bulk density of the sample.

3. Results and Discussion

The XRD pattern shown in Figure 1 indicates the appearance of only the HMS phase with some Si phase remaining, agreeing with the eutectic composition selected. The SEM micrograph in Figure 2 also indicates the existence of only HMS and silicon phases, where $\sim 10\text{--}100\text{ }\mu\text{m}$ Si precipitates are embedded in the main HMS matrix.

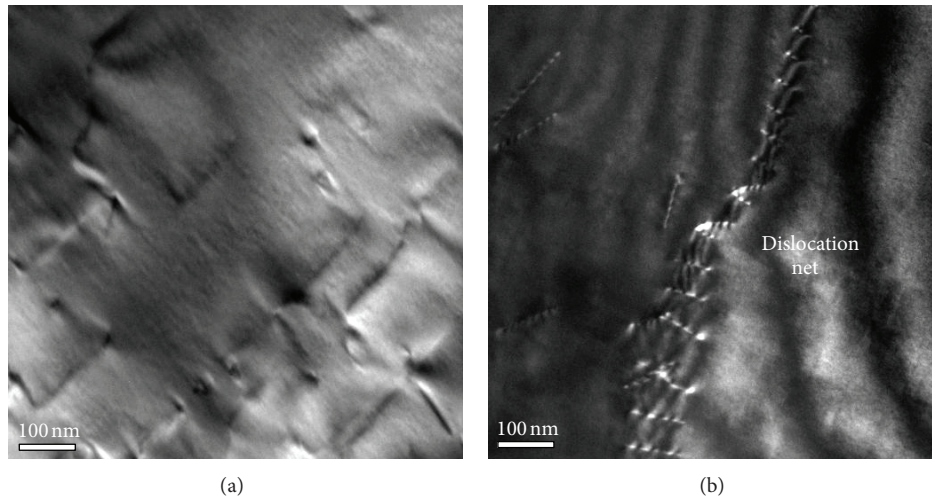


FIGURE 3: TEM images of the HMS matrix containing (a) a large number of dislocations, (b) dislocation walls.

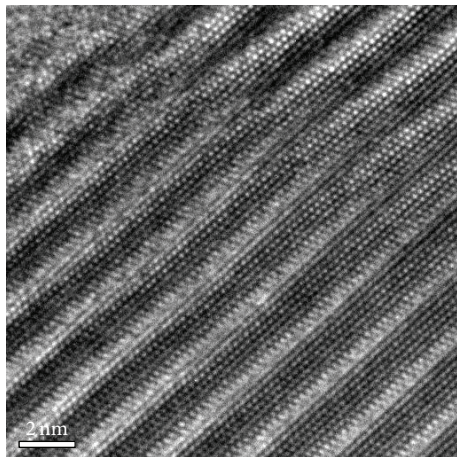


FIGURE 4: TEM lattice image of the hot pressed HMS matrix with a kink showing the fault.

Higher magnification TEM investigation (Figures 3–6) revealed only the appearance of the two types of phases, observed by XRD (Figure 1) and SEM (Figure 2), the white being Si and the dark being HMS, as were determined by both electrons diffraction and EDS. Yet, several submicron features that can act as phonon scattering centers were also observed.

In Figure 3, a large number of dislocations (Figure 3(a)) and even highly dense dislocation walls (Figure 3(b)), apparent in the HMS matrix, can be seen. Such a high dislocation density is not typical for brittle materials such as HMS, and their presence can serve as an efficient phonon scattering source. One more predominant feature can be seen in the lattice image in Figure 4. This type of deviation from the straight lattice was reported in [2] by Ye and Amelinckx. This feature is an extra silicon plane in the middle of the HMS lattice, a special type of stacking fault or dislocation which predominates in HMS.

When looking for larger defects, two main interesting phenomena were observed: submicron precipitates of Si in between the HMS grains and submicron precipitates of HMS inside silicon grains. Figure 5 illustrates two typical Si submicron precipitates between two adjacent HMS grains, one in a triple junction (Figure 5(a)) and one between two grains (Figure 5(b)). The presence of submicron precipitates following the high temperature hot-pressing procedure, at 0.9 Tm of the HMS phase, can provide evidence to the fact that, due to the low diffusion rates of the HMS phase, the submicron features can be stable at or above the working temperature (660°C in air [3, 4] and up to about 750°C in argon). This evidence is also coupled with the HMS precipitates in an Si grain that can be seen in Figure 6. In this figure, a trail of precipitates is observed (Figure 6(a)), which seems to be parallel to the grain boundary shown in Figure 6(b). This can be explained by very fine HMS powder, getting trapped between two silicon grains during the hot-pressing procedure. While the silicon has high diffusion rates in the matrix enhancing the grain boundary movement, the HMS apparently stays where the original grain boundary existed. This further supports the fact that the observed submicron features can be stable at high temperatures.

The described above submicron features in the investigated HMS sample seem to arise from the powdering process, while keeping their size after a long hot-press process. The advantage that can be gained by reducing the lattice thermal conductivity is highly dependent on the ability to retain submicron features during long operations. While very few materials can keep their original submicron features upon high temperature exposure, due to thermodynamic forces, it seems that HMS is the perfect candidate for retaining of such features.

The measured Seebeck coefficient and electrical conductivity values are shown in Figure 7. The positive Seebeck coefficients clearly indicate that the investigated composition is a *p*-type semiconductor, while the increased/decreased trend of Seebeck coefficient/electrical conductivity with increasing

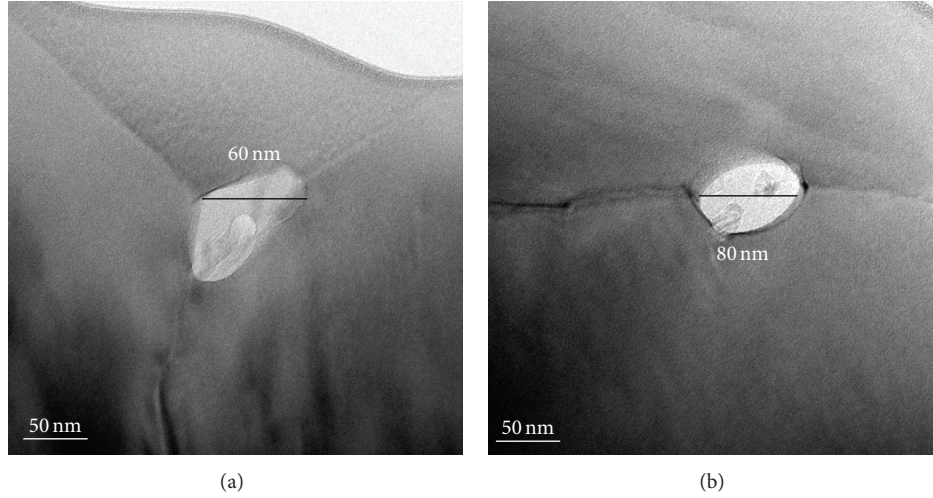
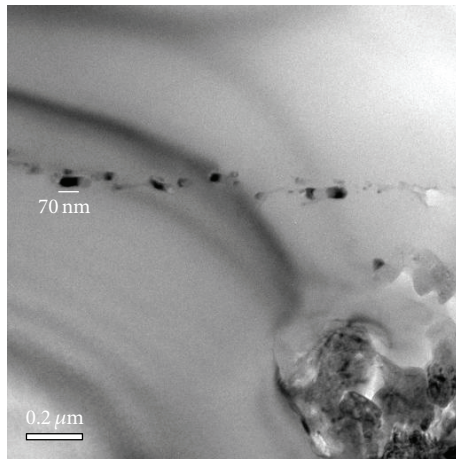
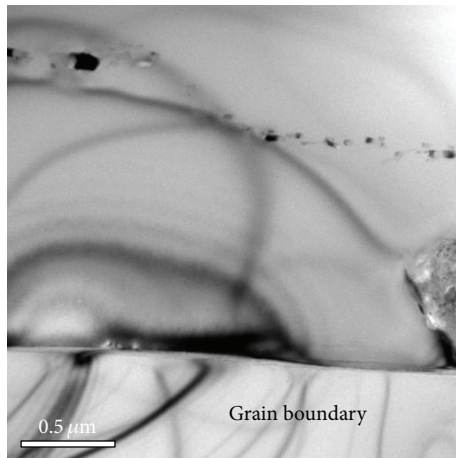


FIGURE 5: TEM images of the HMS matrix containing (a) a 60 nm silicon precipitate in a triple junction, (b) an 80 nm precipitate of silicon between two HMS grains.



(a)



(b)

FIGURE 6: TEM images of the HMS matrix containing (a) a trail of submicron grains within the silicon matrix, (b) a parallel grain boundary.

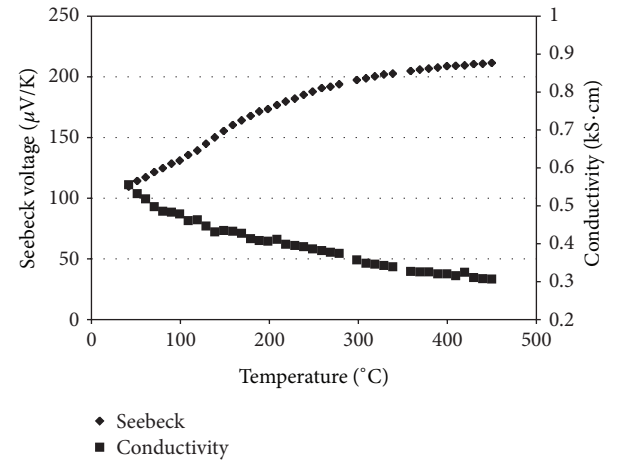


FIGURE 7: The Seebeck coefficient and the electrical conductivity values following arc melting and hot pressing.

of the temperature clearly indicates a metallic nature, highlighting the highly degenerate nature of the semiconductor. Figure 8 shows the total and lattice thermal conductivities as well as the dimensionless thermoelectric figure of merit, ZT , values obtained following arc melting and hot pressing. The electronic contribution to the thermal conductivity, κ_e , was calculated using the Wiedemann-Franz relation (1) and the measured electrical conductivity values (Figure 7). The figure shows that the phonon contribution to the thermal conductivity outweighs the electronic contribution, meaning that, even if some electron scattering occurs, it should not be highly significant:

$$\kappa_e = L\sigma T, \quad (1)$$

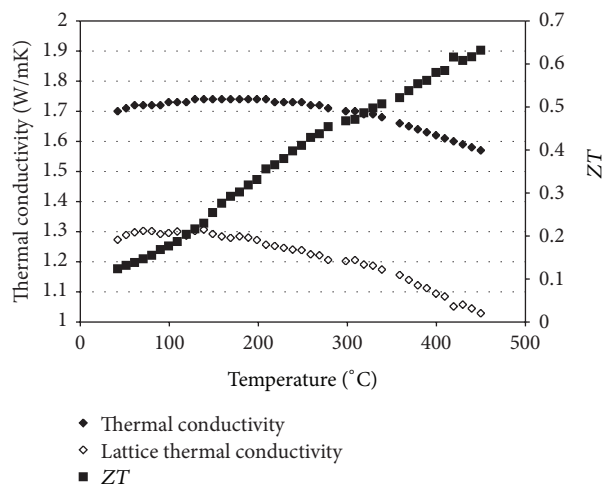


FIGURE 8: Total and lattice thermal conductivities as well as the dimensionless figure of merit, ZT , following arc melting and hot pressing.

where L and T are Lorenz numbers which in highly degenerated semiconductors are constants equal to $2.44 \cdot 10^{-8} \text{ W}\Omega\text{K}^{-2}$ and the absolute temperature, respectively. The lattice thermal conductivity shown in Figure 8 was calculated by subtracting the electronic component of the thermal conductivity from the total thermal conductivities.

It can be seen that very low lattice thermal conductivity values of $\sim 1\text{--}1.3 \text{ W/mK}$ were obtained for the investigated temperature range, which can be attributed to the submicron features observed and retained following the high temperature hot-pressing procedure (Figures 3–6), resulting in very high ZT values with a maximal value of ~ 0.63 , observed at 450°C .

4. Conclusions

Higher manganese silicide-based samples were prepared by arc melting, hand milling, and hot pressing. Of the samples TEM, SEM, and XRD specimens were prepared and examined. The specimen showed various submicron features which can contribute to the low thermal conductivity measured. These features include dislocation walls, stacking faults, and nanoclusters of both HMS inside the Si matrix and Si inside the HMS matrix. These features were retained following the hot-pressing procedure, which was performed at 0.9 of the homologues temperature of HMS, clearly indicating promise for durability of the features during long operations.

Acknowledgments

The authors would like to acknowledge Engineer A. Jarashnely for his help and expertise with XRD characterization and Dr. S. Remenik for the help and expertise with TEM characterization.

References

- [1] C. B. Vining, *CRC Handbook of Thermoelectrics*, CRC Press, Boca Raton, Fla, USA, 1995.
- [2] H. Q. Ye and S. Amelinckx, "High-resolution electron microscopic study of manganese silicides MnSi_{2-x} ," *Journal of Solid State Chemistry*, vol. 61, no. 1, pp. 8–39, 1986.
- [3] S. Okada, T. Shishido, M. Ogawa et al., "MnSi and MnSi_{2-x} single crystals growth by Ga flux method and properties," *Journal of Crystal Growth*, vol. 229, no. 1, pp. 532–536, 2001.
- [4] S. Okada, T. Shishido, Y. Ishizawa et al., "Crystal growth by molten metal flux method and properties of manganese silicides," *Journal of Alloys and Compounds*, vol. 317–318, pp. 315–319, 2001.
- [5] G. J. Snyder and E. S. Toberer, "Complex thermoelectric materials," *Nature Materials*, vol. 7, no. 2, pp. 105–114, 2008.
- [6] Y. Sadia and Y. Gelbstein, "Silicon-rich higher manganese silicides for thermoelectric applications," *Journal of Electronic Materials*, vol. 41, no. 6, pp. 1504–1508, 2012.

Research Article

Effect of Surfactant Concentration Variation on the Thermoelectric Properties of Mesoporous ZnO

Min-Hee Hong,¹ Chang-Sun Park,¹ Sangwoo Shin,² Hyung Hee Cho,² Won-Seon Seo,³ Young Soo Lim,³ Jung-Kun Lee,⁴ and Hyung-Ho Park¹

¹ Department of Materials Science and Engineering, Yonsei University, Seoul 120-749, Republic of Korea

² School of Mechanical Engineering, Yonsei University, Seoul 120-749, Republic of Korea

³ Korea Institute of Ceramic Engineering and Technology, Seoul 153-801, Republic of Korea

⁴ Department of Mechanical Engineering and Materials Science, University of Pittsburgh, Pittsburgh, PA 15261, USA

Correspondence should be addressed to Hyung-Ho Park; hypark@yonsei.ac.kr

Received 7 May 2013; Revised 10 August 2013; Accepted 22 August 2013

Academic Editor: Jin-Sang Kim

Copyright © 2013 Min-Hee Hong et al. This is an open access article distributed under the Creative Commons Attribution License, which permits unrestricted use, distribution, and reproduction in any medium, provided the original work is properly cited.

The electrical and thermal conductivities and the Seebeck coefficient of mesoporous ZnO thin films were investigated to determine the change of their thermoelectric properties by controlling surfactant concentration in the mesoporous ZnO films, because the thermoelectric properties of mesoporous ZnO films can be influenced by the porosity of the mesoporous structures, which is primarily determined by surfactant concentration in the films. Mesoporous ZnO thin films were successfully synthesized by using sol-gel and evaporation-induced self-assembly processes. Zinc acetate dihydrate and Brij-76 were used as the starting material and pore structure-forming template, respectively. The porosity of mesoporous ZnO thin films increased from 29% to 40% with increasing surfactant molar ratio. Porosity can be easily altered by controlling the molar ratio of surfactant/precursor. The electrical and thermal conductivity and Seebeck coefficients showed a close correlation with the porosity of the films, indicating that the thermoelectric properties of thin films can be changed by altering their porosity. Mesoporous ZnO thin films with the highest porosity had the best thermoelectric properties (the lowest thermal conductivity and the highest Seebeck coefficient) of the films examined.

1. Introduction

The acceleration in global warming has made development of alternative energy sources of critical importance to modern society. Among many alternative energy technologies, thermoelectric technology refers to creation of an electrical current in a material with a temperature gradient. High electrical conductivity, a high Seebeck coefficient, and low thermal conductivity are essential characteristics of thermoelectric materials. Although it is very difficult to control these factors individually, because electrical conductivity and the Seebeck coefficient have an inverse relationship, this problem can be overcome by the use of nanostructures, such as nanowires and superlattices [1].

Mesoporous structures are those with a pore diameter ranging from 2 to 50 nm [2]. Compared with nonporous structures, mesoporous structures have excellent physical and

chemical properties. Because of their pore structure, mesoporous materials have unique properties such as low thermal conductivity and high specific surface area. They can potentially be used in gas sensor applications and in thermoelectric devices, among many other applications. However, these materials should have a high Seebeck coefficient and electrical conductivity and low thermal conductivity when applied in thermoelectric devices. Although mesoporous structures have low thermal conductivity property, this is accompanied by a decrease in electrical conductivity. By controlling porosity and pore size, this limitation can be overcome. Electrical conductivity and thermal conductivity have different inelastic mean free paths from each other. The inelastic mean free path of an electron is four times longer than that of a phonon. This difference can induce the phonon-glass electron-crystal (PGEC) effect. By exploiting this effect in mesoporous structures, electrical conductivity and thermal

conductivity can be controlled separately. Furthermore, the thermoelectric properties of a material can be improved by adopting a mesoporous structure.

Zinc oxide (ZnO) is an inexpensive, n-type, wide band gap semiconductor material that has excellent electronic, optic, and photonic properties. It is, therefore, used in photovoltaic [3], gas sensor [4], and laser [5] applications, among many others. ZnO thin films can be synthesized by various techniques such as spray pyrolysis, RF sputtering, chemical vapor deposition (CVD) and sol-gel processes [6–8]. Among these methods, we adopted the sol-gel method in this study because this is a low-cost procedure and it offers easy control of film thickness and composition. However, the low crystallization temperature of ZnO and high reactivity of Zn ion precursors makes it difficult to create mesoporous ZnO [9–11]. During annealing for calcination, the pore structure can easily collapse because of crystallization of ZnO with a hexagonal wurtzite structure at low temperature. Furthermore, it is more difficult to obtain a three-dimensional network structure of ZnO because it is harder to form Zn–O bonds than Si–O or Ti–O bonds during hydrolysis because of the high reactivity of the Zn ion precursor. Low temperature annealing and stable conditions are required to address these problems. By using a block copolymer with a low molecular weight and a complex agent, mesoporous ZnO thin films can be synthesized successfully. In this paper, we investigated the effect of the molar ratio of surfactant/precursor on the formation of mesoporous ZnO thin films and the crystallization, pore structure, porosity, and thermoelectric properties of the resultant films.

2. Experimental Procedure

Mesoporous ZnO thin films were synthesized on SiO₂/Si substrates by sol-gel and spin coating processes. In this work, n-propanol, zinc acetate dihydrate [Zn(CH₃COO)₂·H₂O], and monoethanolamine (MEA) were used as the solvent, precursor and complex agent, respectively. Brij-76 (C₅₈H₁₁₈O₂₁, Aldrich, MW 711), which forms micelle structures, was used as a surfactant. MEA acts as a stabilizer in ZnO sol as well as a pH-increasing agent. Addition of MEA to ZnO sol causes the ZnO matrix to adopt a rigid structure. In this work, the molar ratio of MEA/Zn precursor was fixed at 1 to allow us to investigate the effect of the molar ratio of surfactant/precursor on the pore structure of mesoporous ZnO.

The molar ratio of zinc acetate dihydrate:Brij-76:MEA:n-propanol was 1:0.03~0.09:1:34.5. surfactant/precursor molar ratios were 0.03, 0.05, and 0.09, which we indexed as Z3*/Z3, Z5*/Z5, and Z9*/Z9 before/after the annealing process, respectively. Mesoporous ZnO thin films were prepared by spin coating this solution onto SiO₂/Si substrate through the evaporation-induced self-assembly (EISA) process [12, 13]. After coating, thin films were pre-heated at 300°C for 10 min to pyrolysis the ZnO precursor and remove residual organics. Mesoporous ZnO thin films were synthesized after annealing at 450°C for 4 h under vacuum. To analyze the mesoporous structures, small angle X-ray diffraction (SAXRD) was performed with angles ranging from 1° to 5° using CuK α radiation (1.5418 Å).

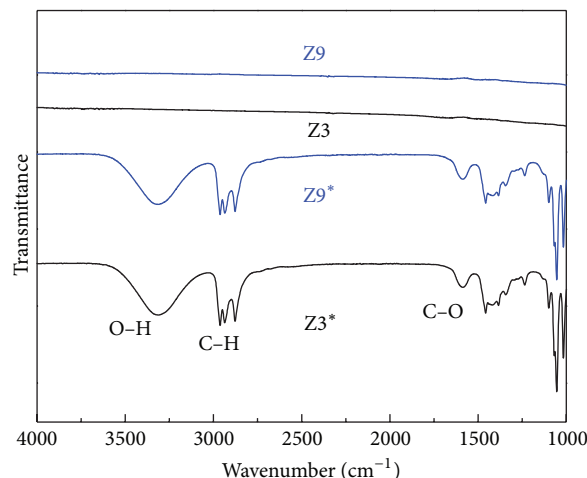


FIGURE 1: FT-IR spectra of mesoporous ZnO thin films produced using various surfactant concentrations before annealing (Z3*, Z9*) and after annealing (Z3, Z9) at 450°C.

The pore structure and ordering was analyzed by transmission electron microscope (TEM, JEOL JEM-2100F) at 400 kV. The porosity of mesoporous ZnO thin films was measured using an ellipsometer (Gatan L117C, 632.8 nm He-Ne lasers) and the Lorentz-Lorenz equation [14]. For thermal conductivity measurements of mesoporous ZnO film, the 3 ω method measurement was performed at 300 K [15]. The Seebeck coefficients and the electrical resistivity of mesoporous ZnO films were measured by detecting the Seebeck voltage and the temperature difference from 323 K to 478 K with an interval of 50 K. Hall measurement equipment was used to measure the carrier concentration of mesoporous ZnO thin films.

3. Results and Discussion

Figure 1 shows the FT-IR spectra of mesoporous ZnO thin films before and after annealing at 450°C under vacuum. Low temperature annealing was performed to prevent the collapse of the pores. Before annealing, organic bonds were observed in ZnO samples, for example, Z3* and Z9* had broad peaks at approximately 3300 cm⁻¹, 2800 cm⁻¹, and from 1400 cm⁻¹ to 1700 cm⁻¹, corresponding to O–H, C–H, and C–O absorption peaks, respectively. We attributed these organic bond peaks to the surfactant (Brij-76) and complex agent (MEA). However, after annealing at 450°C under vacuum, the organic bonds disappeared completely for both the Z3 and Z9 samples, as shown Figure 1. These results indicate that the surfactant was completely removed by annealing at the low temperature of 450°C.

Figure 2 shows the SAXRD patterns of mesoporous ZnO thin films after annealing at 450°C. The existence of diffraction peaks indicates a regular pore distribution in the thin films. Broad diffraction peaks were observed around 2.17, 2.21, and 2.23° of 2 θ for Z3, Z5, and Z9 samples, respectively; this broadness means that the mesoporous ZnO thin films did not have high pore regularity but formed a partially ordered

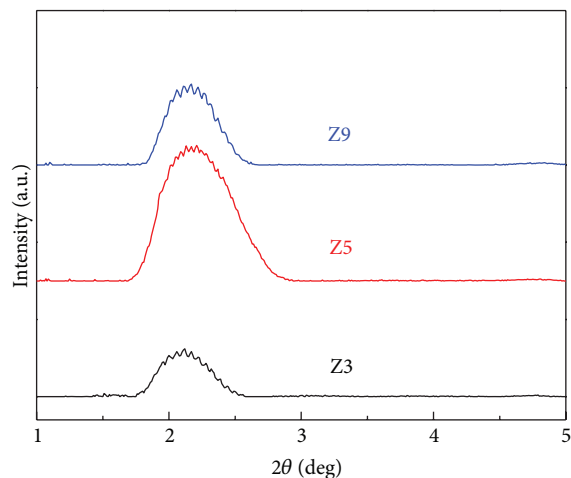


FIGURE 2: Small angle XRD patterns of mesoporous ZnO thin films synthesized using various surfactant concentrations.

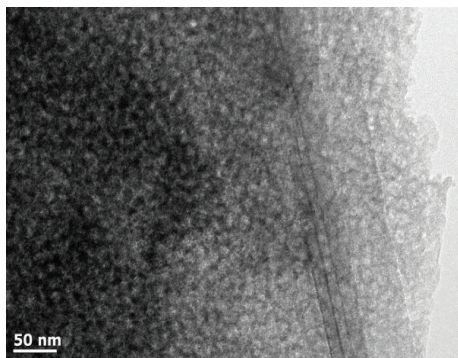


FIGURE 3: TEM image of a mesoporous ZnO thin film (Z5).

structure. From the diffraction 2θ data, the interplanar distances were calculated as 4.07, 3.99, and 3.96 nm for the Z3, Z5, and Z9 samples, respectively. These results indicate that as the surfactant molar ratio increased, so did the number of micelles per unit volume, while the thickness of the ZnO wall decreased [10]. The strongest diffraction intensity was observed for the Z5 sample; this means that the highest ordering of pores in mesoporous ZnO film was obtained at an optimized surfactant concentration. When the surfactant concentration was too low (Z3), a well-ordered micelle structure did not form because of negligible steric effects. When the surfactant concentration was too high (Z9), the regularly arranged micelle structure collapsed during calcination due to the decrease in mechanical strength with an increase in porosity. The partially ordered pore structure of Z5 could be confirmed from the TEM image, as seen in Figure 3. The image showed partially arranged, regularly spaced nanopores 8–9 nm in size, which was almost two times larger than the interplanar spacing obtained from the SAXRD data given in Figure 2. From the (200) indexation of the diffraction peak in SAXRD data and TEM data, mesoporous ZnO thin film could be suggested to have a partially ordered, body-centered cubic arrangement of pores.

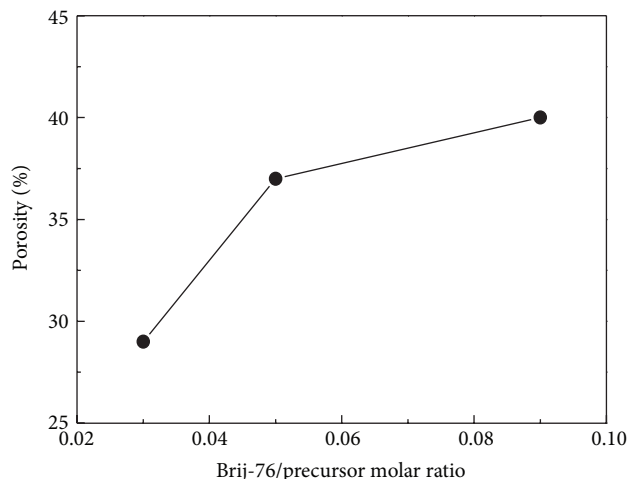


FIGURE 4: Porosity of mesoporous ZnO thin films synthesized using various surfactant concentrations.

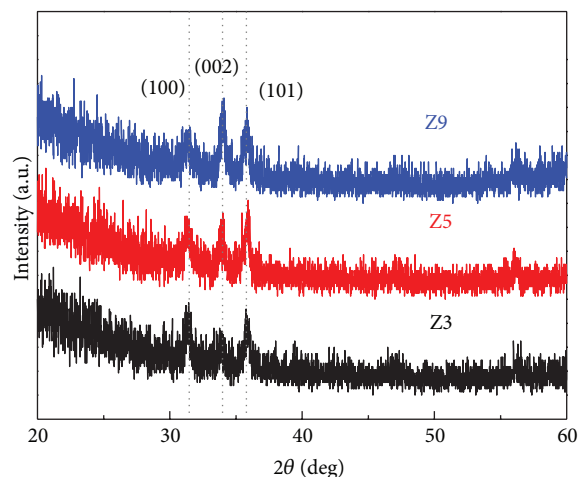


FIGURE 5: Wide-angle XRD patterns of mesoporous ZnO thin films synthesized using various surfactant concentrations.

Figure 4 shows the porosity behavior of mesoporous ZnO thin films. The porosity of the Z3, Z5, and Z9 films was measured as 29, 37, and 40%, respectively, and porosity increased with increasing surfactant molar ratio. However, in the case of the Z9 sample, the increase in porosity was small when considering the increase in the surfactant molar ratio; this was due to the collapse of pores, as shown in Figure 2.

Wide-angle XRD patterns of mesoporous ZnO thin films are shown in Figure 5. Mesoporous ZnO thin films were crystallized with a hexagonal wurtzite structure; the diffraction peaks at a 2θ of approximately 31.8° , 33.4° , and 36.2° were indexed as 100, 002, and 101, respectively. Comparison of diffraction intensity revealed that the surfactant concentration did not affect the crystallization of skeleton-structured ZnO.

Figure 6 shows the Seebeck coefficient of mesoporous ZnO thin films after annealing at 450°C at various surfactant/precursor molar ratios. Because ZnO is an n-type

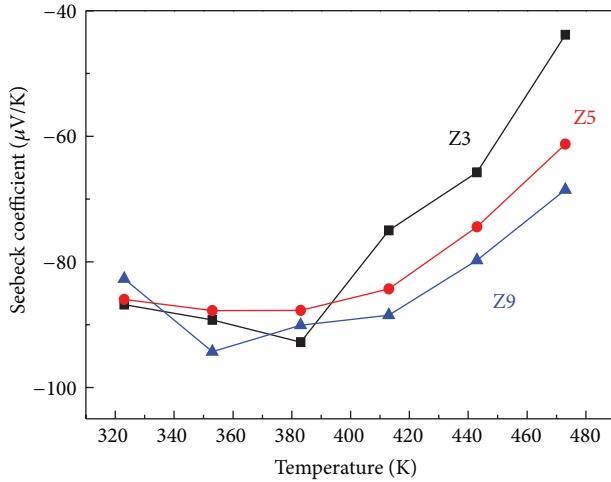


FIGURE 6: The Seebeck coefficient of mesoporous ZnO thin films synthesized using various surfactant concentrations.

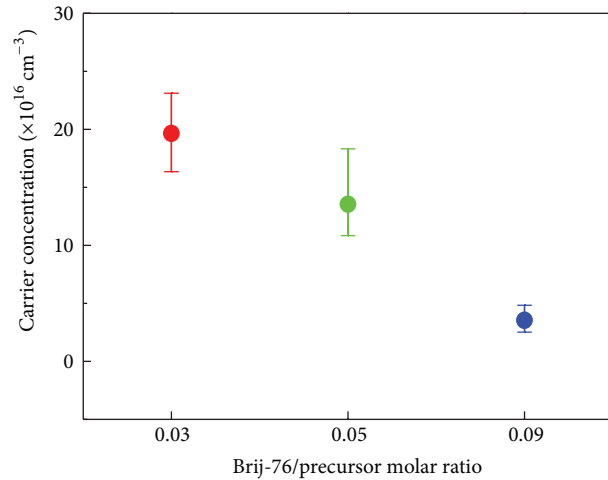


FIGURE 7: The carrier concentration of mesoporous ZnO thin films synthesized using various surfactant concentrations.

material, its Seebeck coefficient has a negative value. The Seebeck coefficient was affected by the surfactant/precursor molar ratio; when surfactant/precursor molar ratio increased, porosity also rose, inducing an increase of internal surface area which might act as a carrier trap site. The relationship between the carrier concentration and surfactant concentration was given in Figure 7. As shown in the figure, decreases in carrier concentration were observed with increasing surfactant concentration, that is, increasing porosity of the film. Thus, Seebeck coefficient was also increased due to its inverse relationship with carrier concentration. The Z9 sample, which had the highest porosity of 40% among the samples evaluated, had the highest the Seebeck coefficient at 353 K: $-94.3 \mu\text{V/K}$.

Figure 8 shows the electrical conductivity of mesoporous ZnO thin films according to surfactant concentrations. Generally, the Seebeck coefficient has an inverse relation with electrical conductivity. As porosity increases, electrons scatter

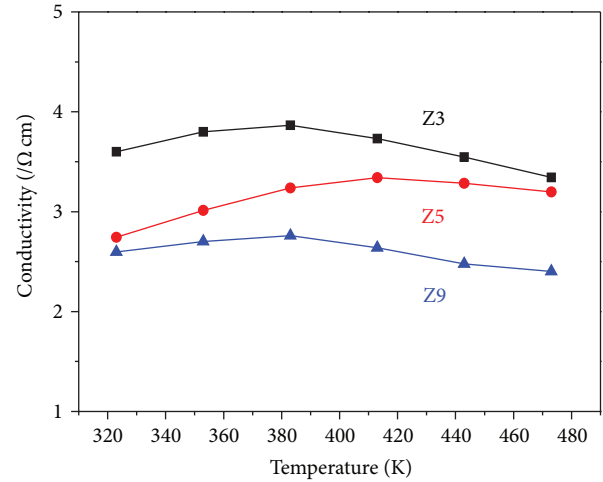


FIGURE 8: Electrical conductivity changes in mesoporous ZnO thin films synthesized using various surfactant concentrations.

and electrical conductivity decreases. Because the Z3 sample had the lowest porosity, its electrical conductivity was higher than those of the Z5 and Z9 samples. The average electrical conductivities values were 3.647 , 3.136 , and $2.596/\Omega\text{cm}$ for the Z3, Z5, and Z9 samples, respectively. Although electrical conductivity decreased with increasing surfactant concentration, the decrease in electrical conductivity was small. Furthermore, in a mesoporous structure, if the Seebeck coefficient increases and thermal conductivity decreases, then the thermoelectric properties of the structure should improve.

Thermal conductivity values of mesoporous ZnO thin films are shown in Figure 9. As the surfactant/precursor molar ratio increased, thermal conductivity decreased due to the increase in porosity. The Z9 sample had the lowest thermal conductivity of 1.01 W/mK . These results, together with the increased porosity of mesoporous ZnO film, indicate that electrical conductivity and thermal conductivity decreased concomitantly. However, thermal conductivity decreased to greater extent than electrical conductivity.

Figure 10 shows the ratio of electrical conductivity to thermal conductivity according to various surfactant concentrations because the thermoelectric figure of merit shows a direct relationship with the electrical/thermal conductivity ratio. To calculate the conductivity ratio, the electrical conductivity value was used as an average term according to temperature. As the surfactant concentration increased, the conductivity ratio also increased from 180.54 K/V^2 to 257.03 K/V^2 . This increase can be explained by the PGEC effect. With increasing porosity, the number of pores also increases, and phonons can be scattered effectively because of the pores. During this process, phonon scattering is higher than electron scattering because the phonon inelastic mean free path is generally known to be shorter than that of electrons [16]. Our conductivity ratio results indicate that the thermoelectric properties of mesoporous ZnO thin films can be enhanced by controlling their porosity. The Z9 sample had the highest conductivity ratio and the largest negative Seebeck coefficient. Therefore, by controlling the porosity of

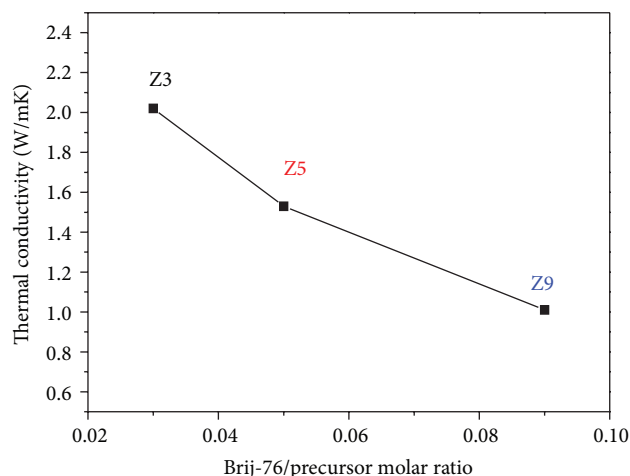


FIGURE 9: Thermal conductivity of mesoporous ZnO thin films synthesized using various surfactant concentrations.

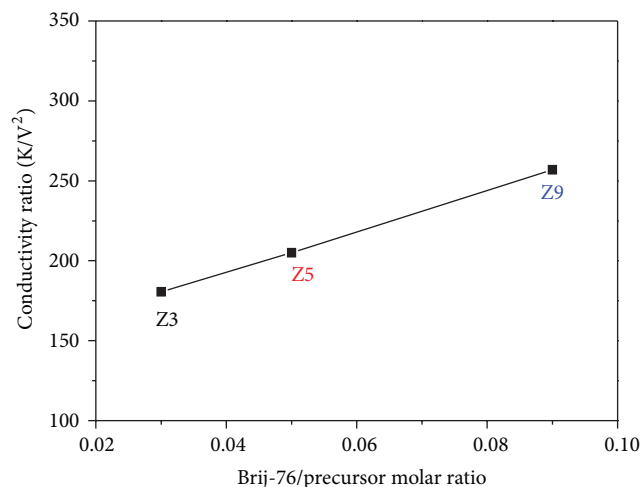


FIGURE 10: Conductivity ratio of mesoporous ZnO thin films synthesized using various surfactant concentrations.

mesoporous structures, their thermoelectric properties can be improved.

4. Conclusions

We synthesized mesoporous ZnO thin film using sol-gel and EISA processes with zinc acetate dihydrate, MEA, and Brij-76. Porosity of mesoporous ZnO thin films was varied from 29% to 40% by adjusting the precursor/surfactant molar ratio from 0.03 to 0.09. As the porosity of the thin films increased, the Seebeck coefficient was increased due to a decrease in carrier concentration. The maximum Seebeck coefficient at 353 K and the maximum electrical/thermal conductivity ratio were obtained at a surfactant/precursor molar ratio of 0.09. By increasing the porosity of the ZnO thin films, their conductivity ratio and Seebeck coefficients increased. In other words, the higher the porosity of mesoporous ZnO thin films, the better their thermoelectric properties.

Acknowledgments

This research was equally supported by the Fundamental R&D Program (Grant no. K0006007) for Core Technology of Materials funded by the Ministry of Knowledge Economy, Republic of Korea and the National Research Foundation of Korea (NRF) Grant funded by the Korean government (MEST) (no. 2012R1A2A2A01011014).

References

- [1] L. D. Hicks and M. S. Dresselhaus, "Effect of quantum-well structures on the thermoelectric figure of merit," *Physical Review B*, vol. 47, no. 19, pp. 12727–12731, 1993.
- [2] G. J. D. A. A. Soler-Illia, C. Sanchez, B. Lebeau, and J. Patarin, "Chemical strategies to design textured materials: from microporous and mesoporous oxides to nanonetworks and hierarchical structures," *Chemical Reviews*, vol. 102, no. 11, pp. 4093–4138, 2002.
- [3] Q. Zhang, C. S. Dandeneau, X. Zhou, and C. Cao, "ZnO nanostructures for dye-sensitized solar cells," *Advanced Materials*, vol. 21, no. 41, pp. 4087–4108, 2009.
- [4] H. Ra, K. Choi, J. Kim, Y. Hahn, and Y. Im, "Fabrication of ZnO nanowires using nanoscale spacer lithography for gas sensors," *Small*, vol. 4, no. 8, pp. 1105–1109, 2008.
- [5] L. Znaidi, G. J. A. A. Soler Illia, S. Benyahia, C. Sanchez, and A. V. Kanaev, "Oriented ZnO thin films synthesis by sol-gel process for laser application," *Thin Solid Films*, vol. 428, no. 1-2, pp. 257–262, 2003.
- [6] Y. Natsume and H. Sakata, "Zinc oxide films prepared by sol-gel spin-coating," *Thin Solid Films*, vol. 372, no. 1, pp. 30–36, 2000.
- [7] M. Smirnov, C. Baban, and G. I. Rusu, "Structural and optical characteristics of spin-coated ZnO thin films," *Applied Surface Science*, vol. 256, no. 8, pp. 2405–2408, 2010.
- [8] T. Sahoo, M. Kim, M. Lee et al., "Nanocrystalline ZnO thin films by spin coating-pyrolysis method," *Journal of Alloys and Compounds*, vol. 491, no. 1-2, pp. 308–313, 2010.
- [9] X. Zi-qiang, D. Hong, L. Yan, and C. Hang, "Al-doping effects on structure, electrical and optical properties of c-axis-orientated ZnO:Al thin films," *Materials Science in Semiconductor Processing*, vol. 9, no. 1-3, pp. 132–135, 2006.
- [10] G. J. D. A. A. Soler-Illia, C. Sanchez, B. Lebeau, and J. Patarin, "Chemical strategies to design textured materials: from microporous and mesoporous oxides to nanonetworks and hierarchical structures," *Chemical Reviews*, vol. 102, no. 11, pp. 4093–4138, 2002.
- [11] P. Yang, D. Zhao, D. I. Margolese, B. F. Chmelka, and G. D. Stucky, "Block copolymer templating syntheses of mesoporous metal oxides with large ordering lengths and semicrystalline framework," *Chemistry of Materials*, vol. 11, no. 10, pp. 2813–2826, 1999.
- [12] C. J. Brinker, Y. Lu, A. Sellinger, and H. Fan, "Evaporation-induced self-assembly: nanostructures made easy," *Advanced Materials*, vol. 11, no. 7, pp. 579–585, 1999.
- [13] D. Grosso, F. Cagnol, G. J. D. A. A. Soler-Illia et al., "Fundamentals of mesostructuring through evaporation-induced self-assembly," *Advanced Functional Materials*, vol. 14, no. 4, pp. 309–322, 2004.
- [14] M. R. Baklanov, K. P. Mogilnikov, V. G. Polovinkin, and F. N. Dultsev, "Determination of pore size distribution in thin films

- by ellipsometric porosimetry,” *Journal of Vacuum Science and Technology B*, vol. 18, no. 3, pp. 1385–1391, 2000.
- [15] B. Tsui, C. Yang, and K. Fang, “Anisotropic thermal conductivity of nanoporous silica film,” *IEEE Transactions on Electron Devices*, vol. 51, no. 1, pp. 20–27, 2004.
- [16] D. M. Rowe, *CRC Handbook of Thermoelectrics*, CRC Press, New York, NY, USA, 1995.

Research Article

Electronic and Thermal Transport Properties of Complex Structured Cu-Bi-Se Thermoelectric Compound with Low Lattice Thermal Conductivity

Jae-Yeol Hwang,¹ Hyeona Mun,² Jung Young Cho,³ Sang Sun Yang,⁴
Kyu Hyoung Lee,³ and Sung Wng Kim^{1,2}

¹ Center for Integrated Nanostructure Physics, Institute for Basic Science (IBS), Daejeon 305-701, Republic of Korea

² Department of Energy Science, Department of Physics, Sungkyunkwan University, Suwon 440-746, Republic of Korea

³ Materials R&D Center, Samsung Advanced Institute of Technology, Samsung Electronics, Yongin 446-712, Republic of Korea

⁴ Powder and Ceramics Division, Powder Technology Department, Korea Institute of Materials Science, Changwon 642-831, Republic of Korea

Correspondence should be addressed to Kyu Hyoung Lee; kyuhyoung.lee@samsung.com
and Sung Wng Kim; kimsungwng@skku.edu

Received 22 June 2013; Revised 20 July 2013; Accepted 5 August 2013

Academic Editor: Hyung-Ho Park

Copyright © 2013 Jae-Yeol Hwang et al. This is an open access article distributed under the Creative Commons Attribution License, which permits unrestricted use, distribution, and reproduction in any medium, provided the original work is properly cited.

Monoclinic $\text{Cu}_{x+y}\text{Bi}_{5-y}\text{Se}_8$ structure has multiple disorders, such as randomly distributed substitutional and interstitial disorders by Cu as well as asymmetrical disorders by Se. Herein, we report the correlation of electronic and thermal properties with the structural complexities of $\text{Cu}_{x+y}\text{Bi}_{5-y}\text{Se}_8$. It is found that the interstitial Cu site plays an important role not only to increase the electrical conductivity due to the generation of electron carriers but also to reduce the thermal conductivity mainly due to the phonon scattering by mass fluctuation. With impurity doping at the interstitial Cu site, an extremely low lattice thermal conductivity of $0.32 \text{ W} \cdot \text{m}^{-1} \cdot \text{K}^{-1}$ was achieved at 560 K. These synergetic effects result in the enhanced dimensionless figure of merit (ZT).

1. Introduction

In thermoelectric (TE) materials, thermal energy is directly converted into electrical energy and vice versa through the flow of charge carriers (electrons or holes) in solid state without any moving parts [1, 2]. The performance of TE device depends on the temperature gradient (ΔT) and the dimensionless figure of merit (ZT) in TE material. The conversion efficiency of TE material is governed by ZT , which is defined as $ZT = S^2 \cdot \sigma \cdot T / \kappa$, where S is the thermopower (Seebeck coefficient), σ is the electrical conductivity, κ is the thermal conductivity, and T is the absolute temperature. Intuitively, good TE materials should have sufficiently large S , high σ , and low κ . Based on this relation, there are two different kinds of straightforward strategies for achieving high ZT . The first one is maximizing power factor ($\text{PF} = S^2 \cdot \sigma$) by the modification of the electronic states through the optimization of doping, introduction of nanoscale materials, and

so forth. The other one is minimizing κ by the perturbation of structural arrangements for enhancing phonon scattering through solid-solution alloying [3–6], nanostructuring [7, 8], and the development of new materials with intrinsically low κ . However, since σ , S , and κ are the functions of charge carriers as well as these physical parameters are intercorrelated to each other, it is very difficult to control these parameters individually. Recent TE researches have been mainly focused on breaking the trade-off relationship between σ and κ by reducing the lattice thermal conductivity (κ_{latt}) due to the relative easiness of reducing κ_{latt} without considerably affecting other electronic transport parameters (S and σ). Thus, extensive researches have been focused on reducing κ_{latt} by utilizing nanostructures and compositional inhomogeneities of state-of-the-art TE materials such as Bi_2Te_3 , PbTe , and SiGe [3–8]. It has been reported that dramatically reduced κ_{latt} in TE materials is due to one of

the following mechanisms: alloy scattering [3–6], resonant scattering [9–13], anharmonic scattering [14], and interface scattering of phonons [15–17] or their combination.

Recently, much effort has been focused on discovering new semiconducting materials with intrinsically low κ_{latt} . Such materials have a solid potential compared to conventional TE materials because their κ_{latt} can be further reduced by compositional and microstructural engineering without sacrificing the other electronic properties. The common structural characteristics of low κ_{latt} materials are complex structures, which have relatively large unit cells, sublattice disorders, low crystal symmetry, and/or a variety of atom types combined with random distributions. These result in the effective phonon scatterings, which make these materials promising candidates for TE applications.

By understanding the origin of low κ in complex structured system, it is possible to find a clue for novel TE materials with an appropriate structure and to manipulate structural arrangement for the achievement of low κ in conventional TE materials. In a previous article [18], we reported new TE materials, which are the pavonite homologues $\text{Cu}_{x+y}\text{Bi}_{5-y}\text{Se}_8$ ($1.2 \leq x \leq 1.5$, $0.1 \leq y \leq 0.4$) with low κ_{latt} ($0.41\text{--}0.55 \text{ W}\cdot\text{m}^{-1}\cdot\text{K}^{-1}$ at 300 K) owing to the structural complexity. In the present study, we investigated the electronic and thermal transport properties in the view point of the correlation with crystal structure in order to clarify the origin of TE properties in the homologous $\text{Cu}_{x+y}\text{Bi}_{5-y}\text{Se}_8$ compounds.

2. Experimental

Crystal ingots of $\text{Cu}_{x+y}\text{Bi}_{5-y}\text{Se}_8$ compounds were fabricated by conventional melting technique by the use of high-purity elemental Cu (99.999%, CERAC), Bi (99.999%, 5N Plus), and Se (99.9%, 5N Plus) as starting materials. The stoichiometric mixtures of the elements were loaded into a quartz tube of 14 mm in diameter. The tube was vacuum-sealed and the mixed contents were melted in a furnace for 10 hrs at 1273 K; then, they were water quenched. The ingots were ground using ball mill, and compacted bulk samples of 10 mm in diameter and 13 mm in thickness were prepared using spark plasma sintering (SPS) technique under dynamic vacuum and with the application of 50 MPa of uniaxial pressure at 663 K. The relative densities of the resulting consolidated samples were found to range from 7.22 to $7.48 \text{ g}\cdot\text{cm}^{-3}$, which are more than 95% of the theoretical value. We used $\text{Cu}_{1.7}\text{Bi}_{4.7}\text{Se}_8$ ($\text{Cu}_{x+y}\text{Bi}_{5-y}\text{Se}_8$, $x = 1.4$, $y = 0.3$) as a reference material, and small amount (w and $z = 0.0085$ and 0.025 for the interstitial and substitutional M sites, resp.) of Zn or In was introduced in host $\text{Cu}_{1.7-w}\text{M}_w\text{Bi}_{4.7}\text{Se}_8$ or $\text{Cu}_{1.7}\text{Bi}_{4.7-z}\text{M}_z\text{Se}_8$ matrix to elucidate the electronic and thermal properties according to the different carrier concentrations. The electronic transport properties including σ and S were measured from 300 K to 560 K using an ULVAC ZEM-3 system. The κ values ($\kappa = \rho_s \cdot C_p \cdot \lambda$) were calculated from measurements taken separately: sample density (ρ_s), heat capacity (C_p), and thermal diffusivity (λ) measured under vacuum by laser-flash method (TC-9000, ULVAC, Japan), in which C_p was used as the constant value

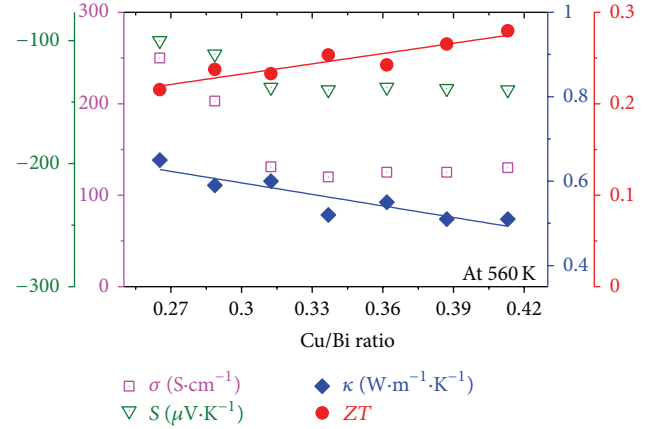


FIGURE 1: Electrical conductivity (σ), Seebeck coefficient (S), thermal conductivity (κ), and ZT as functions of Cu/Bi ratio in $\text{Cu}_{x+y}\text{Bi}_{5-y}\text{Se}_8$ ($1.2 \leq x \leq 1.5$, $0.1 \leq y \leq 0.4$) pavonite homologues. All data were acquired at 560 K.

of $0.225 \text{ J}\cdot\text{g}^{-1}\cdot\text{K}^{-1}$ estimated from the Dulong-Petit fitting using low temperature C_p data. All measured data, which were acquired at the same dimension and configuration, are obtained within the experimental error of about 5%.

3. Results and Discussions

Figure 1 shows TE properties for the homologous $\text{Cu}_{x+y}\text{Bi}_{5-y}\text{Se}_8$ ($1.2 \leq x \leq 1.5$, $0.1 \leq y \leq 0.4$) system at 560 K with varying compositional ratio between Cu and Bi. The absolute value of S decreases linearly with increasing σ , indicating that the semiconducting transport properties do not significantly change with varying the Cu/Bi ratio. Based on theoretical calculations of the previous report, interstitial Cu is regarded as the main source of electron carriers in the $\text{Cu}_{x+y}\text{Bi}_{5-y}\text{Se}_8$ system [18]. Because the electron distributions around interstitial Cu ions, which are shown in the crystal structure of Cu-Bi-Se pavonite compound (Figure 2(a)), overlapped each other along b -axis, the degree of overlapping depends on the content of the interstitial Cu. This might be a possible reason for the changes in electrical properties by perturbing Cu sites, since the interstitial Cu sites locate along b -axis and work as an electrical conduction path, leading to an improvement of electron transfer across the basal plane. On the other hand, κ decreases from 0.65 to $0.51 \text{ W}\cdot\text{m}^{-1}\cdot\text{K}^{-1}$ by increasing Cu content. The highest ZT value of 0.27 at 560 K was obtained in the $\text{Cu}_{1.9}\text{Bi}_{4.6}\text{Se}_8$ composition, which has the highest Cu concentration among samples, mainly due to its low κ . Thus, it is suggested that statistically distributed interstitial Cu along b -axis may be the main factor affecting the electronic (by generating electron carriers) and thermal transport (by enhancing phonon scattering) properties in this system. In order to understand the TE transport behavior based on the roles of the interstitial Cu and substitutional Bi sites, we individually modified those sites by impurity doping.

$\text{Cu}_{1.7}\text{Bi}_{4.7}\text{Se}_8$ was chosen as a base composition for doping, since this composition showed stable structure

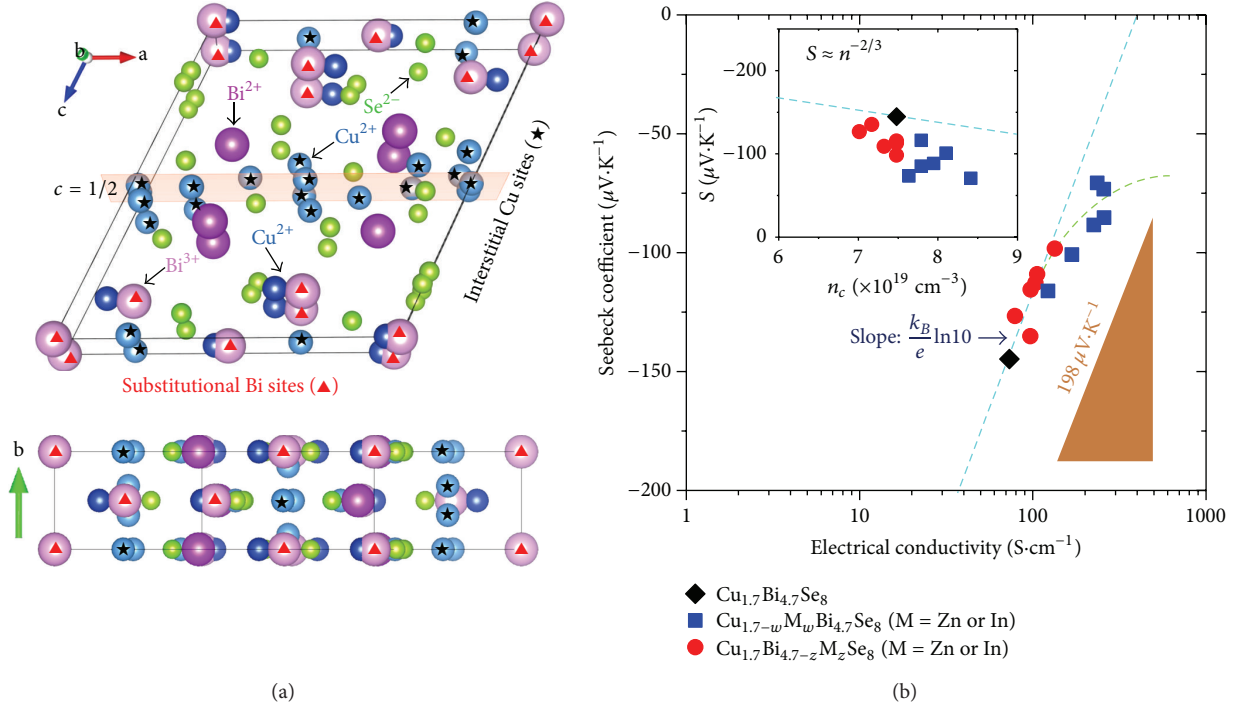


FIGURE 2: (a) Crystal structure of $\text{Cu}_{1.7}\text{Bi}_{4.7}\text{Se}_8$ with interstitial Cu and substitutional Bi sites. (b) Seebeck coefficient as a function of electrical conductivity (σ) for Cu-Bi-Se system. Blue and red dots indicate $\text{Cu}_{1.7-w}\text{M}_w\text{Bi}_{4.7}\text{Se}_8$ and $\text{Cu}_{1.7}\text{Bi}_{4.7-z}\text{M}_z\text{Se}_8$ systems, respectively. Black dot is a base $\text{Cu}_{1.7}\text{Bi}_{4.7}\text{Se}_8$ compound. The inset is Pisarenko plot at 300 K, representing the Seebeck coefficient (S) as a function of carrier concentration (n_c). The dashed line corresponds to the theoretically expected curve for $\text{Cu}_{1.7}\text{Bi}_{4.7}\text{Se}_8$ with effective mass of $m^* \sim 0.21m_0$.

and reproducible physical properties. Figure 2(b) shows the Jonker plot of Cu-Bi-Se system. Most of the experimental data points for $\text{Cu}_{1.7}\text{Bi}_{4.7-z}\text{M}_z\text{Se}_8$ compounds lie on the straight line (cyan dashed) with the slope of $198 \mu\text{V}\cdot\text{K}^{-1}$. However, in case of the interstitial Cu site modified $\text{Cu}_{1.7-w}\text{M}_w\text{Bi}_{4.7}\text{Se}_8$ compounds, the slope (green dashed line) was changed in the region of largely increased σ (Figure 2(b)), indicating that the electronic state was altered to a highly degenerate state by doping at the interstitial Cu sites. In Pisarenko plot (the inset of Figure 2(b)), all data points lie below the theoretically expected Pisarenko curve (cyan) for undoped $\text{Cu}_{1.7}\text{Bi}_{4.7}\text{Se}_8$ with effective mass of $m^* (\sim 0.21m_0)$. These electronic transport properties might be related to the changes in the Hall mobility (μ_H) and m^* of doped compounds. In order to clarify the origin for affecting S in doped compounds, m^* values were calculated using the measured S and the carrier concentration (n_c) for the whole samples. The m^* is one of the critical factors determining S and estimated with the following equation:

$$m^* = \frac{h^2}{2k_B T} \left[\frac{n_c}{4\pi F_{1/2}(\eta)} \right]^{2/3}, \quad (1)$$

where h , k_B , F_n , and η are the Planck constant, Boltzmann constant, n th order Fermi integral, and the reduced Fermi energy, respectively.

As shown in Figure 3, m^* was decreased by the doping compared to that of undoped compound. It should be noted that m^* values of the interstitial Cu site modified

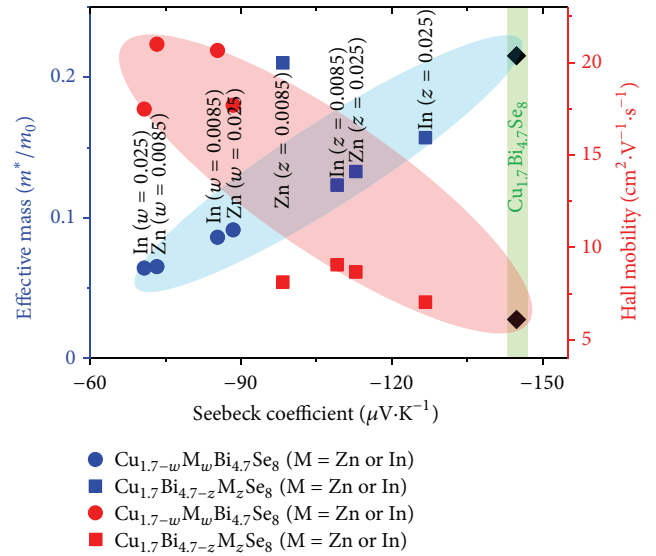


FIGURE 3: Effective mass (m^*/m_0) and Hall mobility (μ_H) as functions of Seebeck coefficient (S) for $\text{Cu}_{1.7-w}\text{M}_w\text{Bi}_{4.7}\text{Se}_8$ and $\text{Cu}_{1.7}\text{Bi}_{4.7-z}\text{M}_z\text{Se}_8$ with varying doping levels and dopants.

$\text{Cu}_{1.7-w}\text{M}_w\text{Bi}_{4.7}\text{Se}_8$ compounds were much lower than those of $\text{Cu}_{1.7}\text{Bi}_{4.7-z}\text{M}_z\text{Se}_8$. Furthermore, μ_H was inversely proportional to m^* due to the reduced mass. In principle, the reduced m^* enables the energetic movement of charge carriers in the highly degenerate semiconductors, resulting

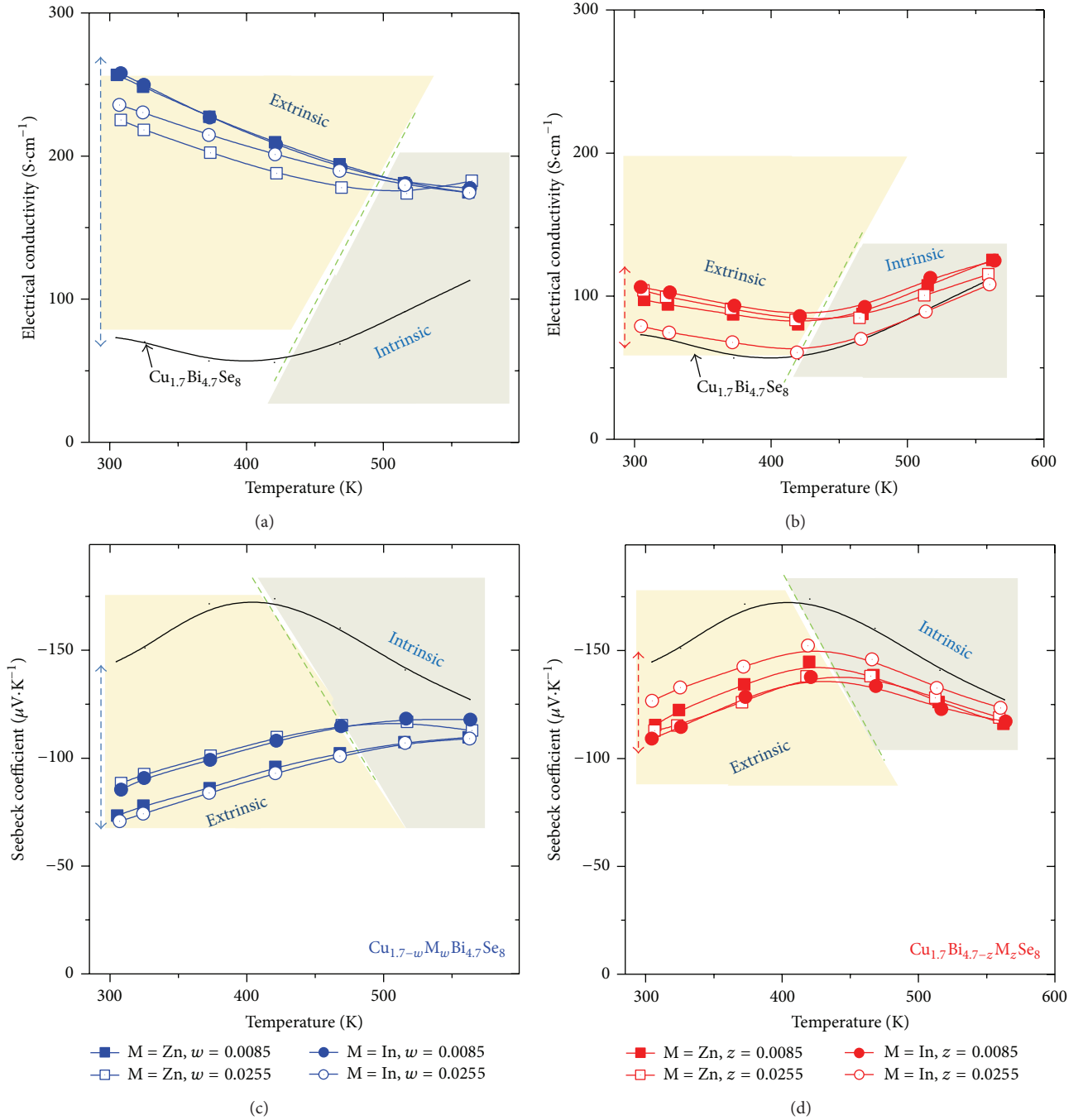


FIGURE 4: Electrical conductivity (σ) as a function of temperature for (a) $\text{Cu}_{1.7-w}\text{M}_w\text{Bi}_{4.7}\text{Se}_8$ and (b) $\text{Cu}_{1.7}\text{Bi}_{4.7-z}\text{M}_z\text{Se}_8$. Seebeck coefficient (S) as a function of temperature for (c) $\text{Cu}_{1.7-w}\text{M}_w\text{Bi}_{4.7}\text{Se}_8$ and (d) $\text{Cu}_{1.7}\text{Bi}_{4.7-z}\text{M}_z\text{Se}_8$.

in the decrease of S . Considering the slight change of n_c in the inset of Figure 2(b), it is concluded that the decrease in S is largely affected by the reduced m^* via the modification of interstitial Cu site.

In Figure 4(a), σ of $\text{Cu}_{1.7-w}\text{M}_w\text{Bi}_{4.7}\text{Se}_8$ was drastically changed by the modification of Cu sites compared to that of Bi sites ($\text{Cu}_{1.7}\text{Bi}_{4.7-z}\text{M}_z\text{Se}_8$). According to the theoretical calculation, interstitial Cu generates electron carriers in $\text{Cu}_{x+y}\text{Bi}_{5-y}\text{Se}_8$ system [18]. Therefore, more electrons can be

generated by the elemental doping at the interstitial Cu site. Indeed, higher n_c , μ_H , and the smaller m^* were observed in $\text{Cu}_{1.7-w}\text{M}_w\text{Bi}_{4.7}\text{Se}_8$ compared to those of $\text{Cu}_{1.7}\text{Bi}_{4.7-z}\text{M}_z\text{Se}_8$. In Figures 4(a) and 4(b), with increasing the doping level, the region of intrinsic conduction also shifts to higher temperatures. This is a typical behavior of a degenerate semiconductor, since the increased extrinsic majority carriers suppress the contribution of the minority carriers and hence increase the onset temperature of intrinsic conduction.

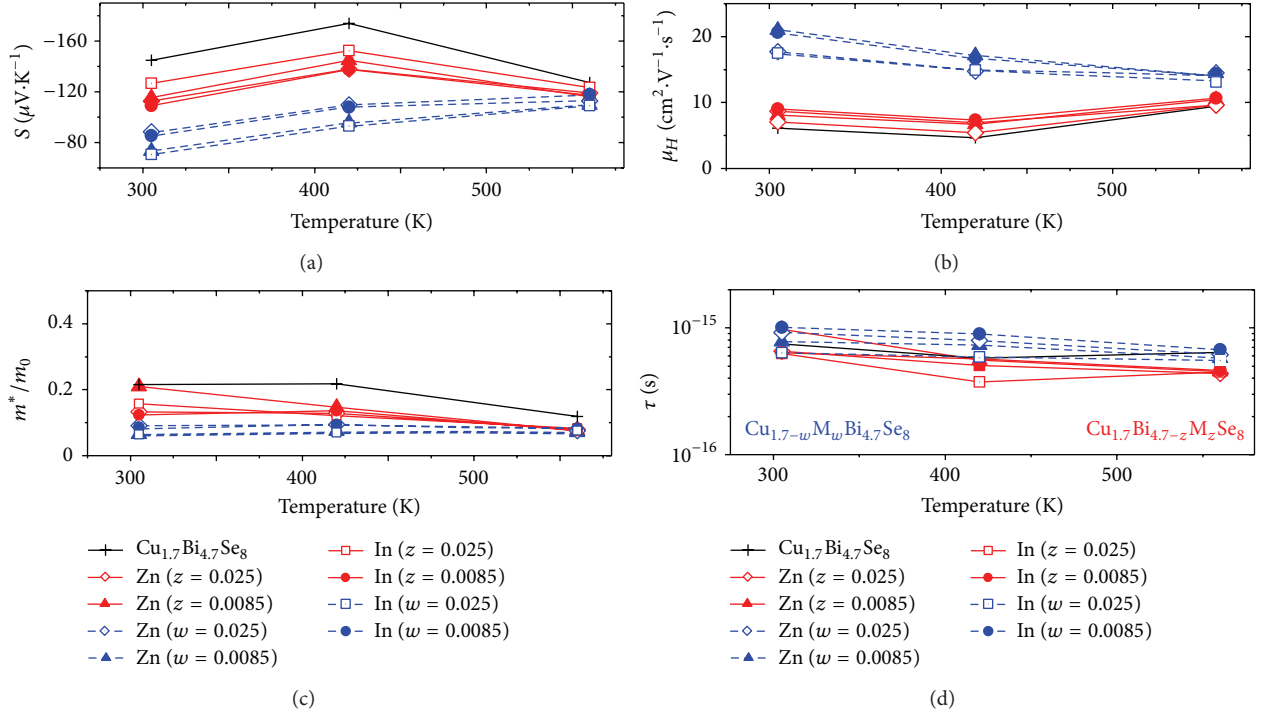


FIGURE 5: (a) Seebeck coefficient (S), (b) Hall mobility (μ_H), (c) effective mass (m^*/m_0), and (d) carrier relaxation time (τ) as a function of temperature for $\text{Cu}_{1.7-w}\text{M}_w\text{Bi}_{4.7}\text{Se}_8$ and $\text{Cu}_{1.7}\text{Bi}_{4.7-z}\text{M}_z\text{Se}_8$ with varying doping levels and dopants.

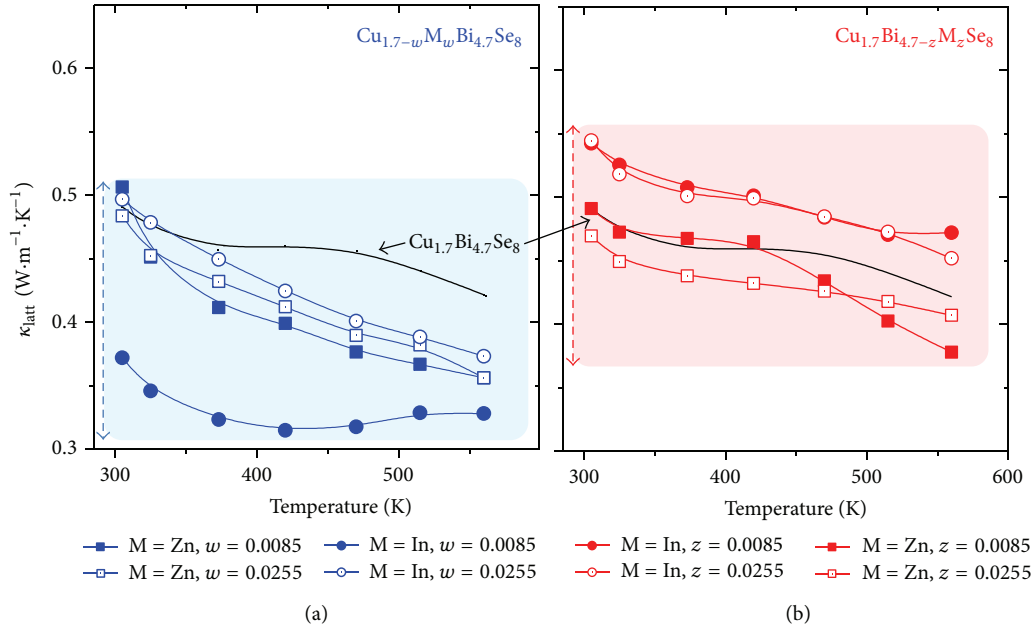


FIGURE 6: Lattice thermal conductivity (κ_{latt}) as a function of temperature for (a) $\text{Cu}_{1.7-w}\text{M}_w\text{Bi}_{4.7}\text{Se}_8$ and (b) $\text{Cu}_{1.7}\text{Bi}_{4.7-z}\text{M}_z\text{Se}_8$ with varying doping levels and dopants.

As shown in Figures 4(c) and 4(d), negative S values for all samples were observed over the entire temperature range, suggesting that the electrical conduction was dominated by n -type carriers. In Figure 5, it was confirmed that the change in S at 560 K was due to the combined effect of decreased m^*

and increased μ_H . Regardless of doping level and sites, carrier relaxation time (τ) was nearly the same (a few femtoseconds) for all samples. Figure 6 shows κ_{latt} as a function of temperature. The value of κ_{latt} was calculated from the relation of $\kappa = \kappa_{\text{latt}} + \kappa_{\text{elec}}$, in which κ_{elec} is the electronic contribution.

The value of κ_{elec} was estimated using the Wiedemann-Franz law, $\kappa_{\text{elec}} = L \cdot T \cdot \sigma$, in which L denotes the Lorenz number, taken to be $L = (\pi^2/3)(k_B/e)^2 \sim 2.45 \times 10^{-8} \text{ V}^2 \cdot \text{K}^{-2}$. However, this value is valid for the estimation of κ_{latt} in metals, not in heavily doped semiconductors like TE materials especially at high temperature. In semiconductors, the L depends on η and scattering factor (r), which can be derived from the temperature dependence of μ_H ($\mu_H \propto T^{-(3/2)+r}$) and decreases as η decreases with increasing temperature. The L is given as

$$L = \left(\frac{k_B}{e} \right)^2 \left(\frac{(r + 7/2) F_{r+(5/2)}(\eta)}{(r + 3/2) F_{r+(1/2)}(\eta)} - \left[\frac{(r + (5/2)) F_{r+(3/2)}(\eta)}{(r + (3/2)) F_{r+(1/2)}(\eta)} \right]^2 \right), \quad (2)$$

where $F_n(\eta)$ is the n th order Fermi integral, $F_n(\eta) = \int_0^\infty (x^n/(1 + e^{x-\eta})) dx$ [19].

Calculated L was nearly constant in all compounds and was in the range of $2.48\text{--}2.58 \times 10^{-8} \text{ V}^2 \cdot \text{K}^{-2}$. As shown in Figure 6, κ_{latt} was much decreased by the modification of Cu sites compared to that of Bi sites. This is mainly ascribed to the mass difference between site ions (Cu or Bi) and dopants. Indeed, the mass difference for interstitial Cu and In is 114.82 compared to 29.2 for the substitutional Bi and In. The values of κ , ranging from $0.47 \text{ W} \cdot \text{m}^{-1} \cdot \text{K}^{-1}$ to $0.69 \text{ W} \cdot \text{m}^{-1} \cdot \text{K}^{-1}$, were found for all compounds, and κ showed a weak temperature dependence. These κ values are much lower than those of state-of-the-art low κ_{latt} systems, such as Zn_4Sb_3 ($\kappa \sim 1.05 \text{ W} \cdot \text{m}^{-1} \cdot \text{K}^{-1}$ at 300 K) [20] and Cu_{2-x}Se ($\kappa \sim 1 \text{ W} \cdot \text{m}^{-1} \cdot \text{K}^{-1}$ at 400 K) [21]. We suggest that the reason of the extremely low κ values in this system is due to the strong phonon scattering and the short phonon mean free path of below 1 nm, which is much shorter than the size of unit cell of this structure. The strong phonon scattering is mainly attributed to the structural complexities based on the combined effect of point defects and intrinsic disorders. The maximum ZT values achieved in this study for Cu site and Bi site modified $\text{Cu}_{1.6915}\text{In}_{0.0085}\text{Bi}_{4.7}\text{Se}_8$ and $\text{Cu}_{1.7}\text{Bi}_{4.6915}\text{Zn}_{0.0085}\text{Se}_8$ were 0.25 and 0.18 at 560 K, respectively. It is expected from the low σ values of Cu-Bi-Se system that the present TE properties can be much enhanced by optimizing PF through tuning n_c . The modification of Cu site is an effective way to reduce κ_{latt} compared to that of Bi site. It is worth noting that intrinsically low κ of this material is less sensitive to temperature gradient because of the complex mixture of extraordinary structural disorders. There is still remaining a possibility for the further improvement of TE performance by the optimization of resonant level doping to enhance PF without sacrificing κ .

4. Conclusions

The electronic and thermal transport properties of $\text{Cu}_{1.7}\text{Bi}_{4.7}\text{Se}_8$ pavonite homologues ($N = 3$) with monoclinic $C2/m$ space group were investigated in the view point of the correlation with complex crystal structure via the modification of Cu or Bi sites with dopants. σ and κ_{latt} were

much affected by the modification of Cu sites compared to that of Bi sites. This is due to the origin of n -type conduction and the intrinsically low κ_{latt} , which is highly related to the structural configuration of the interstitial Cu sites in this system. Though the $\text{Cu}_{1.7}\text{Bi}_{4.7}\text{Se}_8$ compound showed an extremely low κ_{latt} , additional $\sim 30\%$ reduction in κ_{latt} was achieved by the modification of Cu sites. Therefore, we anticipate that the further fine-tuning of the electronic and thermal properties based on the correlated findings about structural modifications gives a possible enhancement of TE performance in the Cu-Bi-Se system.

Acknowledgments

This research was supported by the Institute for Basic Science (IBS) in Korea and by the Human Resources Development Program (no. 20124010203270) of the Korea Institute of Energy Technology Evaluation and Planning (KETEP) grant funded by the Korea government Ministry of Trade, Industry and Energy.

References

- [1] F. J. Disalvo, "Thermoelectric cooling and power generation," *Science*, vol. 285, no. 5428, pp. 703–706, 1999.
- [2] G. J. Snyder and E. S. Toberer, "Complex thermoelectric materials," *Nature Materials*, vol. 7, no. 2, pp. 105–114, 2008.
- [3] H. J. Goldsmid, "Recent studies of bismuth telluride and its alloys," *Journal of Applied Physics*, vol. 32, no. 10, pp. 2198–2202, 1961.
- [4] B. Abeles, "Lattice thermal conductivity of disordered semiconductor alloys at high temperatures," *Physical Review*, vol. 131, no. 5, pp. 1906–1911, 1963.
- [5] W. M. Yim, E. V. Fitzke, and F. D. Rosi, "Thermoelectric properties of $\text{Bi}_2\text{Te}_3\text{--Sb}_2\text{Te}_3\text{--Sb}_2\text{Se}_3$ pseudo-ternary alloys in the temperature range 77 to 300 K," *Journal of Materials Science*, vol. 1, no. 1, pp. 52–65, 1966.
- [6] C. Wood, "Materials for thermoelectric energy conversion," *Reports on Progress in Physics*, vol. 51, no. 4, pp. 459–539, 1988.
- [7] B. Wölfing, C. Kloc, J. Teubner, and E. Bucher, "High performance thermoelectric Tl_3BiTe_6 with an extremely low thermal conductivity," *Physical Review Letters*, vol. 86, no. 19, pp. 4350–4353, 2001.
- [8] K. Kurosaki, A. Kosuga, H. Muta, M. Uno, and S. Yamanaka, "Ag₉TlTe₅: a high-performance thermoelectric bulk material with extremely low thermal conductivity," *Applied Physics Letters*, vol. 87, no. 6, Article ID 061919, 2005.
- [9] B. C. Sales, D. Mandrus, and R. K. Williams, "Filled skutterudite antimonides: a new class of thermoelectric materials," *Science*, vol. 272, no. 5266, pp. 1325–1328, 1996.
- [10] V. Keppens, D. Mandrus, B. C. Sales et al., "Localized vibrational modes in metallic solids," *Nature*, vol. 395, no. 6705, pp. 876–878, 1998.
- [11] J. Yang, W. Zhang, S. Q. Bai, Z. Mei, and L. D. Chen, "Dual-frequency resonant phonon scattering in $\text{Ba}_x\text{R}_y\text{Co}_4\text{Sb}_{12}$ ($R = \text{La, Ce, and Sr}$)," *Applied Physics Letters*, vol. 90, no. 19, Article ID 192111, 2007.
- [12] J. L. Cohn, G. S. Nolas, V. Fessatidis, T. H. Metcalf, and G. A. Slack, "Glasslike heat conduction in high-mobility crystalline

- semiconductors,” *Physical Review Letters*, vol. 82, no. 4, pp. 779–782, 1999.
- [13] D.-Y. Chung, T. Hogan, P. Brazis et al., “CsBi₄Te₆: a high-performance thermoelectric material for low-temperature applications,” *Science*, vol. 287, no. 5455, pp. 1024–1027, 2000.
- [14] O. Delaire, J. Ma, K. Marty et al., “Giant anharmonic phonon scattering in PbTe,” *Nature Materials*, vol. 10, no. 8, pp. 614–619, 2011.
- [15] W. Xie, X. Tang, Y. Yan, Q. Zhang, and T. M. Tritt, “Unique nanostructures and enhanced thermoelectric performance of melt-spun BiSbTe alloys,” *Applied Physics Letters*, vol. 94, no. 10, Article ID 102111, 2009.
- [16] W. K. Liebmann and E. A. Miller, “Preparation phase-boundary energies, and thermoelectric properties of InSb-Sb eutectic alloys with ordered microstructures,” *Journal of Applied Physics*, vol. 34, no. 9, pp. 2653–2659, 1963.
- [17] A. I. Hochbaum, R. Chen, R. D. Delgado et al., “Enhanced thermoelectric performance of rough silicon nanowires,” *Nature*, vol. 451, no. 7175, pp. 163–167, 2008.
- [18] J. Y. Cho, H. Mun, B. Ryu et al., “Cu-Bi-Se-based pavonite homologue: a promising thermoelectric material with low lattice thermal conductivity,” *Journal of Material Chemistry A*, vol. 1, no. 34, pp. 9768–9774, 2013.
- [19] L. D. Zhao, S. Hao, S. H. Lo et al., “High thermoelectric performance via hierarchical compositionally alloyed nanostructures,” *Journal of the American Chemical Society*, vol. 135, no. 19, pp. 7364–7370, 2013.
- [20] G. J. Snyder, M. Christensen, E. Nishibori, T. Caillat, and B. B. Iversen, “Disordered zinc in Zn₄Sb₃ with phonon-glass and electron-crystal thermoelectric properties,” *Nature Materials*, vol. 3, no. 7, pp. 458–463, 2004.
- [21] H. Liu, X. Shi, F. Xu et al., “Copper ion liquid-like thermoelectrics,” *Nature Materials*, vol. 11, no. 5, pp. 422–425, 2012.

Research Article

Solid-State Synthesis and Thermoelectric Properties of $\text{Mg}_{2+x}\text{Si}_{0.7}\text{Sn}_{0.3}\text{Sb}_m$

Sin-Wook You,¹ Il-Ho Kim,¹ Soon-Mok Choi,² and Won-Seon Seo³

¹ Department of Materials Science and Engineering, Korea National University of Transportation, Chungju, Chungbuk 380-702, Republic of Korea

² School of Energy, Materials and Chemical Engineering, Korea University of Technology and Education, Cheonan, Chungnam 330-708, Republic of Korea

³ Energy and Environmental Materials Division, Korea Institute of Ceramic Engineering and Technology, Seoul 153-801, Republic of Korea

Correspondence should be addressed to Il-Ho Kim; ihkim@ut.ac.kr

Received 29 May 2013; Revised 1 August 2013; Accepted 7 August 2013

Academic Editor: Hyung-Ho Park

Copyright © 2013 Sin-Wook You et al. This is an open access article distributed under the Creative Commons Attribution License, which permits unrestricted use, distribution, and reproduction in any medium, provided the original work is properly cited.

$\text{Mg}_{2+x}\text{Si}_{0.7}\text{Sn}_{0.3}\text{Sb}_m$ ($0 \leq x \leq 0.2$, $m = 0$ or 0.01) solid solutions have been successfully prepared by mechanical alloying and hot pressing as a solid-state synthesis route. All specimens were identified as phases with antifluorite structure and showed n-type conduction. The electrical conductivity of Mg-excess solid solutions was enhanced due to increased electron concentrations. The absolute values of the Seebeck coefficient varied substantially with Sb doping and excess Mg, which was attributed to the change in carrier concentration. The onset temperature of bipolar conduction was shifted higher with Sb doping and excess Mg. The lowest thermal conductivity of 1.3 W/mK was obtained for $\text{Mg}_{2.2}\text{Si}_{0.7}\text{Sn}_{0.3}\text{Sb}_{0.01}$. A maximum ZT of 0.64 was achieved at 723 K for $\text{Mg}_{2.2}\text{Si}_{0.7}\text{Sn}_{0.3}\text{Sb}_{0.01}$.

1. Introduction

A thermoelectric generator that converts heat energy directly into electricity offers several benefits, including moderate efficiency, simple device structure, and no moving parts [1, 2]. Thermoelectric materials for high energy conversion efficiency should have a large figure-of-merit value ($ZT = \alpha^2 \sigma T / \kappa$), that is, a large Seebeck coefficient (α), high electrical conductivity (σ), and low thermal conductivity (κ). However, for a given material, these parameters are not independent, because they are closely related to carrier concentration and effective mass. Consequently, thermoelectric materials with a high ZT value should have low lattice thermal conductivity and high carrier mobility with optimum carrier concentration [3, 4].

Magnesium compounds Mg_2X ($\text{X} = \text{Si, Ge, Sn}$) and their solid solutions have attracted increasing attention as promising thermoelectric materials at temperatures ranging

from 500 to 800 K , because they are nontoxic, environmentally friendly, and abundant [5, 6]. In general, the thermal conductivity can be significantly reduced by phonon scattering of point defects as seen solid solutions, which make the low-frequency phonons decrease the thermal conductivity. Among the various solid-solution Mg_2X systems, it is expected that higher ZT can be obtained with $\text{Mg}_2\text{Si}_{1-x}\text{Sn}_x$, because of the greater difference in atomic mass between Si and Sn [7, 8].

The content of Mg and Sb has a significant impact on the electron concentration and thermoelectric properties of n-type $\text{Mg}_2\text{Si}_{1-x}\text{Sn}_x$ solid solutions [9, 10]. The ZT values of $\text{Mg}_2\text{Si}_{1-x}\text{Sn}_x$ solid solutions can be enhanced through excess Mg and/or Sb doping. In order to reduce the changes in composition due to the volatilization and oxidation caused by Mg, $\text{Mg}_{2+x}\text{Si}_{0.7}\text{Sn}_{0.3}\text{Sb}_m$ solid solutions with controlled Mg contents were synthesized by mechanical alloying and hot pressing as a solid-state route.

2. Experimental Procedure

$\text{Mg}_{2+x}\text{Si}_{0.7}\text{Sn}_{0.3}\text{Sb}_m$ ($0 \leq x \leq 0.2$, $m = 0$ or 0.01) solid solutions were synthesized by mechanical alloying (MA) and consolidated by hot pressing (HP). High-purity Mg (99.99%, $<149 \mu\text{m}$) with an excess of 0–10 mol%, Si (99.99%, $<45 \mu\text{m}$), Sn (99.999%, $<75 \mu\text{m}$), and Sb (99.999%, $<75 \mu\text{m}$) were weighed. The powders were mixed and loaded with hardened steel balls (5 mm in diameter) into a hardened steel vial in an argon atmosphere at a weight ratio of 1:20. The vial was then loaded into a planetary ball mill (Fritsch, Pulverisette 5) and mechanically alloyed at 300 rpm for 24 h. The synthesized powders were hot-pressed in a cylindrical graphite die with an internal diameter of 10 mm at temperatures ranging from 873 K to 1073 K under a pressure of 70 MPa for 2 h in a vacuum.

The phases and lattice constants of the synthesized solid solutions were analyzed by an X-ray diffractometer (XRD, Bruker D8 Advance) using $\text{Cu K}\alpha$ radiation (2θ : 10–90°). The Hall coefficient measurements were performed in a constant magnetic field (1 T) and electric current (50 mA) using the van der Pauw method at room temperature. The Seebeck coefficient and electrical conductivity were measured using the temperature differential and 4-probe methods, respectively, with ZEM-3 equipment (Ulvac-Riko) in a helium atmosphere. The thermal conductivity was estimated from measurements of the thermal diffusivity, specific heat, and density, which were obtained using a laser flash TC-9000H system (Ulvac-Riko) in a vacuum. The thermoelectric figure of merit was evaluated from 323 K to 823 K.

3. Results and Discussion

Figure 1 shows the X-ray diffraction patterns for solid-state synthesized $\text{Mg}_{2+x}\text{Si}_{0.7}\text{Sn}_{0.3}\text{Sb}_m$ solid solutions. All specimens were identified as phases with antiferroite structure. The patterns of solid solutions correspond with all the peaks located between pure Mg_2Si and Mg_2Sn , but in the equilibrium phase diagram of the Mg_2Si – Mg_2Sn pseudobinary system, the $\text{Mg}_2\text{Si}_{1-x}\text{Sn}_x$ has an immiscibility gap in the range of $x = 0.4$ – 0.6 [11] or $x = 0.2$ – 0.7 [12], and the Sn-rich phase coexists with the Si-rich phase in this composition range. In this study, the Si-rich phases were observed, but secondary phases were not found.

Table 1 lists the electronic transport properties of $\text{Mg}_{2+x}\text{Si}_{0.7}\text{Sn}_{0.3}\text{Sb}_m$ at room temperature. All specimens showed n-type conduction, and the carrier concentration of $\text{Mg}_2\text{Si}_{0.7}\text{Sn}_{0.3}$ was approximately $7.4 \times 10^{16} \text{ cm}^{-3}$, which was increased to $1.8 \times 10^{19} \text{ cm}^{-3}$ by excess Mg and Sb doping. The Sb successfully acted as a donor, and the excess Mg donated electrons. However, the carrier mobility was reduced by excess Mg and Sb doping, which was attributed to ionized impurity scattering.

Figure 2 shows the temperature dependence of the electrical conductivity for $\text{Mg}_{2+x}\text{Si}_{0.7}\text{Sn}_{0.3}\text{Sb}_m$. The electrical conductivity increased with increasing temperature, indicating nondegenerate semiconducting behavior. For the excess Mg and Sb-doped specimens, the electrical conductivity

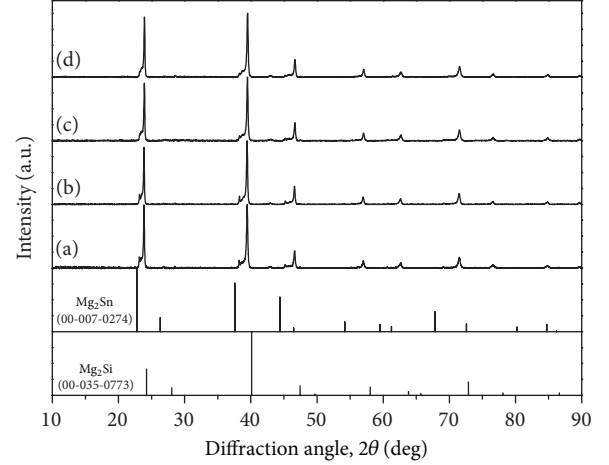


FIGURE 1: X-ray diffraction patterns for $\text{Mg}_{2+x}\text{Si}_{0.7}\text{Sn}_{0.3}\text{Sb}_m$ solid solutions: (a) $\text{Mg}_2\text{Si}_{0.7}\text{Sn}_{0.3}$, (b) $\text{Mg}_2\text{Si}_{0.7}\text{Sn}_{0.3}\text{Sb}_{0.01}$, (c) $\text{Mg}_{2.1}\text{Si}_{0.7}\text{Sn}_{0.3}\text{Sb}_{0.01}$, and (d) $\text{Mg}_{2.2}\text{Si}_{0.7}\text{Sn}_{0.3}\text{Sb}_{0.01}$.

TABLE 1: Electronic transport properties of $\text{Mg}_{2+x}\text{Si}_{0.7}\text{Sn}_{0.3}\text{Sb}_m$ at room temperature.

Specimen	Hall coefficient (cm^3/C)	Mobility (cm^2/Vs)	Carrier concentration (cm^{-3})
$\text{Mg}_2\text{Si}_{0.7}\text{Sn}_{0.3}$	−83.88	30.25	7.4×10^{16}
$\text{Mg}_2\text{Si}_{0.7}\text{Sn}_{0.3}\text{Sb}_{0.01}$	−4.30	9.44	1.4×10^{18}
$\text{Mg}_{2.1}\text{Si}_{0.7}\text{Sn}_{0.3}\text{Sb}_{0.01}$	−0.36	1.67×10^{-1}	1.8×10^{19}
$\text{Mg}_{2.2}\text{Si}_{0.7}\text{Sn}_{0.3}\text{Sb}_{0.01}$	−0.39	1.74×10^{-1}	1.5×10^{19}

increased at specific temperature due to an increase in carrier concentration compared to $\text{Mg}_2\text{Si}_{0.7}\text{Sn}_{0.3}$, as shown in Table 1. As a result, the electrical conductivity of the Mg-excess solid solutions was enhanced.

Figure 3 presents the temperature dependence of the Seebeck coefficient for $\text{Mg}_{2+x}\text{Si}_{0.7}\text{Sn}_{0.3}\text{Sb}_m$. The Seebeck coefficient had a negative sign at all temperature ranges, which was in good agreement with the Hall coefficient. The absolute values of the Seebeck coefficient varied considerably with Sb doping and excess Mg, which was attributed to the changes in carrier concentration. The onset temperature of bipolar conduction was increased with Sb doping and excess Mg. According to the formula $|\alpha| = r - \ln n$, where $|\alpha|$ is the absolute value of the Seebeck coefficient, r is the scattering parameter, c is the constant, and n is the carrier concentration [12], $|\alpha|$ became smaller because n was increased by Sb doping and excess Mg.

Figure 4 shows the temperature dependence of the power factor (PF) for $\text{Mg}_{2+x}\text{Si}_{0.7}\text{Sn}_{0.3}\text{Sb}_m$. The power factor was calculated by $PF = \alpha^2 \sigma$ from the Seebeck coefficient (α) and electrical conductivity (σ). PF increased with increasing temperature and by Sb doping and excess Mg. Compared with $\text{Mg}_2\text{Si}_{0.7}\text{Sn}_{0.3}\text{Sb}_{0.01}$, the PF value of specimens with excess Mg was improved by a factor of 3 to 4. The highest PF was 1.46 mW/mK^2 at 723 K for $\text{Mg}_{2.2}\text{Si}_{0.7}\text{Sn}_{0.3}\text{Sb}_{0.01}$.

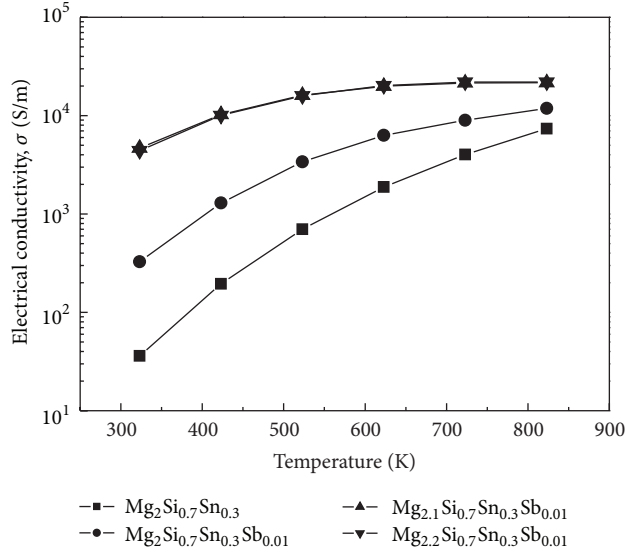


FIGURE 2: Temperature dependence of the electrical conductivity for $\text{Mg}_{2+x}\text{Si}_{0.7}\text{Sn}_{0.3}\text{Sb}_m$.

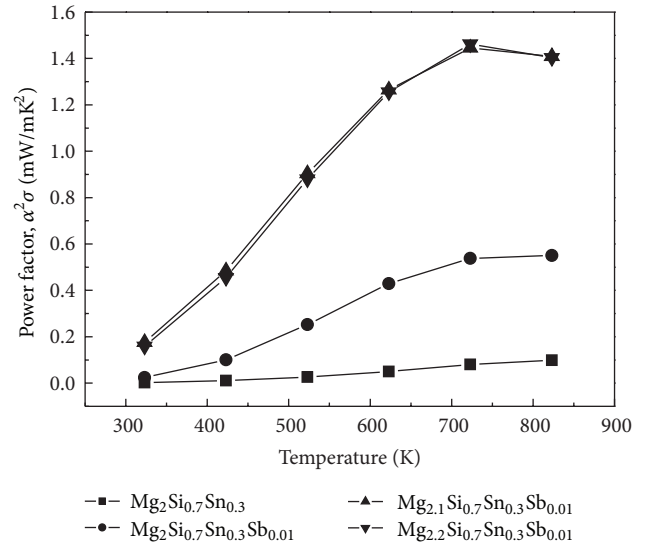


FIGURE 4: Temperature dependence of the power factor for $\text{Mg}_{2+x}\text{Si}_{0.7}\text{Sn}_{0.3}\text{Sb}_m$.

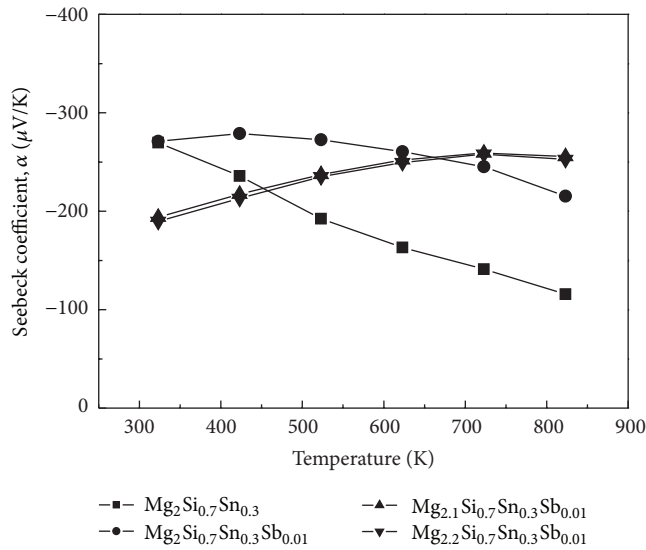


FIGURE 3: Temperature dependence of the Seebeck coefficient for $\text{Mg}_{2+x}\text{Si}_{0.7}\text{Sn}_{0.3}\text{Sb}_m$.

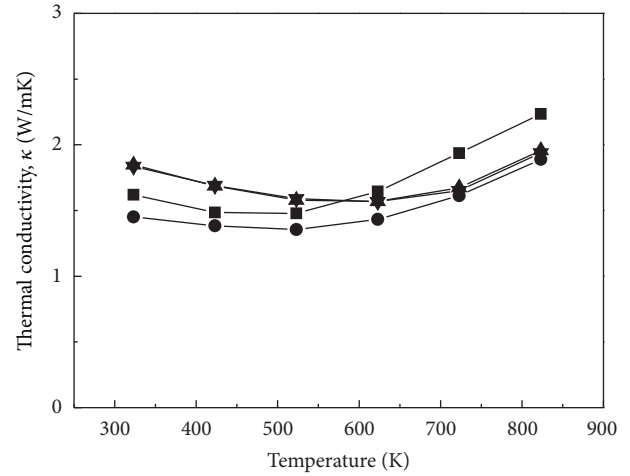


FIGURE 5: Temperature dependence of the thermal conductivity for $\text{Mg}_{2+x}\text{Si}_{0.7}\text{Sn}_{0.3}\text{Sb}_m$.

Figure 5 presents the temperature dependence of the thermal conductivity of $\text{Mg}_{2+x}\text{Si}_{0.7}\text{Sn}_{0.3}\text{Sb}_m$. The thermal conductivity was 1.3–2.2 W/mK in the temperature range of 323 K to 823 K. The thermal conductivity had a minimum value with increasing temperature. The increase in thermal conductivity at high temperatures was attributed to bipolar conduction by intrinsic excitation. Sb doping and excess Mg increased the onset temperature of bipolar conduction. $\text{Mg}_2\text{Si}_{0.7}\text{Sn}_{0.3}\text{Sb}_{0.01}$ had the lowest thermal conductivity of 1.3–1.9 W/mK at all temperatures. The lattice contribution to the thermal conductivity was dominant over the carrier contribution for $\text{Mg}_{2+x}\text{Si}_{0.7}\text{Sn}_{0.3}\text{Sb}_m$ specimens because their

thermal conduction behavior was inconsistent with the Wiedemann-Franz law [13].

Figure 6 shows the temperature dependence of the figure of merit (ZT) for $\text{Mg}_{2+x}\text{Si}_{0.7}\text{Sn}_{0.3}\text{Sb}_m$. The ZT values of the undoped specimen were very low, with values less than 0.05 at all temperatures examined. However, the ZT was remarkably increased by Sb doping and excess Mg, mainly due to the increase in power factor. A maximum ZT of 0.64 was achieved at 723 K for $\text{Mg}_{2.2}\text{Si}_{0.7}\text{Sn}_{0.3}\text{Sb}_{0.01}$. The ZT values of $x = 0.1$ and $x = 0.2$ were nearly the same, which makes $x = 0.1$ a sufficient amount of excess Mg to improve the thermoelectric properties.

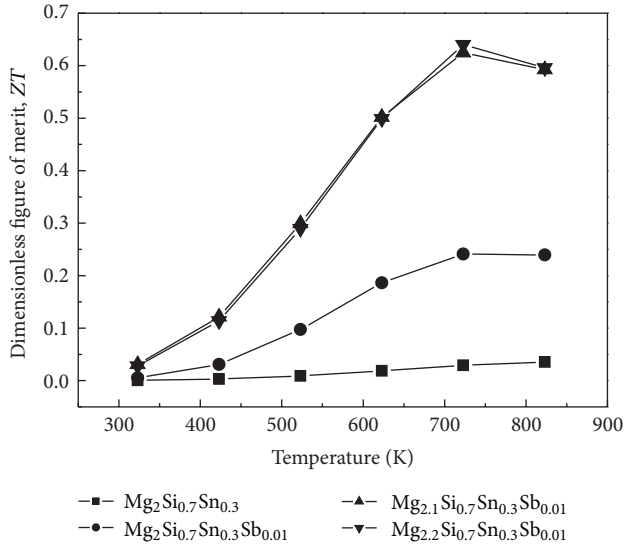


FIGURE 6: Dimensionless thermoelectric figure of merit for $\text{Mg}_{2+x}\text{Si}_{0.7}\text{Sn}_{0.3}\text{Sb}_m$.

4. Conclusions

$\text{Mg}_{2+x}\text{Si}_{0.7}\text{Sn}_{0.3}\text{Sb}_m$ ($0 \leq x \leq 0.2$, $m = 0$ or 0.01) solid solutions were successfully prepared by mechanical alloying and hot pressing. All specimens showed n-type conduction, and the carrier concentration effectively increased from $7.4 \times 10^{16} \text{ cm}^{-3}$ to $1.8 \times 10^{19} \text{ cm}^{-3}$ by Sb doping and excess Mg. As a result, the electrical conductivity increased remarkably. The temperature dependencies of the Seebeck coefficient and the thermal conductivity were varied by Sb doping and excess Mg, which increased the onset temperature of bipolar conduction. A maximum ZT of 0.64 was achieved at 723 K for $\text{Mg}_{2.2}\text{Si}_{0.7}\text{Sn}_{0.3}\text{Sb}_{0.01}$ with excess Mg.

Acknowledgments

This study was supported by the Fundamental R&D Program for Core Technology of Materials and by the Regional Innovation Center (RIC) Program, funded by the Ministry of Trade, Industry and Energy (MOTIE), Republic of Korea.

References

- [1] M. Akasaka, T. Iida, T. Nemoto et al., "Non-wetting crystal growth of Mg_2Si by vertical Bridgman method and thermoelectric characteristics," *Journal of Crystal Growth*, vol. 304, no. 1, pp. 196–201, 2007.
- [2] Z. Du, T. Zhu, and X. Zhao, "Enhanced thermoelectric properties of $\text{Mg}_2\text{Si}_{0.58}\text{Sn}_{0.42}$ compounds by Bi doping," *Materials Letters*, vol. 66, no. 1, pp. 76–78, 2012.
- [3] Q. Zhang, J. He, T. J. Zhu, S. N. Zhang, X. B. Zhao, and T. M. Tritt, "High figures of merit and natural nanostructures in $\text{Mg}_2\text{Si}_{0.4}\text{Sn}_{0.6}$ based thermoelectric materials," *Applied Physics Letters*, vol. 93, no. 10, Article ID 102109, 3 pages, 2008.
- [4] W. Liu, Q. Zhang, X. Tang, H. Li, and J. Sharp, "Thermoelectric properties of Sb-doped $\text{Mg}_2\text{Si}_{0.3}\text{Sn}_{0.7}$," *Journal of Electronic Materials*, vol. 40, no. 5, pp. 1062–1066, 2011.

- [5] J.-I. Tani and H. Kido, "Thermoelectric properties of Bi-doped Mg_2Si semiconductors," *Physica B*, vol. 364, no. 1–4, pp. 218–224, 2005.
- [6] J.-I. Tani and H. Kido, "Thermoelectric properties of P-doped Mg_2Si semiconductors," *Japanese Journal of Applied Physics A*, vol. 46, no. 6, pp. 3309–3314, 2007.
- [7] V. K. Zaitsev, M. I. Fedorov, A. T. Burkov et al., "Some features of the conduction band structure, transport and optical properties of n-type Mg_2Si - Mg_2Sn alloys," in *Proceedings of the 21st International Conference on Thermoelectrics*, pp. 151–154, 2002.
- [8] M. I. Fedorov, D. A. Pshenary-Severin, V. K. Zaitsev, S. Sano, and M. V. Vedernikov, "Features of conduction mechanism in n-type $\text{Mg}_2\text{Si}_{1-x}\text{Sn}_x$ solid solutions," in *Proceedings of the 22nd International Conference on Thermoelectrics*, pp. 142–145, 2003.
- [9] W. Liu, X. Tang, H. Li, J. Sharp, X. Zhou, and C. Uher, "Optimized thermoelectric properties of Sb-doped $\text{Mg}_{2(1+z)}\text{Si}_{0.5-y}\text{Sn}_{0.5}\text{Sb}_y$ through adjustment of the Mg content," *Chemistry of Materials*, vol. 23, no. 23, pp. 5256–5263, 2011.
- [10] W. Liu, X. F. Tang, H. Li, K. Yin, J. Sharp, and X. Y. Zhou, "Enhanced thermoelectric properties of n-type $\text{Mg}_{2.16}(\text{Si}_{0.4}\text{Sn}_{0.6})_{1-y}\text{Sb}_y$ due to nano-sized Sn-rich precipitates and an optimized electron concentration," *Journal of Materials Chemistry*, vol. 22, no. 27, pp. 13653–13661, 2012.
- [11] S. Wang and N. Mingo, "Improved thermoelectric properties of $\text{Mg}_2\text{Si}_x\text{Ge}_y\text{Sn}_{1-x-y}$ nanoparticle-in-alloy materials," *Applied Physics Letters*, vol. 94, no. 20, Article ID 203109, 3 pages, 2009.
- [12] Q. Zhang, X. B. Zhao, H. Yin, and T. J. Zhu, "Thermoelectric performance of $\text{Mg}_{2-x}\text{Ca}_x\text{Si}$ compounds," *Journal of Alloys and Compounds*, vol. 464, no. 1–2, pp. 9–12, 2008.
- [13] C. Kittel, *Introduction to Solid State Physics*, John Wiley & Sons, New York, NY, USA, 6th edition, 1986.